TECHNISCHE UNIVERSITÄT WIEN

DISSERTATION

Assessment of Urban Microclimate Based on Remote Sensing and Building-related Attributes

ausgeführt zum Zwecke der Erlangung des akademischen Grades eines Doktors der Technischen Wissenschaften Architektur unter der Leitung von

Univ. Prof. Dipl. -Ing. Dr.techn. Ardeshir Mahdavi

E 259/3 Forschungsbereich Bauphysik und Bauökologie

Institut für Architekturwissenschaften

Begutachtung durch

Associate Prof. Dipl.-Ing. Dipl.-Ing.(FH) Dr.techn. Matthias Wilhelm Schuß

Prof. Dr. Mustafa Emre İlal

eingereicht an der Technischen Universität Wien
Fakultät für Architektur und Raumplanung

von

Pelin Fırat Örs

[redacted]

[redacted]

Wien, April 2022

Summary

The research conveyed by the present dissertation explores microclimatic conditions the dwellers experience in urbanized locations. It focuses on the interrelationship between microclimatic conditions and building-related attributes. To this end, such interrelationships are examined at seven specific study areas in the city of Vienna (Austria) and its surroundings. Thereby, the research employs satellite-based land surface temperature (LST) data from Moderate Resolution Imaging Spectroradiometer (MODIS) sensors and examines this data with respect to the obtained near-surface air temperature (T_{air}) data from seven meteorological stations operated by Zentralanstalt für Meteorologie und Geodynamik (ZAMG). Thermal data from a temporal range of about 15 years (from 05.03.2000/04.07.2002 to 01.09.2015) are considered. The nature of the data is specifically studied at two day-time and two night-time intervals. The research explores alternative scenarios for deriving near-surface temperatures over the study locations. The present dissertation further proposes and evaluates the performance of day-time and night-time models for deriving near-surface temperatures over all studied locations. The performance of the selected models at the individual weather station locations are further documented.

Kurzfassung

Die vorliegende Dissertation beschäftigt sich mit den mikroklimatische Bedingungen und deren Wirkung auf die Nutzer im urbanen Umfeld. Konkret wird die Wechselbeziehung des urbanen Mikroklimas sowie deren Veränderung durch gebäudebezogene Einflüsse betrachtet. Für die konkreten Analysen wurden sieben exemplarische Standorten in Österreich, mit Schwerpunkt auf die Stadt Wien und ihre Umgebung ausgewählt. Satellitengestützte Landoberflächen-temperatur (LST) auf Grundlage von Daten von Moderate Resolution Imaging Spectroradiometer (MODIS)-Sensoren und gemessenen oberflächennahen Lufttemperaturdaten (Tair) der zugehörigen meteorologischen Stationen der Zentralanstalt für Meteorologie und Geodynamik (ZAMG) wurden hinsichtlich ihrer Korrelation untersucht. Insgesamt wurden Daten aus etwa 15 Jahren (von 05.03.2000/04.07.2002 bis 01.09.2015) an jeweils zwei Tages- und Nachtintervallen analysiert und für die Entwicklung neuer Szenarien zur Berechnung er bodennahen Lufttemperaturen verwendet. In dieser Arbeit wurde unterschiedliche Tages- und Nachtmodelle zur Ableitung der bodennahen Lufttemperatur vorgeschlagen und deren Qualität für die sieben Studienstandorte dokumentiert.

Acknowledgements

First, and foremost, I would like to thank my supervisor Univ. Prof. Dipl. -Ing. Dr.techn. Ardeshir Mahdavi for his support, guidance, patience, and encouragement during my studies at TU Wien. It was always a pleasure learning from him, beyond the limits of the work presented here. I will always admire his passion towards teaching and research.

I would like to also thank Republic of Türkiye for funding and supporting my doctoral studies at TU Wien. The research presented in this dissertation, and my doctoral education at TU Wien has been funded within the scope of YLSY Overseas Postgraduate Scholarship by Republic of Türkiye Ministry of National Education.

I would like to thank Republic of Türkiye Minister of National Education Prof. Dr. Mahmut Özer, Ambassador of the Republic of Türkiye to Vienna Ozan Ceyhun and his wife Azize Ceyhun, Education Counsellor of the Embassy of the Republic of Türkiye in Vienna Assoc. Prof. Dr. Yusuf Yıldız, Mr. Erdem Uysal, and Republic of Türkiye Ministry of National Education General Directorate of Higher and Foreign Education team for their sincere support and encouragement during my education in Vienna, even in the most uncertain times of the COVID-19 pandemic.

I would like to thank the current and past members of the BPI Team at TU Wien, especially Dipl.-Ing.in Dr.in Milena Vuckovic. I learned so much from following the guideposts they left through their remarkable contributions in documenting and investigating the urban climate of Vienna.

I would like to thank Canan Yemez, Mina Aslan, and Gülay Kırmızı for their support, and for truly being there when I needed.

I would like to thank my husband Taylan Örs, for giving me the strength and endurance, endless humour, love, patience, and optimism.

Last, but not the least, I would like to thank my mother Sevgül Fırat and my father Aydın Fırat who have always been there for me, no matter the circumstances. I will be always thankful and indebted for their love, support, encouragement, and belief in me.

Table of Contents

List of Abbreviations

BSA	Black Sky Albedo
BSF	Building Surface Fraction
CET	Central European Time
DSM	Digital Surface Model
DTM	Digital Terrain Model
EBH	Equivalent Building Height
GEE	Google Earth Engine
ISF	Impervious Surface Fraction
LCZ	Local Climate Zone
LST	Land Surface Temperature
MBH	Area-weighted Mean Building Height
OSCAR	Observing Systems Capability Analysis and Review Tool
PSF	Pervious Surface Fraction
RSL	Roughness Sublayer
SUHI	Surface Heat Islands
SVF	Sky View Factor
SZA	Solar Zenith Angle
T_{air}	Near-surface Air Temperature
U2O	Urban Units of Observation
UBL	Urban Boundary Layer
UCL	Urban Canopy Layer
UHI	Urban Heat Island

UHII	Urban Heat Island Intensity
UHI_{BL}	Boundary Layer Urban Heat Island
UHI_{CL}	Canopy Layer Urban Heat Island
VIF	Variance Inflation Factor
WMO	World Meteorological Organization
WS	Terrestrial Meteorological Weather Station
ZAMG	Zentralanstalt für Meteorologie und Geodynamik

1. INTRODUCTION

1.1. Motivation

The Earth has been experiencing a significant growth in the human population, from around 2.6 billion (1950) to seven billion (2011) in just over 60 years. A further 1.5 billion increase is expected from this figure until 2030, at which, the projections indicate an 8.5 billion people will be residing on Earth (UN 2022).

An upward trend is also being observed in the demographic development of the urbanized regions, which accommodated 30% of the whole human population in 1950 and 55% in 2018. 2050 projections indicate even larger figures with 68% (UN 2018). All these reported trends suggest significant transformations in the physical environments.

While the developmental processes and consequent impacts of these transformations are many-fold, they commonly lead to the expansion and/or densification of the built environment in the (existing) urban areas (see, for instance, Chakraborty et al. 2021; Espindola et al. 2017). These "urbanization" processes take place via transformations in the material-based and form-related characteristics of these environments and are also strongly associated with increased anthropogenic activities and emissions (Grimmond 2007; Mills 2014; Voogt 2017).

Due to the differences in the heat and water retention behaviours of natural surfaces and the artificial-urban ones, these afore-mentioned transformations constitute an "urban fabric" which is "drier", and which possesses enhanced heat storage capabilities (Barlow 2014; EPA 2008; Grimmond 2007; Oke 1982; Rizwan et al. 2008; Stathopoulou et al. 2009; Voogt 2002; 2017).

Moreover, these changes also lead to a denser and "rougher" 3D environment, and thus influence the air-flow characteristics (Grimmond 2007; Rizwan et al. 2008; Voogt 2017), including the dispersion of pollutants in the urbanized regions (see, for instance, Ng 2009).

Together with the afore-mentioned increase in anthropogenic emissions, these material and form-related transformations of the urbanization have a certain level of control on the thermal environment (Oke 1976; Taha 1997) and consequently, on the air quality, dweller well-being and habits of energy consumption in cities (Grimmond 2007; Taha 1997; Voogt 2002).

Moreover, each city carries particular characteristics in terms of its urban climate and thermal environment, both of which are closely associated with the built environment properties, anthropogenic activities, topographical and geographical features, specific for that city (Oke 1982; 1984). These "unique" features also lead to "microclimatic variations" in the urban thermal domain, as documented in detail by previous research efforts (see, for instance, Lim et al. 2014; Mahdavi et al. 2013; Mahdavi 2018; Maleki et al. 2012; Vuckovic et al. 2016; 2017).

The motivation behind the present dissertation stems from acknowledging that observing these "complex" variations in the urban thermal environment is potentially not practical via conventional terrestrial methods such as the use of meteorological networks (see, for instance, Crawley and Barnaby 2019), as supported by the previous work of Lim et al. (2014) for Vienna. Moreover, terrestrial meteorological information is still limited for some parts of the world. Contrarily, satellite-based platforms offer global thermal data with significantly superior spatial resolution (Weng 2009) and a large portion of this data can be publicly and freely accessible (see, for instance, ESA_Data 2022; Gorelick et al. 2017; NASA_Data 2022).

Motivated by these aspects, the present dissertation explores the thermal information acquired via satellite-based platforms with the aim of obtaining "location-specific" insights on the urban microclimate variations (Firat Ors and Mahdavi 2021; Firat Ors et al. 2019).

1.2. Objective

Based on the afore-mentioned considerations regarding the urban microclimate variations and the potentials of satellite-based platforms for their observation (see, for further details Firat Ors and Mahdavi 2021; Firat Ors et al. 2019), the present dissertation aims to define a systematic approach that offers location-specific insights on urban thermal environments.

For that purpose, it explores the inter-relationship between the microclimatic conditions, more specifically near-surface and land surface temperatures, and the building-related attributes (Firat Ors and Mahdavi 2021; see also Irger 2014).

The aim is to propose a methodology that can facilitate estimations of near-surface temperatures based on GIS and remote sensing data accessible to the public-use (Firat Ors and Mahdavi 2021). The goal is to allow for the potential applicability of the purposed approach in areas where adequate terrestrial meteorological information is not available.

1.3. Structure

This dissertation consists of seven chapters:

- The first chapter provides an overall introduction to the investigated field and the defined research problem.

  This is presented by describing the motivation and the objectives that lead to the problem definition and consequently, to the proposed workflow.

- The second chapter presents a detailed background on the investigated field.

  This includes information regarding the physical aspects and commonly applied methods on the urban climate, with a focus on the thermal remote sensing method.

- The third chapter describes the pursued approach to achieve the research goals defined in the first chapter.

  This is realized through several steps. Initially, the case area and the procedure followed to investigate the building-related attributes are presented. Later, data-selection and filtering processes regarding the remotely-sensed datasets are described. In the last part, the proposed statistical approach to derive near-surface information on the urban thermal environment is explained in detail.

- The fourth chapter presents and discusses the results obtained from the afore-mentioned efforts described in the previous steps.

- The fifth chapter concludes the framework of this dissertation by discussing its findings, limitations and by proposing research topics that can be pursued by future works.

- Further details regarding the references are presented in Chapter 6, and the Appendix is given in Chapter 7.

2. BACKGROUND

According to Oke (1984), there is a general tendency to describe the "urban climates" (p. 19) as "natural climates" (p. 19) that were undergone through the human impacts. Therefore, identifying the role of "urbanization" (p. 19) on the urban climate can be regarded as the motivation behind its inquiries (Oke 1984).

As described by Oke (1984), this aim, to a certain extent, brings up the need to understand the alterations urbanization causes in the environment, and find ways to quantify and address them in urban climate investigations (Oke 1984; see also Mahdavi et al. 2013; Stewart and Oke 2012).

Motivated by these aspects, the first two sections of the present chapter convey the main principles and tendencies of the climatic states that the dwellers experience in urban environments. Here, the focus is given to the urban thermal domain, concerning the goals presented earlier in the first chapter.

2.1. Characteristics of urban climate

As outlined by Oke (1984), looking at the changes in the geometry and material properties of the urban environments introduced with the urbanization processes can be the starting point to these explorations (Oke 1984; see also Mahdavi et al. 2013; Stewart and Oke 2012).

This is supported by many studies which investigated and confirmed the influence of such alterations on the observed climatic conditions in urban environments (see, for instance, Coseo and Larsen 2014; Kantzioura et al. 2015).

In parallel with the findings of these works, Oke (1984) emphasizes the importance of "the urban-atmosphere interface" (p. 20) in urban climate investigations and points out that "the urban 'surface'" (p. 20) is a significant modifier of the climatic conditions observed in the urban settings. According to Oke (1984), this stems from the interaction of the "surface" (p. 20) with highly dynamic processes such as "energy, mass and momentum exchange and transformation" (p. 20) (Oke 1984).

In-line with this point, and as further mentioned by Oke (1984), the material and form-related aspects of the urban environments are not the only features that influence the climatic behaviours of these settings (Mahdavi et al. 2013; Oke 1984; Stewart and Oke 2012; Taha 1997). Emissions from the activities of urban dwellers, i.e., "anthropogenic emissions", also bring about notable changes to the atmospheric composition and contribute to the observed climatic conditions (Mahdavi et al. 2013; Oke 1984; Stewart and Oke 2012; see also Kousis et al. 2021; Vahmani et al. 2022 amongst others).

In this context, Oke (1984) explores investigating the urban climate through the role of the following aspects: "turbulent boundary layers" (p. 20) and "urban morphological units" (p. 20), as proposed by Oke (1976; 1983) (Oke 1984). The latter of these aspects is the geometrical urban features of various scales; whereas the former (mainly) refers to the atmospheric characteristics of the urban settings (Oke 1984; Oke et al. 2017).

These aspects, i.e., atmospheric and surface considerations, have been utilized by Oke (1984) and Oke et al. (2017) as a guiding basis in their efforts to explain the urban climate principles. Following these two works, amongst others, this section explores these two mediums of the urban domain which are also primarily related with the objectives of the present dissertation.

In this context, the motivation to describe the physical processes associated with the urban climate through these two features stems from the points discussed earlier, that these domains are the ones foremost affected by the "urbanization" activities. In other words, they are what is transformed in the environment by the introduction of human habitation. In turn, they influence the environmental quality humans experience and, to a certain degree, the energy they consume (see, Harlan et al. 2006; Santamouris et al. 2015; Sun and Augenbroe 2014; Tsitoura et al. 2014; Vuckovic et al. 2017 amongst others).

To summarize; changes of the "surface cover", transformations of the 3D environment by building urban structures, altering the topography, via activities such as "deforestation" or "plantation" lead to a significantly different physical environment in cities with respect to the one in "rural" regions. These "surface" alterations trigger "atmospheric" changes in the urban environments (see, Dimitrova et al. 2014; Kantzioura et al. 2015; Oke 1984; Oke et al. 2017 amongst others).

Furthermore, the activities that stem from the human habitation in urban areas transform the "structure" and thermal properties of the atmosphere via "anthropogenic emissions" (see, Kousis et al. 2021; Oke et al. 2017; Taha 1997; Vahmani et al. 2022 amongst others).

All of these afore-mentioned factors lead to the environmental and climatic conditions that we experience in the cities (see, Mahdavi et al. 2013; Oke 1984; Oke et al. 2017; Stewart and Oke 2012; Voogt 2017 amongst others).

2.1.1. Atmospheric features

Atmospheric profiles over and in the vicinity of urbanized regions present certain differences with respect to the ones over natural settings (Voogt 2017). These "modifications" occur up to a distinctive vertical extent - commonly 250 m to 2500 m (Oke et al. 2017) - from ground and the layer of atmosphere carrying these effects is identified as the "urban boundary layer (UBL)" (see, for instance, Barlow 2014; Oke 1976; 1982; Oke et al. 2017; Voogt 2017).

Vertical profile of the UBL shows different characteristics which are closely associated with the observed height from the "roughness elements" underneath. For instance, the bottom part of the layer is strongly influenced by the local urban features as they considerably modify the airflow characteristics (Barlow 2014). This part is called the "roughness sublayer (RSL)" and occupies about to two to five times of the average height of the buildings from the ground (Barlow 2014).

Besides the air-flow characteristics, the local features influence other mechanisms in RSL as well, such as the thermal behaviours or the solar access (Voogt 2017).

In RSL, the section just above the ground surface is identified as the "urban canopy layer (UCL)" (see, for further details, Barlow 2014; Mills 2014; Oke 1976; Oke et al. 2017). "Mean" building (in some cases, tree) heights generally set the UCL height (Oke et al. 2017; Voogt 2017); whereas the layer may not be formed in large areas that are devoid of these 3D urban features (Oke 1976). In the present dissertation, the employed air temperature observations are mainly representative of this layer. Further details regarding these observations are presented in the next chapter.

2.1.2. Surface features

As mentioned earlier, the urbanized settings are formed and developed via the modifications in form-related and material-based properties of the natural environments, as buildings and urban surfaces replace the natural topography and materials (see, for instance, Oke 1984; Oke et al. 2017).

In this context, Oke (1984) argues that the geometrical structure of the urban areas exerts impacts on the observed climate at various spatial levels ("scales"). These impacts can influence formation of small distance events (such as "building wakes" (p. 20)) to much larger ones (such as the urban "heat island" effect (p. 21)) in urban environments (Oke 1984; see also Oke et al. 2017; Voogt 2017).

Based on these insights, Oke (1984) groups the geometrical features of the urban settings into "urban morphological units" (p. 20) of various sizes. According to the author, the idea behind this is to utilize these segments together with relevant atmospheric information to obtain practical insights about climatic behaviours at various spatial levels (Oke 1984; see also Oke et al. 2017; Voogt 2017).

These "morphological units" (p.19) differ from single surface features such as "walls" to the increasing "scales" of urban "canyon", "neighbourhood" and so on (Oke et al. 2017; see also Oke 1984; Voogt 2017). Further details of these units can be found in these afore-mentioned sources with minor modifications (see, for instance, Table 2.1. at Oke et al. (2017), p. 19).

From the stand-point of the present dissertation, the idea behind this segmentation (and the associated climatic interactions) is of significance in the context of determining the spatial extents of the selected study areas. This point is discussed further in the next chapter.

2.2. Urban heat islands and microclimates

Based on the surface and atmospheric considerations presented in the previous section, the airflow patterns, pollutant concentrations, thermal behaviours, humidity conditions, characteristics of cloud formation and precipitation, amongst others, present altered characteristics in urban environments (Voogt 2017, amongst others).

By acknowledging the cumulative influence of these processes to one another, the focus of the present dissertation mainly lies within the thermal characteristics of the urbanized settings.

2.2.1. Urban heat island effect

The changes in the atmospheric behaviours and surface features due to urbanization and other anthropogenic activities lead to a warmer urban thermal domain with respect to its surroundings. This "phenomenon" has been identified as the "urban heat island (UHI) effect" (see, for instance, Crawley 2008; EPA 2008; Oke 1995; Oke et al. 2017; Rizwan et al. 2008; Voogt 2002; 2017).

UHIs are observed as greater "sub-surface", "surface" and atmospheric temperatures in urban settings when compared with the ones of the city surroundings (Oke 1995; Oke et al. 2017; Voogt 2002).

The classification of UHIs is also performed accordingly, as "sub-surface heat islands" (Oke 1995; Oke et al. 2017; Yow 2007), "surface heat islands (SUHI)" (EPA 2008; Oke 1995; Oke et al. 2017; Yow 2007) and "atmospheric heat islands (or heat islands in the air)" (EPA 2008; Oke 1995; Yow 2007).

In the present dissertation, the term UHI corresponds to the "atmospheric heat islands", following most studies (see, for instance, Stewart and Oke 2012; Voogt 2002).

In this context, the term "urban heat island intensity (UHII)" identifies the UHI magnitude (Voogt 2002). It is calculated by subtracting rural air temperature observations from spatially corresponding air temperature observations of the urban settings which are conducted within the same time interval (see, for instance, Magee et al. 1999; Yow 2007). UHII is a commonly employed metric to track down the extents of the urban warming.

2.2.1.1 Exploring surface and atmospheric heat islands

Affected by the afore-mentioned dynamics of the urban environments, the developmental behaviours of UHIs and SUHIs present different characteristics (EPA 2008; Grimmond 2007; Oke et al. 2017; Voogt 2002).

In this context, the "atmospheric urban heat islands" are investigated under two sub-groups based on the section of the atmosphere they are formed: "canopy layer urban heat islands" and "boundary layer urban heat islands" (EPA 2008). This differentiation was first suggested by Oke (1976).

The boundary layer UHIs (UHI_{BL}s) form within the upper part of the UBL, at the top of the UCL (EPA 2008; Oke 1976; 1995; Oke et al. 2017). Fixed ("tower", "sodar" (p. 82)) or mobile ("aircraft", "tetroon" (p. 82)) measurements are utilized for investigating them (Oke 1995).

The canopy layer UHIs (UHI_{CL}s) are formed below the level that the UHI_{BL}s are formed, within the UCL (EPA 2008; Oke 1995; Oke et al. 2017). The research efforts studying UHIs more often address the UHI_{CL}s in their inquiries (EPA 2008; Voogt 2002; Voogt 2017; Yow 2007). According to Yow (2007), this is largely attributed to the way UHI_{CL}s are detected, which is more convenient than observing UHI_{BL}s with less complicated equipment and a more effortless reachability of the UCL (Yow 2007).

The observations of UHI_{CL}s are generally conducted from the "standard screen height", which corresponds to a height of 1-2 meters from the ground level (Stewart and Oke 2012) and by means of weather stations that can be stationary or mobile (EPA 2008; Voogt 2002).

On the other hand, the "surface heat islands (SUHIs)" display a more dynamic behaviour, both temporally and spatially, with respect to UHIs (EPA 2008) and "remote sensing" method is commonly utilized in their inquiries (EPA 2008; Yow 2007; see also Mathew et al. 2018; Schwarz et al. 2011; Stathopoulou et al. 2009; Wang et al. 2019 amongst others).

As Voogt (2002) points out, with respect to the air temperatures, the surface temperatures have a more dynamic character as they are more responsive to the climatic processes exerted on them. These characteristics also depart SUHIs from UHIs (Voogt 2002).

In this context, diurnal dynamics of urban and rural thermal environments are presented in the next sub-section of this dissertation. Here, the aim is to provide a background on how the urban thermal environment departs from the rural within a diurnal cycle. The factors and processes leading to this departure is also presented in the following parts of this chapter.

2.2.1.2. Diurnal behaviours of urban and rural environments

Oke (1982) provides an overview of the diurnal development of UHI_{CL}s by individually addressing "rural" and "urban" thermal environments. Note that, these insights belong to "idealized" (p. 2) conditions at the "screen-level" (p. 2) height, pertaining to a day in hot season, with "calm or very light" (p. 2) wind and clear sky conditions for "a large temperate-climate city" (p. 2) (Oke 1982).

According to Oke (1982), for the afore-mentioned conditions, the rural thermal environment undergoes a cooling trend around the time of sunset, triggered by the radiative heat loss from rural surfaces. This trend slows down during the night. It is later replaced by a warming trend which starts a bit later than the sunrise and continues until the time of peak temperature in the afternoon (Oke 1982).

As Oke (1982) points out, for the urban thermal environment, the thermal processes tend to develop at a slower pace when compared with the ones of rural. This holds true for the whole course of the day, apart from later during the night when urban environments present a bit higher cooling tendency (Oke 1982).

As illustrated by Oke (1982), the main driver for the canopy layer UHIs is the different diurnal "cooling" dynamics within the rural and urban domains (Oke 1982; Voogt 2002).

As Oke (1982) points out, the departure between the cooling trends of the two domains are more pronounced (in the favour of rural areas), around sunset and afterwards for a couple of hours (Oke 1982). According to Voogt (2002), the "nocturnal" tendencies of the UHIs stems from these dynamics (Voogt 2002; see also van Hove et al. 2015; Paulina et al. 2015; Vuckovic et al. 2016 amongst others).

2.2.1.3. Further dynamics

Besides the diurnal considerations stated in the previous sub-section, there are various factors that influence the spatial behaviours of a city's thermal environment with respect to the rural; or influence that relationship on various temporal intervals. These include spatial (i.e., "geometrical" and "material-based" features), anthropogenic, topographic, geographic factors that are related with the physical and/ or demographic attributes of the specific cities they exert impacts on; as well as the ones based on weather and seasonal conditions (see, for instance, EPA 2008; Grimmond 2007; Oke 1982; 1995; Oke et al. 2017; Rizwan et al. 2008; Taha 1997; Voogt 2002).

When we look at the weather conditions that result in greater UHIIs, they are primarily the ones with no cloud cover and no significant wind speed (EPA 2008; Grimmond 2007; Voogt 2002; 2017). This is further supported by the findings of a recent research effort, where Ngarambe et al. (2021) reported cloud cover and wind speed had a negative influence on the observed "boundary layer" UHIIs for Seoul (Ngarambe et al. 2021).

On the other hand, the seasonal changes are associated with the amount, direction (Oke 1982) and duration of the solar radiation that reaches the urban surface. They also have a potential control on the use of HVAC systems, thus have an influence on the anthropogenic emissions (Rizwan et al. 2008; Taha 1997). This is supported by the findings of Chapman et al. (2016) for their investigations on anthropogenic emissions in Australia. The seasonal changes associated with UHIIs are also emphasized by findings of van Hove et al. (2015), where they reported the greatest UHIIs for "summer" and "late spring" for Rotterdam agglomeration (van Hove et al. 2015). Likewise, for Vienna, Vuckovic et al. (2016) reported the highest UHIIs for May and August observations with respect to the ones in February and November (Vuckovic et al. 2016).

In addition to the factors mentioned above, features such as latitude, proximity to the blue spaces, positioning of topographical elements such as mountains or valleys also have an influence on the reported UHIIs (see, for instance, EPA 2008; Oke 1982).

For instance, Kourtidis et al. (2015) clearly depict the temporal development of urban air temperatures in Greater Athens Area by focusing on locations at / near topographically significant places such as the sea-side and mountainous regions, and also industrial zones and the urban core; and report considerable differences in thermal behaviours observed at these places (Kourtidis et al. 2015).

In this context, by acknowledging the contribution of all these afore-mentioned parameters on the urban thermal environment and the UHIs, the present dissertation is mainly concerned with the influence of building-related attributes on the thermal domain of the urbanized settings. In this regard, the potential impacts of the built environment and its spatial organization on the thermal environment is discussed with further detail in the following parts of this chapter.

In the light of these points, Figure 1 below represents the distribution of a ("fully-developed" nocturnal) UHI_{CL} (EPA 2008), whose developmental patterns, i.e., "islands", show a notable interaction with the urban spatial features (EPA 2008; Oke 1982; Voogt 2002).

At finer scales than illustrated by Figure 1, the urban thermal environment shows even a more dynamic behaviour (see Lim et al. (2014) amongst others) and presents significant "microclimatic variation". These microclimatic variations as well as further characteristics of UHIs and SUHIs are associated with the "surface energy balance" (Oke 1982; Oke et al. 2017 amongst others), which is discussed in the next sub-section of the present dissertation.

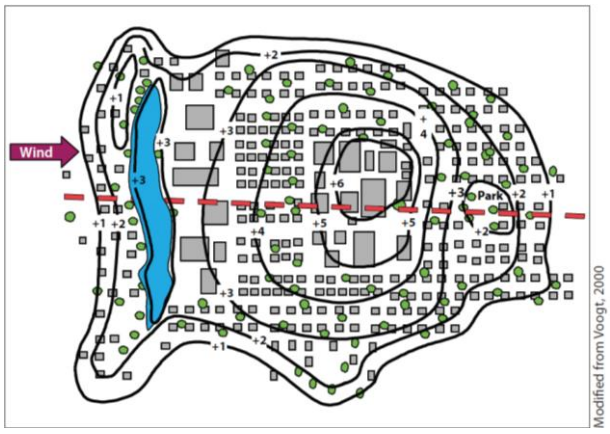

Figure 1. Representation of nocturnal UHI (source: EPA 2008, original source: Voogt 2000 (as cited in EPA 2008))

2.2.2. Microclimate dynamics: Energy balance

According to Voogt (2017), and as discussed earlier, the transfers of "mass" (p. 3) and "energy" (p. 3) due to the interaction of urban surfaces with the surrounding air is what drives the climate observed in an urbanized setting (Voogt 2017). However, this interaction is not mainly straightforward.

As Oke (1982) points out, the UCL is a complex environment where each "surface facet" (p. 7) is characterized by two sets of features which determine their contribution to the urban climate dynamics. These are the surface's own material-based features plus other characteristics stemming from its interaction with the immediate urban domain (Oke 1982). According to Oke (1982), numerous "energy balances" (p. 8) and consequently "microclimates" (p. 8) form in the urban environments thanks to these features and dynamics (Oke 1982).

As Ali-Toudert (2021) remarks, in order to gain insights regarding these dynamics, the "urban energy balance" (p. 3) is fundamental (Ali-Toudert 2021).

In this context, the "surface energy balance" is illustrated as (Arnfield 2003; Mirzaei and Haghighat 2010; Nunez and Oke 1977; Oke et al. 2017 amongst others):

$$Q^* = Q_H + Q_E + Q_G \qquad [W\ m^{-2}] \qquad (Eq\ 2.1.)$$

In Equation (2.1.), the term Q^* corresponds to the "net all-wave radiation" whereas Q_H is the "sensible heat flux"; Q_E is the "latent heat flux" and Q_G is the "conductive heat flux" (Arnfield 2003; Mirzaei and Haghighat 2010).

For the urban condition, to explore more than a single surface, the "energy balance" calculation is performed for a "volume", and is represented as (Ali-Toudert 2021; Arnfield 2003; Barlow 2014; Mirzaei and Haghighat 2010; Oke 1988; Oke et al. 2017; Voogt 2017 amongst others):

$$Q^* + Q_F = Q_H + Q_E + \Delta Q_S + \Delta Q_A \qquad [W\ m^{-2}] \qquad (Eq.\ 2.2.)$$

In Equation (2.2.), Q_F corresponds to the "anthropogenic heat release" whereas ΔQ_S is the "storage heat flux" and ΔQ_A is the "net advection" (Mirzaei and Haghighat 2010; Rizwan et al. 2008).

The term "sensible heat flux, Q_H" stems from different atmospheric and surface temperatures (Grimmond et al. 2010; Oke et al. 2017). Its ratio to the "latent heat flux, Q_E" is identified as the "Bowen ratio – β" (Q_H/Q_E) (Oke 1988; Oke et al. 2017; Rizwan et al. 2008; Taha 1997). β tends to be greater in urban environments at which more surfaces are sealed, green spaces are scarcer and large amounts of run-off water is observed (Voogt 2017). In parallel with that, according to Oke et al. (2017), it refers to a warming trend when β is greater than 1, and to a cooling trend as well as more humid conditions when smaller (Oke et al. 2017).

The term "anthropogenic heat release, Q_F" results from activities of the dwellers (see, for instance, Ali-Toudert 2021; Arnfield 2003; Grimmond et al. 2010; Oke et al. 2017; Rizwan et al. 2008; Taha 1997; Voogt 2017) and can contribute to the formation of UHIs (see, for instance, EPA 2008; Oke 1982; 1995; Rizwan et al. 2008; Taha 1997). According to Taha (1997), they are generally greater in the cold season, specifically in developed parts of the urban settings with cold climates (Taha 1997).

The term "net advection - ΔQ_A" is widely "neglected" in "energy balance" calculations (see, for instance, Oke et al. 2017, Rizwan et al. 2008; Voogt 2017). According to Grimmond et al. (2010), inhomogeneities in the physical near-surface environment lead to its formation and it is not yet extensively addressed by and investigated in neighbourhood-scale inquiries (Grimmond et al. 2010).

The term "storage heat flux - ΔQ_S" (Oke et al. 2017) is considered for each element within the investigated domain (i.e., the "volume") as well as the air (Arnfield 2003; Oke et al. 2017). According to Grimmond et al. (2010), the term corresponds to a maximum of 40-50 % of the Q* in urban environments, whereas in other regions the "soil heat flux" (p. 253) only makes up around 5% (Grimmond et al. 2010).

In this context, Oke et al. (2017) argues that the literature had widely associated the "urban materials" with higher heat storage characteristics of urban settings in the past where first studies stated UHIs mainly stemmed from these dynamics. However, according to Oke et al. (2017), the enhanced heat storage tendencies in the urban domain stem from a combined influence of "moisture" (p. 168), "form" (p. 168) and "thermal properties" (p. 168) and cannot be solely attributed to the "urban-rural" (p. 168) difference of the latter (Oke et al. 2017).

In this context, the urban dynamics and characteristics that influence how the input heat is shared among Q_H, Q_E and Q_S can be summarized as follows (Grimmond et al. 2010; Oke et al. 2017; Voogt 2017): The built environment in urbanized regions introduces an increase in the surface area, which is covered with artificial materials. Also, more surfaces are sealed in inhabited areas such as the ones for roads or parking lots. These "urban" surfaces are commonly covered by materials associated with rapid heat transfer and storage tendencies. Together with the greater surface area, this contributes to the increases in heat storage behaviours of the urban domain. The geometrical organization of the built environment also influence the airflow, especially within denser urbanized locations. This potentially alters the distribution of heat within the near-surface layer. Less vegetative elements, i.e., fewer trees or green spaces, as well as less pervious cover in general, decrease the chance of cooling via evaporation and evapotranspiration. All these parameters influence the individual share of Q_H, Q_E and Q_S and potentially control the thermal environment one experiences within the UCL (Grimmond et al. 2010; Oke et al. 2017; Voogt 2017).

2.2.3. Microclimate dynamics: Radiation budget

Objects with temperatures above the 0 K threshold emit "electromagnetic radiation" at all times (see, for instance, Lillesand et al. 2015; Oke et al. 2017). The intervals of the wavelengths, by which the radiation travels, is shown by the "electromagnetic spectrum (CCRS 2019; Lillesand et al. 2015) and is illustrated in Figure 2 (NASA_Weather 2021).

In this context, Planck's Law specifies the radiation an object emits for a certain wavelength for a certain temperature (Oke et al. 2017). Based on this, according to Wien's Displacement Law (Eq. 2.3.), one can determine the wavelength at which blackbodies emit most for a specific temperature (Lillesand et al. 2015). Wien's Displacement Law also indicates that, this wavelength is inversely proportional with the temperature: it corresponds to longer wavelengths for lower temperatures and vice versa (Lillesand et al. 2015).

$$\lambda_m = A / T \qquad [\mu m] \qquad \text{(Eq. 2.3.)}$$

In Equation (2.3.), λ_m refers to the wavelength at which the maximum emission occurs at temperature T (in kelvin). A is a constant with a value of 2898 µm/K (Lillesand et al. 2015).

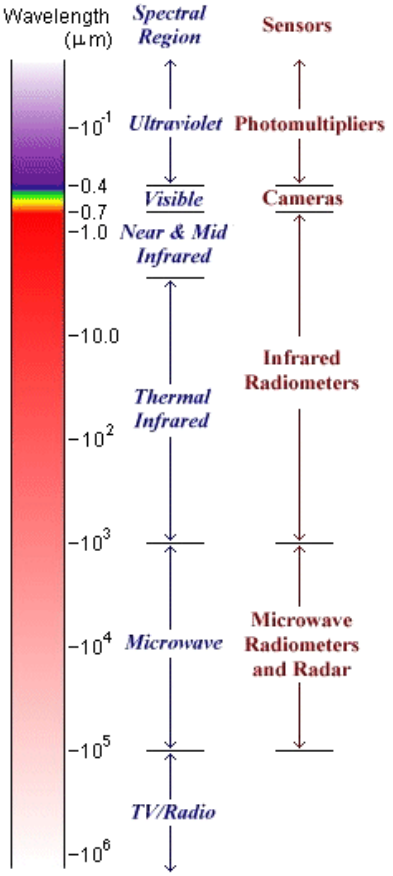

Figure 2. Electromagnetic spectrum (source: NASA_Weather (2021) - adapted)

Based on the afore-mentioned principles, as Oke et al. (2017) points out, there occurs a distinction in the wavelengths that the Sun and the Earth emit the biggest portion of their radiation. Due to much higher temperatures, the Sun emits mostly in shorter wavelengths, whereas the Earth in longer (Oke et al. 2017). According to Oke et al. (2017), this is the physical basis behind the different identification of the radiation emitted by the Sun ("shortwave" or "solar" (p. 123)) and the Earth ("longwave", "terrestrial", "thermal infrared" (p. 123)) (Oke et al. 2017).

Furthermore, as Oke et al. (2017) states, when we look at the radiation emitted by the Sun, the distribution lies mainly between 0.1 and 3 µm, whereas for the Earth, it is between 3 and 100 µm (Oke et al. 2017). This distinction also points out to a certain threshold around 3 µm which mainly separates the radiation emitted by and reflected from the surface (Lillesand et al. 2015). This principle is discussed further in detail in the following parts of this chapter in the context of the remote sensing method.

2.2.3.1. Surface radiation budget: Principles

The term Q* in Equations (2.1.) and (2.2.) can be derived from the surface radiation budget below (Eq. 2.4) (Ali-Toudert 2021; Grimmond et al. 2010; Oke et al. 2017 amongst others):

$$Q^* = K^* + L^* = K\downarrow - K\uparrow + L\downarrow - L\uparrow \qquad [W\,m^{-2}] \qquad (Eq.\ 2.4.)$$

In Equation (2.4.), the terms *K** and *L** correspond to "net shortwave radiation" and "net longwave radiation" respectively, whose components are shortwave (*K*) and longwave (*L*) radiation coming to (↓) and leaving from (↑) the surfaces (Grimmond et al. 2010).

In Equation (2.4.), $K\downarrow$ is identified as the "shortwave irradiance" (Oke et al. 2017). Parameters such as the atmospheric conditions (cloud conditions, pollutant concentrations, atmospheric composition), solar geometry (Grimmond et al. 2010; Oke et al. 2017) as well as the characteristics and positioning of the immediate site geometry (Oke et al. 2017) contribute to the amount of $K\downarrow$ that arrives a surface.

In Equation (2.4.), $K\uparrow$ is the "outgoing shortwave radiation" (Rizwan et al. 2008) and mainly can be represented as (Oke et al. 2017):

$$K\uparrow = \alpha \cdot K\downarrow \qquad [Wm^{-2}] \qquad (Eq.\ 2.5.)$$

In Equation (2.5.), the term α refers to the albedo of the "surface" that K↓ is incident upon (Oke et al. 2017).

Albedo is a commonly explored feature in inquiries in the field of urban climate and/ or building energy performance (see, for instance, Akbari and Matthews 2012; Wang et al. 2016; Yuan et al. 2015). Taha (1997) defines the **albedo (α)** of a medium based on "its hemispherically- and wavelength-integrated reflectivity" (Taha 1997, p. 100).

In a general sense, materials with higher albedo values are favoured in urban environments to increase the $K\uparrow$ which can assist in preventing the overheating (see, for instance, Akbari and Matthews 2012; Wang et al. 2016; Taha 1997; Yuan et al. 2015).

The parameters that influence the albedo values of the urbanized settings are the material-based properties and the geometrical features (see, for instance, Ali-Toudert 2021; Grimmond et al. 2010; Oke et al. 2017). The colour of a material (light vs. dark), its texture (Ali-Toudert 2021; Grimmond et al. 2010) as well as its moisture condition (wet vs. dry) has a role on the albedo value (Grimmond et al. 2010; Oke et al. 2017).

In this context, Table 1 provides the albedo values of some common surface types and materials found in urban and rural domains based on Oke et al. (2017). Note that a more extensive and complete version of this table is presented in Oke et al. (2017) and the presented information is based on the works by Arnfield (1982); Bailey et al. (1997); Bretz et al. (1998); Gubareff et al. (1960); Maykut (1985); Oke (1987) and (1988), as cited by Oke et al. (2017).

Table 1. Albedo values for selected materials and surface types (source: Oke et al. (2017) p.129 Table 5.1. – modified. See above text for the list of references cited by Oke et al. (2017))

Surface type	**Surface and material properties**	**Albedo (α) range***
Soils	from dark coloured and wet to light coloured and dry	0.05 – 0.30
Vegetation	from bare deciduous forests to short grass	0.13 – 0.26
Road surfaces	from fresh asphalt to certain concrete types	0.05 – 0.35
Wall surfaces	from red coloured bricks to certain limestone types	0.20 – 0.64
Roof surfaces	from dark coloured shingles to fresh clay tiles	0.05 – 0.35
	from certain types of corrugated iron to new galvanized steel	0.10 – 0.45
Metals	polished metal surfaces	0.50 – 0.90

* Represented values are the lowest and highest albedo values reported in Oke et al. (2017) at p.129 Table 5.1., for the respective surface types. For instance, based on Oke et al. 2017, dark coloured and wet soils have an albedo range of **0.05** – 0.10, whereas light coloured and dry soils have a range of 0.18 – **0.30**. In the above table, the lowest and highest values of these two intervals are presented.

Looking back to Equation (2.4.), the term $L\downarrow$ is identified as the "incoming longwave radiation" (see, for instance, Ali-Toudert 2021; Arnfield 2003).

$L\downarrow$ tend to be greater in urbanized settings (Arnfield 2003, Oke 1982; Grimmond et al. 2010). This stems from the increased amount of pollutants within the urban atmosphere (Ali-Toudert 2021; Arnfield 2003; Oke 1982; Grimmond et al. 2010); as well as the higher temperature profiles within cities (Arnfield 2003; Grimmond et al. 2010; Voogt 2017).

In Equation (2.4.), the term $L\uparrow$ is identified as the "outgoing longwave radiation" and is controlled by the urban geometry (in particular, sky view factor (SVF)), emissivity (ε), and the temperature of the surfaces (Ali-Toudert 2021; Grimmond et al. 2010).

In this context, Stefan-Boltzmann Law (Equation 2.6.) determines "total energy flux density (i.e., "emittance")" (Oke et al. 2017) which is closely related with the object's temperature (Lillesand et al. 2015).

$$E = \varepsilon \sigma T^4 \qquad [W\ m^{-2}] \qquad \textit{(Eq. 2.6.)}$$

In Equation (2.6.), ε corresponds to the object's mean "emissivity", T refers to the temperature of the object and σ is a constant identified as the "Stefan-Boltzmann constant" which corresponds to $5.67 \cdot 10^{-8}$ $Wm^{-2}K^{-4}$ (Oke et al. 2017).

The term $L\uparrow$ of the Equation (2.4.) then can be calculated as (Oke et al. 2017):

$$L\uparrow = \varepsilon \cdot\sigma\cdot T_0^4 + (1 - \varepsilon) \cdot L\downarrow \qquad [W\ m^{-2}] \qquad \text{(Eq. 2.7.)}$$

In Equation (2.7.), the term T_0 refers to the surface's "absolute temperature" (Oke et al. 2017).

In this context, the "**emissivity - ε**" determines the radiative capabilities of a medium (see, for instance, Lillesand et al. 2015; Mahdavi et al. 2013; Oke et al. 2017). The "emissivity" has a range from 0 to 1, i.e., from no emission to a full-emission, and for "blackbodies" it corresponds to 1 (see, for instance, Lillesand et al. 2015; Oke et al. 2017).

Table 2. provides the emissivity values (for broadband-longwave) of some common surface types and materials found in urban and rural domains based on Oke et al. (2017). Note that, similar to Table 1, Table 2 stems from a more detailed version presented by Oke et al. (2017). The information conveyed below in Table 2 is based on Arnfield (1982); ASHRAE (2009); Oke (1987) and (1988); Campbell and Norman (1998); Wittich (1997), as cited by Oke et al. (2017).

Table 2. Emissivity values (broadband-longwave) for selected materials and surface types (source: Oke et al. (2017) p.130 Table 5.2. – modified. See above text for the list of references cited by Oke et al. (2017))

Surface type	Surface and material properties	Emissivity (ε) range
Soils	from light coloured and dry to dark coloured and wet	0.89 – 0.98
Vegetation	from short grass to long grass	0.90 – 0.98
	from bare deciduous forest to leaved deciduous forest	0.90 – 0.99
Road surfaces	asphalt	0.89 – 0.96
	concrete	0.85 – 0.97
Wall surfaces	from red coloured bricks to white coloured bricks	0.90 – 0.92
Roof surfaces	shingles and tiles	0.90
	corrugated iron	0.13 – 0.28
Metals	polished metals	0.02 – 0.06

2.2.4. Employed methods in urban climate studies

Guided by the afore-mentioned principles, research efforts that explore urban climate inquiries follow a wide-range of approaches depending on the research problem, type and availability of the required data, feasibility-related aspects, amongst other considerations (see, for instance, Aleksandrowicz et al. 2017; Mirzaei and Haghighat 2010).

In this context, Mirzaei and Haghighat (2010) provides a comprehensive overview regarding the methods employed in the UHI inquiries by discussing the benefits and drawbacks associated with each. They categorize these methods under observation- and simulation-based efforts (Mirzaei and Haghighat 2010), in-line with the building-physics investigations – and many other disciplines.

Similar with Oke (1984), Mirzaei and Haghighat (2010) points out the necessity to identify the "scale" associated with the explored research problem in UHI studies. According to the Mirzaei and Haghighat (2010), the idea behind this is to prevent considering parameters which theoretically would not make a notable impact on the investigated domain. This would allow for an optimal use of the research resources as the urban domain is a complex entity and thus, is challenging to investigate (Mirzaei and Haghighat 2010).

Although this remark by Mirzaei and Haghighat (2010) was primarily intended for UHI investigations, it can nevertheless be applied to any effort studying various other urban climate related aspects. This perspective is further evaluated in the next chapter, in the context of selecting the spatial extents of the investigated study areas for the present dissertation. In this context, Mirzaei and Haghighat (2010) divides observation-based methods into three further groups:

- the methods which rely on in-situ detection and documentation of the investigated parameters (i.e., "field measurements" (Mirzaei and Haghighat 2010),
- the methods which gather data through employment of aerial platforms or satellites with no actual contact to the investigated domain (i.e., "thermal remote sensing" (Mirzaei and Haghighat 2010); see also Lillesand et al. 2015; Toth and Jóźków 2016),
- the methods which imitate and employ a scaled physical version of the study domain through "small-scale modelling" (Mirzaei and Haghighat 2010).

Amongst these methods, in-situ observations are commonly employed, either as a sole approach or together with other empirical or computational techniques (Mirzaei and Haghighat 2010; see also Coseo and Larsen 2014; Kantzioura et al. 2015; Krüger 2015; Lim et al. 2014; Mahdavi et al. 2014; Maleki et al. 2012; Ngarambe et al. 2021; Paulina et al. 2015; Rotach et al. 2005; Shi and Zhang 2022; Skarbit et al. 2017 amongst others).

In-situ observations of the climatic variables are specifically advantageous regarding reliability-based concerns, such as precision and accuracy of the measurements. Moreover, these observation settings have the potential to provide this supreme data quality over long temporal periods that can span many decades. This is specifically common through organizational station networks (for instance, WMO 2018; WMO_OSCAR 2022a; ZAMG 2022a; see also Stewart 2011).

Meteorological stations allow for the detection of many parameters such as air temperature at various heights, humidity, wind speed/ direction, radiation, state and concentration of the atmospheric pollutants, and precipitation (Mirzaei and Haghighat 2010; WMO 2018; WMO_OSCAR 2022a). These stations can be stationary (both long-term and short-term), or can be mounted on mobile platforms, i.e., "mobile traverses" (EPA 2008; Mirzaei and Haghighat 2010; see also Irger 2014; Lim et al. 2014; Maleki et al. 2012).

Stewart (2011) includes a critical overview regarding the employment of these sensors in data collection for UHI studies (canopy-level) with the aim of providing a reliable standardization among the UHI researchers and respective publications (Stewart 2011). Likewise, such as Oke (2006) and WMO (2018), World Meteorological Organization (WMO) provides detailed guidelines towards obtaining reliable, comparable, and sustainable measurements of climatic parameters in order to establish a robust network across the globe to detect climatic tendencies and events (Oke 2006; WMO 2018; WMO_IMOP 2020; WMO_OSCAR 2022a; see also Stewart 2011; WMO 2022).

In Austria, Zentralanstalt für Meteorologie und Geodynamik (ZAMG), together with its partnering organizations, provides a well-established meteorological network which meets the WMO standards (ZAMG 2022a; 2022b). Further details regarding ZAMG observations are provided in the next chapter, in relation with the data collection and research design of the present dissertation.

On the other hand, computational inquiries of the urban climate investigations are widely applied as well (see, Han et al. 2015; Kaloustian and Diab 2015; Salata et al. 2016; Tsoka 2017; Vuckovic et al. 2017 amongst others) and address various-scale settings, from building-based assessments to micro- and meso-scale models (Mirzaei and Haghighat 2010; Sola et al. 2018).

In the intersection of urban climate and building-energy/ comfort inquiries, Schneider dos Santos et al. (2016) provide a detailed perspective on the present efforts that address the application potentials of urban warming to the building-based thermal assessment tools. The authors specifically explore the "weather data" generation alternatives for this purpose, by investigating employment of micro-, global- and regional-scale models as well as in-situ and remotely-sensed data collection techniques (Schneider dos Santos et al. 2016; see also Crawley and Barnaby 2019).

In the light of these points, it is a common practice in urban climate research to employ the afore-mentioned methods solely or in different combinations with each other (Mirzaei and Haghighat 2010). Considering the data collection and analyses steps of the present dissertation, the next section conveys a detailed perspective on the (thermal) remote sensing method.

2.3. Thermal remote sensing method

2.3.1. Background & principles

As Lillesand et al. (2015) describes, remote sensing is a data collection and analysis method which the instrument carrying out the data collection has no direct contact with the inspected medium (Lillesand et al. 2015; Toth and Jóźków 2016). The "distributions" of electromagnetic radiation or sound-waves are examples to the kind of information acquired via remote sensing (Lillesand et al. 2015).

As Lillesand et al. (2015) delineates, the method relies on the characteristic behaviours of "earth features" whose abundantly different material-based properties lead to distinctive energy-transfer behaviours, such as different fractions of transmitted, absorbed and reflected components. As the authors depict, variations in these fractions respond to different wavelengths and this holds true among the elements of the same kind as well (Lillesand et al. 2015).

Lillesand et al. (2015) remarks that, these principles are utilized by remote sensing to facilitate identifying specific elements within the remotely-sensed images, such as the way different colors are perceived by humans (Lillesand et al. 2015).

In this context, the short- and long-wave radiation principles mentioned earlier, namely, the threshold around 3 µm wavelength that mainly separates the reflected and emitted radiation from earth surfaces (Lillesand et al. 2015; Oke et al. 2017) becomes significant. "Nonphotographic" sensors are employed above this threshold in remote sensing to detect the emitted long-wave radiation (Lillesand et al. 2015).

Considering the afore-mentioned characteristics and "atmospheric windows" that only allow the transmission of certain wavelengths, 3-5 µm and 8-14 µm intervals are employed by the thermal remote sensing sensors to detect the radiation emitted via earth surfaces (Lillesand et al. 2015; see also Oke et al. 2017). This is carried out by means of a range of different platforms, and Toth and Jóźków (2016) provides a relatively recent overview (which does not solely focus on thermal remote sensing, but remote sensing in general) by grouping them into satellites, aircrafts, drones, vehicles, and stationary platforms (Toth and Jóźków 2016).

As already mentioned, the present dissertation is mainly concerned with the application of satellite-based (thermal) remote sensing. Therefore, in the following parts of this chapter, the focus is given to satellite-based thermal sensors and land surface temperatures derived through them, as well as research efforts that employ satellite-based thermal data in their inquiries.

2.3.2. Satellite platforms

Remotely sensed thermal data of earth surfaces are available through a range of satellite sensors with different acquisitional capabilities, and sources such as Tomlinson et al. (2011) and Almeida et al. (2021) provide a good initial perspective regarding the ones commonly employed in UHI (Almeida et al. 2021) and climate-related inquiries (Tomlinson et al. 2011).

According to Almeida et al. (2021), thermal sensors of Landsat satellites, MODIS sensors of Terra and Aqua satellites as well as ASTER sensor of Terra satellite are the ones more frequently employed for land surface temperature (LST) investigations in UHI studies (Almeida et al. 2021; Aqua 2022; ASTER 2022; Landsat 2022; MODIS 2022a; Terra 2022).

Main details regarding these satellite-based TIR sensors are presented in Table 3 below.

Table 3. Information on selected satellite-based TIR sensors (sources: adapted from Almeida et al. (2021); Tomlinson et al. (2011) (as cited in Almeida et al. 2021); WMO_OSCAR 2022b (as cited in Almeida et al. 2021); partially based on LP DAAC_ASTER 2022; USGS_Landsat 2022)

Satellite SENSOR	Availability	Wavelengths (µm)	Spatial resolution	Revisit time
Landsat 4 TM	1982 - 1993	10.40 - 12.50	120m (Provided in 30m)	16 days
Landsat 5 TM	1985 - 2013	10.40 - 12.50	120m (Provided in 30m)	16 days
Landsat 7 ETM+	1999 - (…)	10.40 - 12.50	60m (Provided in 30m)	16 days
Landsat 8 TIRS	2013 - (…)	10.60 - 11.19 11.50 - 12.51	100m (Provided in 30m)	16 days
Landsat 9 TIRS2	2022 - (…)	10.60 - 11.19 11.50 - 12.51	100m (Provided in 30m)	16 days
Terra ASTER	1999 - (…)	8.125 - 8.475 8.475 - 8.825 8.925 - 9.275 10.25 - 10.95 10.95 - 11.65	90m	Twice a day (Irregular acquisitions) operational on-demand
Terra MODIS	1999 - (…)	10.78 - 11.28 11.77 - 12.27	~ 1000m	Twice a day
Aqua MODIS	2002 - (…)	10.78 - 11.28 11.77 - 12.27	~ 1000m	Twice a day

The satellite-based TIR sensors presented in Table 3 is a small portion of the total available satellite sensors that LST can be derived from (Almeida et al. 2021). As pointed out by Almeida et al. (2021), other available satellite-based platforms and resources can be explored through platforms such as WMO OSCAR (Observing Systems Capability Analysis and Review Tool) (Almeida et al. 2021; WMO_OSCAR 2022b). WMO OSCAR includes a comprehensive database that allows users to perform inquiries based on criteria such as satellite characteristics, temporal data availability, acquired parameters, spatial limits, and so on (Almeida et al. 2021; WMO_OSCAR 2022b).

As it can be derived from Table 3, thermal data provided by these sensors are either more frequently available (lower revisit interval) or provide a more detailed spatial view of the investigated domain (higher spatial resolution) (see, for instance, Sobrino et al. 2012). This becomes even more evident in geostationary satellites, such as MSG SEVIRI which has a 15-minute temporal resolution but provides spatial details with a 3 km resolution for nadir (Benas et al. 2017) and 5-6 km over Central Europe (Zakšek and Schroedter-Homscheidt 2009), lower than any of the sensors listed on Table 3 (Almeida et al. 2021). This is an ongoing dilemma in satellite-based remote sensing research, which becomes even a more complex research design issue when the investigated domain is a dynamic entity like the urban thermal environment (see, for instance, Sobrino et al. 2012). For instance, Yoo et al. (2018) mentions a similar concern towards employing Landsat in air temperature inquiries within the urban areas because of the long revisit-cycles of the satellites (Yoo et al. 2018) although their spatial resolution is favourable for urban climate investigations.

In this context, the following parts of this background includes a brief overview of selected previous efforts which employed thermal remote sensing in their inquiries. In this overview, more attention is given to the works that employed Terra and Aqua MODIS data in their assessments, due to their sufficient temporal coverage (see Table 3) as well as rich diurnal availability of their acquisitions (two day-time and two night-time acquisitions when both satellites are utilized) (Aqua 2022; MODIS 2022a; Salomonson et al. 1989; Terra 2022; see also Firat Ors and Mahdavi 2021). Considering these points, a brief information regarding these two satellite sensors and the characteristics of the LST data derived from them are provided below.

2.3.3. Terra and Aqua MODIS

Thermal data acquired via Moderate Resolution Imaging Spectroradiometer (MODIS) sensors can be accessed from the dates 24.02.2000 and 04.07.2002 for Terra and Aqua respectively (MOD11A1_Data 2022; MYD11A1_Data 2022; Wan 2014).

MODIS sensors onboard these two satellites operate at 705 km altitude, on "circular", "sun-synchronous" and "near-polar" orbits. Each day, the satellites move over the Equator three hours apart from each other, with Terra crossing earlier at 10:30 a.m. and Aqua at 01:30 p.m. in UTC time (LAADS DAAC 2022; MODIS 2022b amongst others).

MODIS sensors operate for both day-time and night-time acquisitions. They gather information through 36 bands, and with 250 m, 500 m or 1 km spatial resolutions depending on the employed band (LAADS DAAC 2022; MODIS 2022b).

Various combinations of MODIS bands are utilized in different fields of observations. Table 4 below presents an overview regarding the instrument's capabilities and characteristics.

Table 4. MODIS Bands and primary areas of application (sources: LAADS DAAC 2022; MODIS 2022b, modified)

Primary application	Spatial resolution	Band	Bandwidth (nm)
Land/Cloud/ Aerosols Boundaries	250 m	1	620 - 670
		2	841 - 876
Land/Cloud/ Aerosols Properties	500 m	3	459 - 479
		4	545 - 565
		5	1230 - 1250
		6	1628 - 1652
		7	2105 - 2155
Ocean Colour/ Phytoplankton/ Biogeochemistry	1000 m	8	405 - 420
		9	438 - 448
		10	483 - 493
		11	526 - 536
		12	546 - 556
		13	662 - 672
		14	673 - 683
		15	743 - 753
		16	862 - 877
Atmospheric Water Vapor	1000 m	17	890 -920
		18	931 - 941
		19	915 - 965

Table 4. (cont.) MODIS Bands and primary areas of application (sources: LAADS DAAC 2022; MODIS 2022b, modified)

Primary application	Spatial resolution	Band	Bandwidth (µm)
Surface/ Cloud Temperature	1000 m	20	3.660 - 3.840
		21	3.929 - 3.989
		22	3.929 - 3.989
		23	4.020 - 4.080
Atmospheric Temperature	1000 m	24	4.443 - 4.498
		25	4.482 - 4.549
Cirrus Clouds Water Vapor	1000 m	26	1.360 - 1.390
		27	6.535 - 6.895
		28	7.175 - 7.475
Cloud Properties	1000 m	29	8.400 - 8.700
Ozone	1000 m	30	9.580 - 9.880
Surface/ Cloud Temperature	1000 m	31	10.780 - 11.280
		32	11.770 - 12.270
Cloud Top Altitude	1000 m	33	13.185 - 13.485
		34	13.485 - 13.785
		35	13.785 - 14.085
		36	14.085 - 14.385

2.3.3.1. MODIS data characteristics

MODIS datasets are provided with different levels of processing, as it is a common practice among satellite-based data providers (see, for instance, Wolfe et al. 1998; Young et al. 2017). Wolfe et al. (1998) describe the main processing steps differentiating the MODIS "land" category data types (which, land surface temperature is a part of) with different levels of complexity. As the authors delineate, Level 0 data refers to the unprocessed MODIS acquisitions which later go through a calibration and geolocation process to obtain the Level 1 data. This Level 1 data is further processed utilizing specific algorithms to attain the pertinent "geophysical parameter" (such as land surface temperature). Level 2 data conveys this computed parameter (Wolfe et al. 1998).

On the other hand, as Wolfe et al. (1998) depict, Level 3 data is the most sophisticated data category. It is generated utilizing a certain coordinate system, by "gridding" and/or "compositing" the Level 2 data (Wolfe et al. 1998).

As Wolfe et al. (1998) describe, this categorization also leads to differences in the format these data types are distributed. Level 1 and Level 2 data are provided as "granules" which have a spatial extent of, about, 2340 km to 2000 km. They belong to 5-minute-long operations of the MODIS sensors (Wolfe et al. 1998). On the other hand, Level 3 data are provided to users in a "grid" system that create "fixed, nonoverlapping, earth-located tiles" (Wolfe et al. 1998, p. 1327). As Wolfe et al. (1998) describe, these Level 3 data "tiles" are structured in various map projections and have, around, a 1200 km to 1200 km spatial extent. A total of 326 tiles belong to "land" locations around the world. The "grid cells" building these "tiles" correspond to the pixels of the Level 3 data (Wolfe et al. 1998; see also Grant 2017).

In this context, further details regarding the MODIS grid system employed in the "land" products, which include the land surface temperature data, can be reached from MODLAND (2021a). Relevant conversions such as the individual MODIS tile that corresponds to a certain earth location ("geographic coordinate") for a specific spatial resolution and "map projection" (also vice-versa) can be accessed through MODLAND (2017).

2.3.3.2. Land surface temperature: MODIS data

Prata et al. (1995) provide a detailed overview regarding the land surface temperature (LST) retrieval by means of satellite-based thermal remote sensing platforms. As the authors delineate, a wide-range of investigations employ LST including evapotranspiration assessments and frost monitoring, inquiries of thermal inertia or crop health, as well as predictive computations of sea-breezes and clouds (Prata et al. 1995; see also Li et al. 2013 amongst others). As Prata et al. (1995) further emphasize, LST is also essential for proper modelling of the surface energy budget (Prata et al. 1995; see also Li et al. 2013; Voogt and Oke 2003; Weng 2009 amongst others).

Likewise, Voogt and Oke (2003) point out the significance of LST in urban climate investigations due to its influence on parameters such as near-surface air temperature (T_{air}), indoor-

and outdoor-comfort conditions and suggest its significance to the surface energy balance (Voogt and Oke 2003; see also Li et al. 2013; Wan 2008; 2014; Weng 2009 amongst others).

Currently, there are two main LST product families available through MODIS acquisitions which are MOD21 and MOD11 (MYD 21 and MYD 11 respectively, for Aqua MODIS) products. These products differ from each other mainly regarding the approaches they are computed with (MOD21 2022).

MOD21 (MYD21) product group is the more recent one and currently tagged with the "stage 1" "maturity" (MOD21 2022; MOD21_Data 2022). As MODLAND (2021b) describes, this "stage 1 validation" refers to the condition that their accuracy is explored with respect to field data or other meaningful information for a limited number of case locations as well as temporal intervals (MODLAND 2021b).

On the other hand, MOD11 (MYD11) data group is referred to as the "heritage LST product" (MOD11 2022) and are currently tagged with "stage 2" "maturity" (MOD11A1_Data 2022; MYD11A1_Data 2022). As MODLAND (2021b) describes, in "stage 2 validation" process, the accuracy is evaluated employing field data or other meaningful information for a "significant" number of case locations, also temporal intervals. Furthermore, the products go through a series of "consistency" assessments for temporal and spatial considerations, and with respect to other relevant products. These assessments are performed for "globally representative" settings, as well as temporal intervals. Also, the outcomes from the afore-mentioned efforts are disseminated in the peer-reviewed publications (MODLAND 2021b).

Considering these points, the focus is given to the MOD11 (MYD11) data group in the overview below.

2.3.3.3. MOD11/MYD11 LST data

MOD11 (MYD11) LST data (hereafter M*D11) consist of nine LST products with different processing levels (Table 5) (Wan 2013). According to Wan (2013), "daily" LST computations are performed by either the "generalized split-window LST algorithm" (Wan and Dozier 1996) or the "day/night LST algorithm" (Wan and Li 1997), depending on the product type (Wan 2013). An overview of the M*D11 data types is presented in Table 5.

Table 5. MOD11(MYD11) products available for Collection 6 (source: Wan 2013, modified)

Product	Level	Spatial resolution	Temporal resolution	LST algorithm
M*D11_L2	2	1 km (at nadir)	swath (scene)	generalized split-window
M*D11A1	3	1 km (actual 0.928 km)	daily	generalized split-window (from MOD11_L2)
M*D11B1	3	6 km (actual 5.568 km)	daily	day/night
M*D11B2	3	6 km (actual 5.568 km)	8 days	day/night (from MOD11B1)
M*D11B3	3	6km (actual 5.568 km)	monthly	day/night (from MOD11B1)
M*D11A2	3	1 km (actual 0.928 km)	8 days	generalized split-window (from MOD11A1)
M*D11C1	3	0.05° by 0.05°	daily	day/night ["supplemented" by generalized split-window] (from MOD11B1)
M*D11C2	3	0.05° by 0.05°	8 days	day/night ["supplemented" by generalized split-window] (from MOD11C1)
M*D11C3	3	0.05° by 0.05°	monthly	day/night ["supplemented" by generalized split-window] (from MOD11C1)

As Table 5 indicates, the products which, both spatially and temporally, offer more enhanced detail (i.e., MOD11_L2 and MOD11A1) stem from the "generalized split-window algorithm" (Wan 2013). Due to these temporal and spatial observation capabilities, they can be regarded as better candidates (among the products presented in Table 5) for the urban climate assessments in-line with the goals of the present dissertation.

In this context, Wan (2008) describes the LST data provided by M*D11 products as follows:

> "In the MODIS LST product, LST is the radiometric (kinetic) temperature related to the thermal infrared (TIR) radiation emitted from the land surface observed by an instantaneous MODIS observation."
>
> (Wan 2008, p. 60).

Wan (2008) further explains that the LST computed from MODIS acquisitions is specific for the viewing angle of the acquisition and corresponds solely to "the radiometric temperature at the given viewing angle" (Wan 2008, p.60).

In the light of these points, Equation 2.8 is utilized to obtain the Level-2 LST via the "generalized split window algorithm" (Wan and Dozier 1996) as represented below (Wan 2014):

$$LST = b_0 + [b_1 + b_2 \cdot ((1-\varepsilon)/\varepsilon) + b_3 \cdot (\Delta\varepsilon/\varepsilon^2)] \cdot ((T_i + T_j)/2) + [b_4 + b_5 \cdot ((1-\varepsilon)/\varepsilon) + b_6 \cdot (\Delta\varepsilon/\varepsilon^2)] \cdot ((T_i - T_j)/2) \quad [Eq.\ 2.8]$$

In Equation (2.8), the terms b_0 to b_6 are coefficients based on "water vapor", "atmospheric surface temperature" and "viewing zenith angle" (Wan 2014). The term ε refers to the mean emissivity value of band 31 and band 32, whereas Δε denotes their difference, with i = 31 and j = 32 (Wan 2014). The term T corresponds to the "brightness temperature" at the respective MODIS bands (Wan 2014). Note that, for pixels that are classified as "bare soil", there is a slight modification in the algorithm introduced with Collection-6, as presented in Wan (2014).

In this context, the emissivity values employed by MODIS Band 31 and Band 32 can be accessed from Wan (2008) (see Wan 2008, p.62, Table 2). As Wan (2008) delineates, these emissivity values are largely according to the model by Snyder et al. (1998) and relies on the land cover classification of the observed pixels (Wan 2008; see also Snyder et al. 1998).

2.4. Overview of previous efforts: T_{air} estimation

In the light of the afore-mentioned principles related with the urban climate, thermal remote sensing method and respective data sources, this section of the present dissertation aims to convey a concise overview of the tendencies, goals, and findings of the selected previous efforts that explored estimating near-surface air temperatures.

In this context, Zakšek and Schroedter-Homscheidt (2009) list the methods pursued in deriving screen-level air temperature (i.e., T_{air}), which can be regarded amongst the main research goals of the present dissertation, under four main themes. These are "simple-", and "advanced statistical approaches", "temperature-vegetation index (TVX) approach", and finally, the "energy-balance approaches" (Zakšek and Schroedter-Homscheidt 2009, p. 415; see also Benali et al. 2012 amongst others).

Each of these groups of techniques have certain potentials or limitations regarding the characteristics of the studied domain, type and source of the required data or the goals addressed by the studies employing them (see, for instance Benali et al. 2012; Yoo et al. 2018; Zakšek and Schroedter-Homscheidt 2009) and this is tried to be addressed below.

As Zakšek and Schroedter-Homscheidt (2009) describe; the differentiation between simple and advanced statistical techniques is mainly the number of independent variables explored in T_{air} calculations. Efforts to derive T_{air} through a simple linear regression with LST are considered as simple statistical procedures, whose disadvantage – according to Zakšek and Schroedter-Homscheidt (2009) – is the lack of applicability of these models to different samples from other geographic locations than they are originally built for (Zakšek and Schroedter-Homscheidt 2009; see also Benali et al. 2012). On the other hand, a minimum of two independent variables are employed in "advanced statistical approaches", which include machine learning techniques (Zakšek and Schroedter-Homscheidt 2009; see also Benali et al. 2012).

The "temperature-vegetation index (TVX) approach", as Zakšek and Schroedter-Homscheidt (2009) depict, is derived from the assumption that the air temperature within a vegetation canopy that is "infinitely thick" is equal to the surface temperature at the top of that canopy. Thus, the approach benefits from the Normalized Difference Vegetation Index (NDVI) parameter as an

indicator of the amount/ state of the vegetation cover and relies on the "hypothesis" of an inverse linear relationship between the amount of vegetation (more specifically, NDVI) and day-time LST (Zakšek and Schroedter-Homscheidt 2009; see also Benali et al. 2012). Note that, here, NDVI is a "health" indicator of the observed vegetation via remote sensing and is calculated from remote sensing acquisitions in near-infrared, as well as the red portion of the visible wavelengths (EOS 2022).

On the other hand, the last category described by Zakšek and Schroedter-Homscheidt (2009), the "energy balance approaches" are conducted based on the physical principles of the interaction among urban elements, as discussed previously in this chapter (Zakšek and Schroedter-Homscheidt 2009; see for instance Ali-Toudert 2021; Grimmond et al. 2010).

In this framework, Yoo et al. (2018) mention that the TVX approach is not a good alternative for T_{air} estimations within urban areas as they are characteristically scarce in green spaces, and as the application of TVX approach is closely associated with areas of abundant vegetation (Yoo et al. 2018). Furthermore, Yoo et al. (2018) further state that the heterogeneity of the urban domain makes it complicated to apply energy balance techniques for T_{air} estimations, due to the complexity of the surface interactions within these settings (Yoo et al. 2018; see also Ali-Toudert 2021; Grimmond et al. 2010). In this context, Yoo et al. (2018) conclude that advanced approaches such as machine learning and multiple regression are required in these settings to derive T_{air} from satellite-based data sources (Yoo et al. 2018; see also Irger 2014; Schneider dos Santos 2020 amongst others).

In the light of these points, Table 6 below provides an overview regarding the employed techniques and investigated variables by the T_{air} estimation efforts, in relation with the employed satellite sensors and the domains the models are developed for. Note that, here, the completeness of the works from literature that estimate T_{air} is not aimed or claimed. This table is only intended as a medium to convey a general perspective towards the approaches employed in the literature to derive T_{air}. These works are tried to be selected from the literature that deals with more relevant research questions or employs similar parameters and techniques with the present dissertation.

Table 6. Selected previous efforts that estimate T_{air}

Study	Domain	Sensor & LST product	Approach*	Dependent & Independent variables
Zakšek and Schroedter-Homscheidt (2009)	Regional (Central Europe)	SEVIRI, LSA SAF LST (from 5-6 km to 1km)	Surface Energy Balance	T_{air} & LST (multi-temporal), NDVI, albedo, "down-welling short-wave radiation flux", solar angles, relief slope, elevation difference
Benali et al. (2012)	Regional (Portugal)	MODIS, MOD11A1 v5 (1km)	Advanced Statistical Methods	T_{min}, T_{max}, T_{mean} (weekly) & LST-daytime, LST-nighttime, elevation, distance to- coast and freshwater bodies, latitude, Julian day, day length
Irger (2014)	Urban (Sydney, Australia)	Airborne Remote Sensing (2m)	Advanced Statistical Methods (Multiple Regression, Spatial Regression Model)	T_{air} (daytime, nighttime; individually assessed) & impervious surface fraction, vegetated surface fraction (high and medium-height), albedo, LST (daytime, or nighttime; based on the dependent variable), orientation and aspect ratio of urban canyons, distance to coast, sea-level, observation time
Shi et al. (2016)	Regional (South-east USA)	MODIS, MOD11A1 v5, 6 (1km)	Advanced Statistical Methods	T_{mean} (daily) & Ts (calculated as LST/$\varepsilon^{1/4}$), NDVI, urban area percentage, elevation, distance to water
Yoo et al. (2018)	Urban (Los Angeles, Seoul)	MODIS, MOD11A1 v5 (1km) MYD11A1 v5 (1km)	Advanced Statistical Methods (Random Forest)	T_{min}, T_{max} (daily) & LST-day, LST-night, LST-day of previous day, LST-night of previous day, solar radiation, NDVI, elevation, aspect, latitude, longitude, impervious area percentage
Schneider dos Santos (2020)	Urban (London)	MODIS, MOD11A1 v6 (1km)	Advanced Statistical Methods	T_{max} (daily) & LST, SZA, NDVI, BSA, DEM, Julian day, distance to the coast, latitude, longitude

* Based on the classification of Zakšek and Schroedter-Homscheidt (2009)

As summarized in Table 6, Zakšek and Schroedter-Homscheidt (2009) suggested an approach which utilizes energy balance principles and requires no in-situ observation data for deriving screen-level air temperatures with 30-minute and 1km resolution over Central Europe (Zakšek and Schroedter-Homscheidt 2009). As the authors reported, the performance of the proposed approach yielded 2K RMSD (-0.01 K bias) for day-time. The LST data employed in the process consisted of 5-6 km pixels that belong to MSG SEVIRI satellite sensor, which was downscaled to 1km. This downscaling was conducted considering a study area in regional scale ("large geographic regions", p.420), and the authors suggested employing more fine-tuned, additional variables that would consider urban-climate related aspects for downscaling applications in smaller areas such as cities (Zakšek and Schroedter-Homscheidt 2009).

Similar with the present dissertation, Yoo et al. (2018) employed LST data that belong to Terra and Aqua MODIS satellite-sensors, namely, MOD11A1 and MYD11A1 day-time and night-time LST data. They explored different temporal combinations of LST data, including the ones from the subject day (two day-time and two night-time, like the present dissertation) and the corresponding "day-before" observations. The goal defined in their work was to estimate daily T_{min} and T_{max} for Seoul and Los Angeles. For that purpose, in addition to the afore-mentioned LST data, they also considered parameters of "solar radiation", NDVI, "elevation", "aspect", "latitude", "longitude", "percentage of impervious area" (p. 149). (Here, note that the impervious area percentage was derived from a land-cover dataset with a spatial resolution of 250m for 1km grid cells.) Through random forest, a machine learning technique, the study derived T_{min} and T_{max} with less than 1.7K RMSE and greater than 0.7 R^2 (Yoo et al. 2018).

Similar with the goals of the present dissertation, Irger (2014) explored microclimatic conditions in Sydney city of Australia with respect to the built environment attributes. This was carried out by means of a series of regression analyses, namely, "multiple linear regression" inquiries as well as introduction of a "spatial regression model" at later stages. Dependent variables for these inquiries were air temperatures in specified urban canyons, mean land surface temperatures at specified 100m x 100m "grids" as well as, again, in urban canyons. These variables were evaluated separately at regression inquiries, and each were investigated for both day-time and night-time conditions (Irger 2014).

As Irger (2014) describes, the study relied on the "airborne remote sensing" including lidar acquisitions, as well as vehicle transects (car) which were simultaneously carried out during the flights. This data acquisition by Irger (2014) was performed in early August 2012 (winter season in Australia), one "midnight" and one "noon" campaign. The study explored the attributes of the "urban form" by largely employing the "local climate zone" (LCZ) parameters by Stewart and Oke (2012), with some "modifications" and omissions (Irger 2014).

As presented in Table 6, the independent variables Irger (2014) examined for air temperature estimations consisted of variables representing the building-related characteristics as well as location-based and temporal parameters, and LSTs. By evaluating these variables based on "Pearson's correlation coefficients", "Variance Inflation Factors" (VIFs), and "Durbin-Watson" tests, amongst other spatial assessments, Irger (2014) concluded that the area covered by high vegetated surface cover, albedo values associated with the ground covered by impervious surfaces and sea-level were the three variables that made a significant influence on the day-time air temperature predictions for the specified urban canyons. For the night-time prediction of air temperatures, the variables Irger (2014) classified as "significant" included the aspect ratio of the canyons, distance of the investigated canyon to the coast and the sea-level (Irger 2014).

Note that, when the dependent variable was considered as the mean LSTs of the specified "grid" zones, Irger (2014) further looked into the built environment parameters such as surface fractions of building roofs (unless trees were blocking them), as well as other independent variables representing the three dimensionality of the study domain. These variables were "Height-to-Distance ratio" which is the proportion of mean building height to "the average distance between all buildings within a grid cell" (Irger 2014, p. 147); and "Volume-to-Area ratio" which refers to "the ratio of the total building volume to grid cell area" (Irger 2014, p. 147) (see also, "equivalent building height", Chapter 3) (Irger 2014).

This differentiation in the estimated parameters by Irger (2014) (i.e., T_{air} and LST) is to some extent related with the point emphasized by a recent study carried out in the Czech Republic by Středová et al. (2021). (Note that, this differentiation is also associated with the parameters employed by the present dissertation and further briefly discussed in relation with the research findings, in the conclusion chapter.)

According to Středová et al. (2021), existing literature tend to focus on either the air temperature behaviours among the LCZs or the LST characteristics. In that sense, Středová et al. (2021) argue that "a comprehensive method combining LCZs, LST and AT is still rare" (p. 2), by referring to a research effort exploring this interaction, Cai et al. (2018) (Středová et al. 2021). Here, AT denotes T_{air}, based on Středová et al. (2021), and the work by Irger (2014) mentioned above is also an example which "combines" LST, T_{air}, and LCZs (Irger 2014).

In the light of these points, Středová et al. (2021) and Cai et al. (2018) also provide valuable insights regarding the thermal behaviours in relation with the built environment and from the perspective of LST and T_{air} interactions (Cai et al. 2018; Středová et al. 2021).

Although this afore-mentioned argument by Středová et al. (2021) is focused on a more wider scale explorations of LCZs and their direct interactions with T_{air} and LST behaviours, it nevertheless implies a potential to further explorations carrying similar motivations, based on the built environment and urban climate perspective. This is further addressed in the next chapter of the present dissertation, in relation with the research design and methodology.

3. APPROACH

3.1. Framework of the study

This chapter presents the case area, employed methods and the conducted workflow in the present dissertation. This is carried out by dividing the performed work into four sections based on the research objectives as well as the contribution of these sections to the overall goals of the study.

As such, the present dissertation aims to define an approach for attaining near-surface air temperatures (T_{air}) with sufficient spatial detail that would allow its utilization in building science and urban canopy-layer inquiries (Firat Ors and Mahdavi 2021; Firat Ors et al. 2019).

The goal is to realize this objective in such a manner that the proposed approach would rely solely on "publicly-accessible" geo-spatial and thermal data to derive this information (i.e., T_{air}) (Firat Ors and Mahdavi 2021). The motivation behind this is to facilitate the applicability of the proposed approach to the situations (regions) that are deficient of terrestrial thermal observations. This further includes urban environments, which require an immensely "dense" spatial distribution of the meteorological equipment for obtaining "representative" readings of T_{air} at the micro-climatic scale (see, for instance, Crawley and Barnaby 2019; Mahdavi 2018; Mahdavi et al. 2013; Maleki et al. 2012; Lim et al. 2014; Vuckovic 2015; Vuckovic et al. 2017).

In this context, the workflow that the present dissertation carries out to accomplish these objectives (following Firat Ors and Mahdavi 2021; see also Firat Ors et al. 2019) can be described under four stages:

- Defining the case study area and within that area, selecting sub-areas to focus further investigations.

  This was accomplished by considering potential thermal data sources (both remotely-sensed and terrestrially-observed), as well as the environmental aspects (spatial characteristics, building-related features, green spaces) of the considered locations.

- Quantifying the building-related attributes of the specified areas to be able to objectively describe these locations, compare them with each other or with other locations.

  This was accomplished by exploring these settings – mainly – via the "Local Climate Zone" (LCZ) Classification System (Stewart 2011; Stewart and Oke 2012).

- Selecting, filtering, pre-processing and obtaining remotely-sensed thermal datasets; and exploring them with respect to the obtained T_{air}.

  This was carried out by comparing these data (i.e., remotely-sensed data and T_{air}) to illustrate how they responded to one another, and thus, providing an initial and objective basis for obtaining T_{air}.

- Exploring ways to derive T_{air} with an agreement better than the one acquired in the previous step (namely, its existing relationship with the remotely-sensed thermal data).

  This was accomplished by benefiting from the location-based attributes of the specified areas and by considering certain observational conditions (Benali et al. 2012; Irger 2014; Schneider dos Santos 2020; Shi et al. 2016; Yoo et al. 2018; Zakšek and Schroedter-Homscheidt 2009 amongst others).

In this context, this framework is illustrated in detail in the following parts of this chapter. The next chapter includes the outcomes from the presented approach. Before explaining these points in more detail, it is of importance to remark that the goals, approach, and the findings conveyed in the present dissertation are to a considerable extent adapted, or at certain parts, modified/ changed, from a previous collaborative work that is presented in Firat Ors and Mahdavi (2021). The goals and the approach of the present dissertation also show a significant alignment with another collaborative work that is presented in Firat Ors et al. (2019).

3.2. Selected and specified study areas

3.2.1. Case area

The specified case area for the present dissertation is presented in Figure 3. Note that the exact perimeter of this area is determined considering certain properties of the remotely-sensed land surface temperature (LST) data and the locations of the "terrestrial meteorological weather station"s ("WS"s) employed in this work. This is explained with further detail in the following parts of this chapter (Firat Ors and Mahdavi 2021).

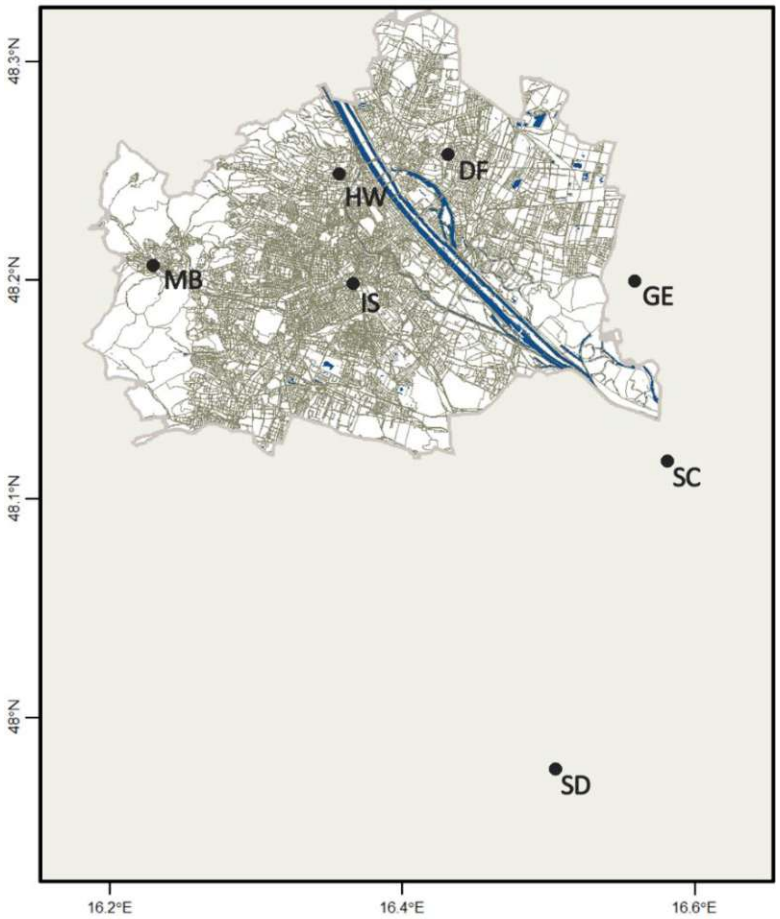

Figure 3. Case study area including the City of Vienna

Data source: OGD_Vienna (2021). Figure is illustrated using RStudio (RStudio Team 2018). Re-generated based on Firat Ors and Mahdavi (2021); partially based on Firat Ors et al. *(2019) and Vuckovic* et al. *(2017))*

As illustrated, the City of Vienna (Austria) is located within the defined case area. Vienna lies between 48° 07' 06'' - 48° 19' 23'' N and 16° 10' 58'' - 16° 34' 43'' E (City of Vienna 2021a), occupying 414.9 km^2 surface area (Bauer et al. 2020; City of Vienna 2021a; see also Firat Ors and Mahdavi 2021).

The city is closely situated to Austria's three neighbouring countries of Czechia (North), Slovakia (North-East) and Hungary (East) (see, for instance, Latitude 2021) and currently hosts around 1.91 million residents (Bauer et al. 2020; see also Firat Ors and Mahdavi 2021; Firat Ors et al. 2019).

Vienna has a notable topography. An Alpine "foothill" area, the Vienna Woods, lies at the West of Vienna (City of Vienna 2021b; Vienna Tourist Board 2021; see also Firat Ors and Mahdavi 2021). Danube River passes through the city and is a prominent element, like some other European cities such as Budapest (Hungary) or Bratislava (Slovakia), leading the dwellers to a frequent interaction with the "water" in the urban area via its channels (see, for instance, City of Vienna 2021c). Vienna also has a significant amount of vegetated surfaces, all of which makes up 45% of the City's total surface area (City of Vienna 2021d).

When we look at the climatic conditions experienced in Vienna, for the period between 1981 and 2010, the average monthly temperatures present a profile between 0.3 °C (January) and 20.8 °C (July) with the yearly average at 10.4 °C (City of Vienna 2021e; see also Firat Ors and Mahdavi 2021).

On the other hand, the "total" precipitation averaged for the same period (i.e., 1981-2010) is between 37.8 mm (October) and 72 mm (August) with the yearly total at 650.7 mm (City of Vienna 2021e; see also Firat Ors and Mahdavi 2021). According to the same data, the months from May to September stands out by being the most humid period of the year where the lowest total precipitation is noted for September at 60.8 mm (City of Vienna 2021e).

3.2.2. Selected weather stations and T_{air} data

3.2.2.1. Selected stations

The present work utilizes T_{air} data observed by seven WS (Firat Ors and Mahdavi 2021; Firat Ors et al. 2019). The locations of these WS are illustrated in Figure 3. Table 7 includes additional details regarding their positioning.

As presented in Table 7, the employed WS are positioned with varying distances from the city center of Vienna. Three of them, namely, SD (Seibersdorf), SC (Schwechat) and GE (Gross-Enzersdorf) are situated in the State of Lower Austria with distances from 1.5 km (GE) to 17 km (SD) to Vienna's borders. Other four, (MB (Mariabrunn), DF (Donaufeld), HW (Hohe Warte), IS (Innere Stadt)), are located in the city of Vienna (Firat Ors and Mahdavi 2021; Firat Ors et al. 2019).

Table 7. Further information on the selected weather stations (Partially based on ZAMG (2022b), modified from Firat Ors and Mahdavi (2021); Firat Ors et al. *(2019))*

WS	State	Distance to city center* (km)	Latitude, Longitude	Screening height (Ground / Altitude) (m)
Innere Stadt (IS)	Vienna	1.2	48.1984, 16.3664	9.3 / 177
Hohe Warte (HW)	Vienna	4.6	48.2486, 16.3564	1.9 / 198
Donaufeld (DF)	Vienna	6.9	48.2573, 16.4313	2 / 160
Mariabrunn (MB)	Vienna	10.7	48.2069, 16.2294	2.1 / 225
Gross-Enzersdorf (GE)	Lower Austria	13.8	48.1997, 16.5592	2.1 / 154
Schwechat (SC)	Lower Austria	18.5	48.1174, 16.5815	2.2 / 183
Seibersdorf (SD)	Lower Austria	27.6	47.9764, 16.5050	2.1 / 185

(*City center of Vienna, taken as 48.208, 16.372)

The WS DF, one of the seven WS that the T_{air} data is obtained from, is presented in Figure 4.

(a)

(b)

Figure 4. (a), (b) Weather station Donaufeld (DF) (photos by P. Fırat Örs, July 2019)

3.2.2.2. T_{air} data

ZAMG, Zentralanstalt für Meteorologie und Geodynamik (ZAMG 2022b) is the data provider of the employed T_{air} for the present dissertation (Firat Ors and Mahdavi 2021; Firat Ors et al. 2019).

Obtained T_{air} data was provided in one-hour increments (Firat Ors and Mahdavi 2021; Firat Ors et al. 2019). The dataset had been constructed by ZAMG (2022b) by taking the last-ten-minute average of the previous hour's observations and specifying that value as the temperature reading for the subject hour (personal communication of Josef Lechleitner (TU Wien) with ZAMG (2022b) on July 3rd, 2019).

For the present study, as an initial step, T_{air} data belonged to the period between 01.01.2000 – 01.09.2015 was attained from the afore-mentioned list of stations. This interval was specified considering the mutual availability of the terrestrial and remote-sensing measurements, which is explained with further detail in the following parts of this chapter (Firat Ors and Mahdavi 2021).

Furthermore, the selection of the seven WS presented in Table 7 was conducted considering available meteorological observations within the case area as well as environmental characteristics of the evaluated locations (Firat Ors and Mahdavi 2021). This is discussed in the next sub-section.

3.2.3. Specified study areas

3.2.3.1. Background

After selecting the weather stations whose T_{air} observations would be employed in this work, the next step was determining the spatial extent of the areas to be investigated around each. The aim was to define a perimeter within which the selected building-related attributes of the surrounding environment would be calculated and described.

Defining the extent of this perimeter is of significance because it encompasses the area whose characteristics potentially "influence" the T_{air} observations (i.e., "circle of influence"; see, for instance, Oke 2006; Stewart and Oke 2012). Note that, this is associated with the "scale" of the research problem, as discussed earlier (for instance, Mirzaei and Haghighat 2010; Oke 1984), here, T_{air} interactions with the surrounding environment.

This decision was guided by a considerable number of previous research works (see, for instance, Lelovics et al. 2014; Mahdavi et al. 2013; Skarbit et al. 2017; Stewart and Oke 2009; 2012).

Among these works, Mahdavi et al. (2013) introduce the term "Urban Units of Observation (U2O)". According to the authors, U2Os are "well-defined segments" (p. 4) within urban areas with similar built environment properties; and T_{air} observations from these areas are thus potentially insightful in illustrating the UHI "variation" inside an urban area (Mahdavi et al. 2013).

On the other hand, after Stewart (2011), Stewart and Oke (2012) define a series of classes termed the "Local Climate Zones (LCZs)". Such as U2Os, LCZs represent specific portions of (urbanized) settings with similar climatic tendencies. According to the principles presented by the authors, possessing certain combinations of environmental properties provides the basis for an investigated "setting" (i.e., "zone") to be classified into the relevant, corresponding LCZ class. Thus, this assignment is also associated with certain climatic tendencies of that location with respect to other types of LCZs with similar (climatic, topographic, geographic features etc.) backgrounds (Stewart and Oke 2012).

When we look at the spatial coverage of these areas, Mahdavi et al. (2013) consider "a spatial dimension (diameter) of approximately 400 to 1000 m" (p. 4) for the extent of the U2Os. Likewise, Stewart and Oke (2012) also suggest the same extent for the "minimum" dimensions of a LCZ setting.

In the light of these works and following previous studies such as Skarbit et al. (2017) and Stewart and Oke (2009); the areas to be examined in this dissertation are specified by determining a 500m diameter circle around each WS. The selected stations are readily positioned centrally within the specified areas (Firat Ors and Mahdavi 2021). Note that, for a consistent use of terminology within the present study, these specified areas are referred to as U2Os (Mahdavi et al. 2013) in this dissertation.

3.2.3.2. Overview of the specified areas

Based on the afore-mentioned considerations, seven U2Os are defined within the case area, around the WS illustrated in Figure 3. Figures 5 to 11 provide aerial views from these locations. Before quantitatively addressing these areas in the following parts of this chapter, a short description of each is provided for explanatory purposes and following Vuckovic (2015).

Figure 5. Specified U20 (black circle) and the IS WS (yellow point) (source: Orthofoto (2015), image exported from QGIS.org (2021))

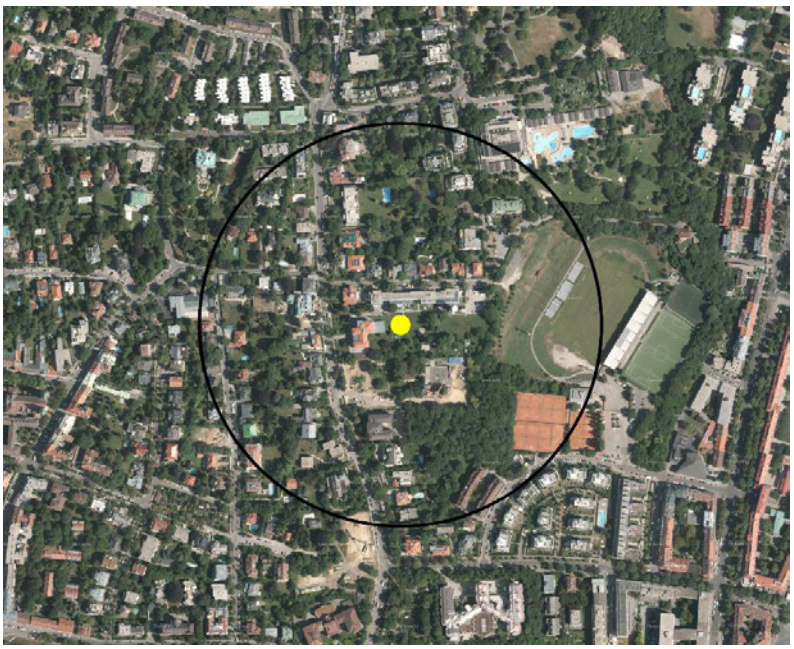

Figure 6. Specified U20 (black circle) and the HW WS (yellow point) (source: Orthofoto (2015), image exported from QGIS.org (2021))

Figure 7. Specified U20 (black circle) and the DF WS (yellow point) (source: Orthofoto (2015), image exported from QGIS.org (2021))

Figure 8. Specified U20 (black circle) and the MB WS (yellow point) (source: Orthofoto (2015), image exported from QGIS.org (2021))

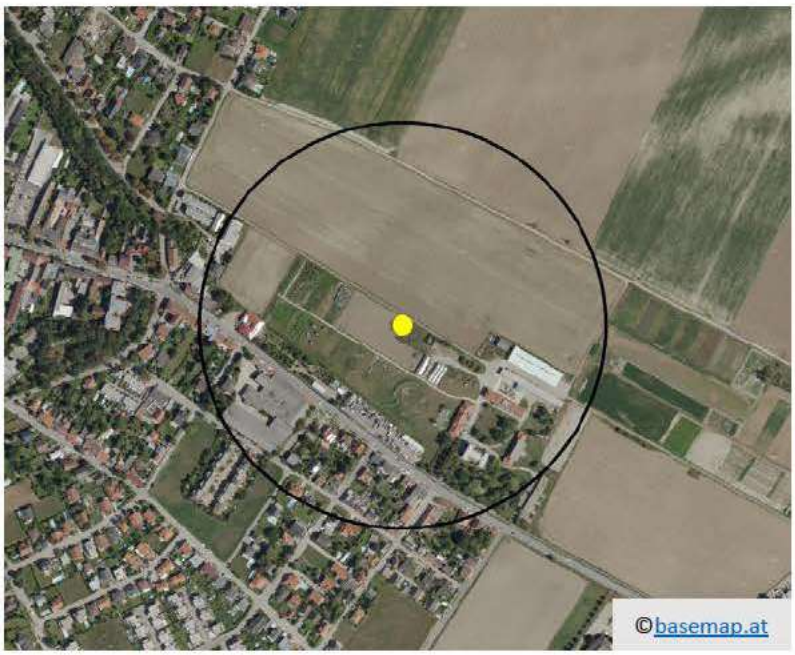

Figure 9. Specified U20 (black circle) and the GE WS (yellow point) (source: Geoland_Basemap Orthofoto (2021), image exported from QGIS.org (2021))

Figure 10. Specified U20 (black circle) and the SC WS (yellow point) (source: Geoland_Basemap Orthofoto (2021), image exported from QGIS.org (2021))

Figure 11. Specified U20 (black circle) and the SD WS (yellow point) (source: Geoland_Basemap Orthofoto (2021), image exported from QGIS.org (2021))

Innere Stadt (IS) U2O is the closest U2O to the city center of Vienna (taken as 48.208, 16.372) with a distance of – around – 1.2 km (Table 7). Likewise, it is the densest one in terms of the built environment characteristics. Courtyards are commonly found within the building blocks. The building types include educational facilities as well as residential buildings with street-level trade spaces (small shops, restaurants). Green surfaces are observed within the courtyards, as well as partially on the North-East edge of the specified U2O, where a public square is located (Figure 5).

Further information regarding the IS area (as well as for HW, DF and SD locations) is also provided by Vuckovic (2015) which can be also referred to, though it must be noted that the footprints of the U2Os defined by both works are not identical with each other.

Hohe Warte (HW) U2O largely consists of residential buildings, whereas buildings which belong to government institutions, and places of worship are also situated within the area. Vegetated surface cover is common. Transportation infrastructure is also clearly identifiable from the aerial images (Figure 6). The altitude generally increases when moving from South-East to North-West within the defined perimeter (see also Vuckovic 2015).

Donaufeld (DF) U2O mainly consists of residential and educational buildings; and includes the campus of Veterinärmedizinische Universität Wien (the University of Veterinary Medicine Vienna), where the DF WS is situated (Figure 4). The vegetated cover is denser on the North-West part of the defined area (see also Vuckovic 2015) (Figure 7).

Mariabrunn (MB) U2O consists of sparsely distributed buildings with residential, religious, research or trade functions. Green surfaces are common. Brick, concrete and metal roofs are found in the area. The transportation infrastructure includes a railway passing through the North edge of the defined perimeter. Aerial images also clearly depict the main roads (Figure 8).

Gross-Enzersdorf (GE) U2O is situated in an intersection of open fields and a residential setting with rural/suburban characteristics. Buildings with education, research or trade functions are also present in the area. (Figure 9).

Schwechat (SC) U2O is situated mainly in an airport area in the State of Lower Austria. The surface cover is largely pervious (Figure 10).

Seibersdorf (SD) U2O is the Southernmost study area in the present work (Figure 3). Such as the GE U2O, the SD area is also positioned in an intersection of open fields and a built-up space. The buildings within the defined zone mainly belong to several research institutions. Pervious surface cover is common (see also Vuckovic 2015) (Figure 11).

3.3. Building-related attributes of the specified areas

3.3.1. Background

After specifying the study areas around the selected stations, the next step was to quantitatively describe these locations to assist the following stages of the present work. As stated earlier, this was accomplished by investigating these areas utilizing mainly the "local climate zone (LCZ)" classification system (Stewart 2011; Stewart and Oke 2012; see also Firat Ors and Mahdavi 2021).

To summarize, according to Stewart and Oke (2012), LCZ classes are separated into two main groups referred to as "built types" and "land cover types" (p. 1885).

"Built types" consist of 10 different LCZ classes where each class represents a combination of different built environment features. These include "compact" (LCZs 1-3) or "open" (LCZs 4-6) classes which differ by their spatial organization and roughness characteristics (i.e., "high-rise", "midrise", "low-rise"). The dominant type of land cover also shows certain tendencies amongst them (i.e., pervious for open and impervious for compact types). Remaining built classes include "lightweight low-rise" and "large low-rise" classes (LCZs 7 and 8), "sparsely-built" (LCZ 9) and "heavy industry" (LCZ 10) (Stewart and Oke 2012, p. 1885).

On the other hand, the LCZs defined as "land cover types" consist of seven groups. These are "dense" or "scattered" trees (LCZs A, B), "bush, scrub" (LCZ C), "low plants" (LCZ D), "bare rock or paved" (LCZ E), "bare soil or sand" (LCZ F) and "water" (LCZ G) (Stewart and Oke 2012, p. 1885). Additionally, LCZ classification addresses temporal changes in the land cover as well by introducing "bare trees", "snow cover", "wet" or "dry" ground as "variable land cover categories" (Stewart and Oke 2012, p. 1885).

In this framework, Stewart and Oke (2012) suggests employing certain parameters to quantitatively assess subject areas and to classify them into LCZ classes. These are grouped under "geometric and surface cover properties" (seven parameters) and "thermal, radiative and metabolic properties" (three parameters) listed below (Stewart and Oke 2012, pp. 1886-1887):

- **Sky View Factor**
- Aspect Ratio
- **Building Surface Fraction**
- **Impervious Surface Fraction**
- **Pervious Surface Fraction**
- **Height of Roughness Elements [m]**
- Terrain Roughness Class

- Surface Admittance [J m^2 $s^{-1/2}$ K^{-1}]
- **Surface Albedo**
- Anthropogenic Heat Output [W m^{-2}]

3.3.2. Physical description of the specified areas

In this context, the specified seven U2Os in the present dissertation were explored regarding their environmental features by employing the "sky view factor", "height of roughness elements", "building surface fraction", "impervious surface fraction" and "pervious surface fraction" LCZ parameters from the above-mentioned list (Stewart and Oke 2012; see also Firat Ors and Mahdavi 2021).

Note that, in principle, these selected parameters are also present among the variables suggested by Mahdavi et al. (2013). Apart from these, one additional U2O variable, "equivalent building height" (Mahdavi et al. 2016; Vuckovic 2015), was also considered in this dissertation. This is explained in more detail in the following chapter in relation with the research findings.

Furthermore, for the specified study areas, the "surface albedo" parameter was also considered via the remote-sensing data of "Black-sky Albedo". This is explained further in later sections of this chapter (Mahdavi et al. 2013; 2016; Stewart and Oke 2012; Firat Ors and Mahdavi 2021).

In this context, the selected "geometric and surface-cover" attributes were calculated for each specified U2O in this study (Stewart and Oke 2012; Mahdavi et al. 2013). The idea behind this was to utilize the results of these calculations in the next steps of the present work where the microclimatic behaviours within these settings would be explored (Firat Ors and Mahdavi 2021). As stated earlier, calculating these parameters would also provide the objective basis to compare and evaluate the environmental characteristics of the selected U2Os (Stewart and Oke 2012). This would provide a more informed perspective when evaluating the outcomes of the present study.

3.3.2.1. Approach

In the light of these considerations, calculations of the afore-mentioned built environment parameters within the specified areas were carried out by employing Geographic Information System (GIS) tools and techniques.

According to USGS, GIS has a wide range of application areas including "resource management", "earth sciences" and "biology" (USGS 2022a). Selvam et al. (2019) provides a comprehensive overview regarding its basic principles. Many recent studies employed GIS techniques for similar purposes as with the present dissertation, to quantify and document building-related attributes within the investigated locations (for instance, Glawischnig et al. 2014; Hammerberg 2014; Lelovics et al. 2013; Skarbit et al. 2017; Vuckovic 2015; Zheng et al. 2018).

In this context, QGIS software (Version 3.8.0 Zanzibar) was mainly employed in the present study for the afore-mentioned purposes (QGIS.org 2021; Firat Ors and Mahdavi 2021). Microsoft_Excel (2022) also assisted at some points to further process the QGIS outputs.

It is of significance to note here that, at certain instances, the pursued workflow for these calculations was adapted based on the type of the attained geospatial data for the study areas. This mainly depended upon whether the investigated U2O was situated within the city of Vienna or not (Figure 3, Table 7).

3.3.2.2. Calculating the surface fractions

In principle, the whole surface area of an U2O is divided into three sub-areas according to the type of the surface cover: Areas covered with buildings, with pervious surfaces or with impervious surfaces (Mahdavi et al. 2013; Stewart and Oke 2012; see also Vuckovic 2015; Vuckovic et al. 2016). Their fractions within the U2Os were calculated based on the following relationships:

"Building Surface Fraction" (BSF) is calculated as the ratio of total plan area of buildings at ground-level ($\sum A_{building}$) to the whole surface area of U2O (A_{U2O}), as represented in Equation (3.1) (Stewart and Oke 2012; Mahdavi et al. 2013; see also Vuckovic 2015; Vuckovic et al. 2016):

$$BSF = \sum A_{Building} / A_{U2O} \qquad (Eq.\ 3.1.)$$

"Pervious Surface Fraction" (PSF) is calculated as the ratio of the total surface area with pervious surface cover – including bare soil, water, and vegetated surfaces – ($\sum A_{Pervious}$) to the whole surface area of the U2O (A_{U2O}), as represented in Equation (3.2) (Mahdavi et al. 2013; Stewart and Oke 2012; see also Vuckovic 2015; Vuckovic et al. 2016):

$$PSF = \sum A_{Pervious} / A_{U2O} \qquad (Eq.\ 3.2.)$$

"Impervious Surface Fraction" (ISF) is calculated as the ratio of the total surface area with impervious surface cover ($\sum A_{Impervious}$) to the whole surface area of the U2O (A_{U2O}) (Equation 3.3) (Mahdavi et al. 2013; Stewart and Oke 2012; see also Vuckovic 2015; Vuckovic et al. 2016):

$$ISF = \sum A_{Impervious} / A_{U2O} \qquad (Eq.\ 3.3.)$$

Equations 3.1. to 3.3. lead to (Mahdavi et al. 2013; Stewart and Oke 2012; see also Vuckovic 2015; Vuckovic et al. 2016):

$$BSF + PSF + ISF = 1 \qquad (Eq.\ 3.4.)$$

For the U2Os located within the City of Vienna (namely, IS, HW, DF and MB U2Os), the surface fraction calculations were carried out utilizing geospatial datasets in form of "vector" data. These data were obtained from the City of Vienna (City of Vienna 2021f; Firat Ors and Mahdavi 2021; Glawischnig et al. 2014; Hammerberg 2014; Vuckovic 2015; Vuckovic et al. 2016).

Since meteorological and remote sensing data employed in this study belongs to the period 2000-2015, obtained vector data does not represent the current conditions, but the built environment prior to 2015. Exception to this was the MB U2O, for which, historical geospatial data before 2015 was not readily available. For this location, a current dataset, namely, "Flächen-Mehrzweckkarte Vektordaten Wien" ("Area Multi-purpose Map Vector Data Vienna") was obtained from MA41_Geodata (2021) (MA41_Geodata 2021; OGD_Vienna 2021; OGD_Vienna FMZK 2021; Vienna_FMZK 2021). In this dataset, potential changes in the built environment were assessed with respect to the historical condition using the aerial imagery from 2015 (Orthofoto 2015), and the data was decided to be used as it was provided. Note that, within the scope of the present work, special attention was not given to the possible changes in the (built) environment within the defined time period of the study (i.e., from 2000 to 2015).

In this context, the obtained vector data for the Vienna locations include geo-spatial information that "attribute" each element within an U2O in various categories. These categories include the "Bodennutzungsklasse" (Land use class) of the elements (Glawischnig et al. 2014; Hammerberg 2014; Vienna_FMZK 2021; Vuckovic 2015; Vuckovic et al. 2016). This information is in decimal number format for which a "look-up" table is provided for interpretation (Vienna_FMZK 2021). This assisted in surface fraction calculations to identify pervious, impervious surfaces and surfaces covered by buildings. Based on these insights, the following workflow was carried out individually for each specified U2O within the city of Vienna.

The obtained vector file was first spatially clipped to include information only from the defined circular U2O area. After that, the geometry information of "area" and "perimeter" were added in QGIS to all spatial elements within the clipped area. This was achieved via the "Vector – Geometry Tools – Add Geometry Attributes" tool in QGIS.

Later, the clipped file was grouped into three separate layers depending on the land cover categories of its attributes. These layers were constructed so that, the U2O area was individually divided among "buildings" (ground-level), "impervious surfaces" and "pervious surfaces". This was accomplished by selecting the relevant attributes that belong to each surface fraction group and "exporting" the "selected features" to a new layer in QGIS. The afore-mentioned "look-up table" (Vienna_FMZK 2021) was consulted in the selection.

Next, the total plan area of each layer was derived by employing the "Vector – Analysis Tool – Basic Statistics for Fields" tool in QGIS (following Vuckovic 2015). From the outputs, fraction of each plan area (i.e., "building", "pervious", "impervious") with respect to "the total U2O plan area" was computed based on the Equations 3.1. to 3.3.

Figure 12 represents the vector data layers employed in the surface fraction calculations for the IS U2O.

Figure 12. Layers representing buildings (brown), impervious surfaces (grey), pervious surfaces (green). Yellow point represents the IS WS

(Data source: City of Vienna (2021f), image exported from QGIS.org (2021))

For the U2Os situated outside the city of Vienna's borders (namely, GE, SC, SD U2Os), it was first decided to construct a vector dataset for each of these areas due to the characteristics of the available geo-spatial data for these locations. For that purpose, aerial imagery and maps accessed mainly via QGIS were employed (Basemap_HIGHDPI 2021; Geoland_Basemap Orthofoto 2021; Google Earth 2022a; 2022b; 2022c; OpenStreetMap contributors 2021; Orthofoto 2014; 2015; see also Firat Ors and Mahdavi 2021). The exception to that was Google Earth (2022a; 2022b; 2022c) which was accessed via its web interface.

Recent changes in the built environment due to urbanization was addressed in the process. The goal was to determine as representative conditions as possible for the time period of the present study. For that purpose, for the GE U2O, Orthofoto (2015) and (2014) were utilized. Although these sources provide aerial imagery acquired in the years 2015 and 2014 for the City of Vienna respectively, they also contain information from the GE U2O thanks to the close proximity of the area to Vienna. For the SC and SD U2Os, this information was not available. Addressing the historical condition was not found to be necessary for the SC U2O, as it is largely situated in an open airport area. For the SD location, the aerial image provided by Vuckovic (2015) was consulted to screen for the more recent changes in the built environment (Google Maps© image as presented in Vuckovic 2015 Figure 22, p.37).

As with the Vienna locations, no extra attention was directed to track the potential urbanization activities within the specified time period of the present study (between the years 2000-2015).

In the light of these considerations, the data sources noted above were utilized; and vector layers corresponding to "building", "pervious" and "impervious" surfaces were constructed in QGIS for the three specified U2Os in the State of Lower Austria. The same workflow was pursued with the Vienna locations to calculate surface fractions based on these layers.

Note that, the presented approach employed for these three U2Os outside of Vienna was subject to a certain level of uncertainty. First, for some buildings, the ground-level plan area information was not found suitable (or was missing) and aerial images were used instead for defining the building areas. This led to using the roof area information as the building surface area for these buildings. At few instances, it was also not easy to

distinguish between bare soil and sealed surfaces from the aerial images. The way the surface fraction vector layers were constructed in QGIS via this workflow (by tracing) was also, precision-wise, prone to a certain level of error. All in all, it was decided that at the spatial level of an U2O, these uncertainties were not significant, and the approach yielded acceptable outcomes.

3.3.2.3. Height of the buildings

After calculating the surface fractions, the next step was to calculate the "height of roughness elements" within the U2Os (Stewart and Oke 2012). This was accomplished by calculating the "area-weighted mean building height" (MBH) of the specified locations (Abougendia et al. 2020; Firat Ors and Mahdavi 2021; Hammerberg et al. 2018; Lelovics et al. 2013; Wu et al. 2018; Unger et al. 2014; Zheng et al. 2018).

The calculations were carried out based on the Equation 3.5 presented below (Abougendia et al. 2020; Wu et al. 2018):

$$MBH = \frac{\sum_i^n (BHi * BAi)}{\sum_i^n BAi} \qquad \textit{(Eq. 3.5.)}$$

In Equation 3.5, BHi corresponds to the "height", BAi to the "footprint area" of the specific building and n is the total "number of buildings" within an U2O (Abougendia et al. 2020; Wu et al. 2018).

For the U2Os situated in Vienna, the previously described vector data contains the information necessary to derive building heights (on the level of eaves) (Vienna_FMZK 2021; Vuckovic 2015) except for the MB dataset. For MB, a new vector dataset, namely, "Baukörpermodell" (building model) was obtained from MA41_Geodata (2021) which included the necessary attributes (Vienna_Baukörpermodell 2021). This file was initially processed as described in the previous sub-section via spatial clipping and assigning the geometrical attributes of "area" and "perimeter" to all elements inside the U2O. After this pre-processing, the relevant elements were selected in QGIS individually for all specified U2Os in Vienna, and the geospatial data associated with them were exported in .csv format. From this data, the MBH calculations were performed employing Microsoft_Excel (2022) (Equation 3.5).

Note that, with this approach, the building heights were defined from the level of eaves (Vienna_FMZK 2021; Vuckovic 2015) and the building footprint areas were defined from the ground-level plan areas of the buildings.

For the remaining U2Os, the following workflow was pursued individually. Initially, a "digital terrain model" (DTM) and a "digital surface model" (DSM) were obtained in "raster" format with 10m spatial resolution from the "Open Government Data" database of the State of Lower Austria (Land Niederösterreich) (DTM_NOE 2020; DSM_NOE 2020; OGD_NOE 2020).

These raster files were spatially clipped in QGIS based on the U2O area. Afterwards, by utilizing "Raster Calculator", the DTM raster was subtracted from the DSM raster (hereafter, the "DSM-DTM raster"). This provided height information of the 3D elements within the study area. As the DSM-DTM raster was in 10 m spatial resolution, three-dimensional information from Google Earth (2022a; 2022c), a QGIS plug-in named AustrianElevation (AustrianElevation 2022), and height information provided by Geoland_map (2022) were also consulted. The following workflow was conducted to assign the building heights based on these data sources.

First, from the DSM-DTM raster, the "maximum" pixel value overlapping the building area was selected for each building. The idea behind this was to avoid mis-leading information, as the spatial resolution of the DSM-DTM raster was not ideal. If this value was not found plausible based on the consulted sources listed above, another pixel value overlapping the investigated building was used or a representative value (mainly from the centroids of the building footprints) was selected based on Geoland_map (2022) and AustrianElevation (2022). After the building heights were assigned, the same workflow pursued for the study areas in Vienna was followed to obtain the MBH values.

Note that, the SC U2O is situated largely in an open airport area and includes only a couple of structural elements which belong to the meteorological observation setting. Therefore, MBH calculation was not performed for this location. Also, for the SD U2O, a minor subset of buildings was not included to the MBH calculations due to data reliability concerns associated with the recent changes in the built environment.

It is of significance to note here that, the presented approach brings about a difference in the MBH outcomes representing the U2Os situated within and outside of Vienna's borders. As already mentioned, the obtained vector data for Vienna provides height information from the level of building eaves (Vienna_FMZK 2021; Vuckovic 2015) while with the presented approach, for the Lower Austria U2Os, the building heights were commonly assigned from the highest/higher parts of the buildings. Moreover, the LCZ parameter "height of roughness elements" refers to the "mean tree/plant height" in the absence of buildings (Stewart and Oke 2012). This was not considered in the present work as it was not found critical for the evaluated locations (was only relevant for the SC U2O) and for the purposes of this dissertation.

3.3.2.4. Sky view factor

For the U2Os situated in Vienna, a DSM raster with 0.5m spatial resolution was obtained from MA41_Geodata (2021) to be employed in the "sky view factor" (SVF) calculations (DSM_Vienna 2020). This DSM raster provides a complete 3D overview of the specified U2Os including trees (see, for instance, Glawischnig et al. 2014; Hammerberg 2014; Vuckovic 2015). The workflow presented below was followed individually for each specified U2O within the city of Vienna.

Following the recommendations of Glawischnig et al. (2014), as a first step, "a buffer zone" was specified around each U2O. This zone had a width of 50 – 100 meters depending on the geospatial data availability from the U2Os. As a next step, the DSM raster was spatially clipped to include only this circular "buffered" extent.

SVF calculations were performed for this clipped DSM in QGIS, utilizing the "Sky View Factor" tool of the embedded SAGA-GIS module (Conrad et al. 2015; QGIS.org 2021). Other studies employed SAGA-GIS for SVF calculations include Zheng et al. (2018), Estacio et al. (2019) and Bernard et al. (2018).

After obtaining the outputs, a "buffer" with a width of 1.5 meters was also specified around buildings. This is adapted from Glawischnig et al. (2014), to derive outputs without contamination from the building-pixels.

The building footprint areas and this 1.5-meter buffer zone around them was later subtracted from the whole U2O surface area and an "overlay layer" was constructed as a vector data in QGIS. SVF output from SAGA-GIS was averaged over this layer (which did not include the buildings and a 1.5m buffer zone around the buildings) to obtain the SVF result representing the investigated U2O. This was accomplished by employing the "Raster Analysis – Zonal Statistics" tool in QGIS.

Figure 13 illustrates the example SVF output from IS U2O (Conrad et al. 2015; QGIS.org 2021).

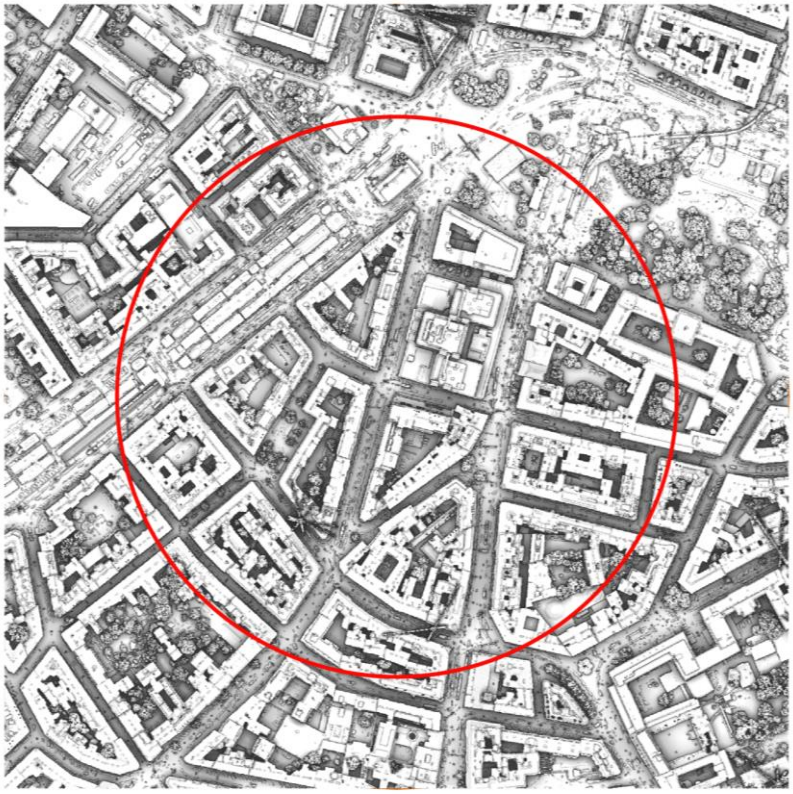

Figure 13. Example sky view factor output from SAGA_GIS module. Red circle indicates the boundaries of the IS U2O

(Data source: OGD_Vienna (2021), image exported from QGIS.org (2021))

For the remaining U2Os, the previously obtained DTM file (DTM_NOE 2020; OGD_NOE 2020) was also clipped to cover the U2O areas and the buffer zone specified around them. As stated earlier, this DTM was in 10m spatial resolution. After clipping, it was first resampled into a 1-m spatial resolution raster (hereafter, "1-m DTM raster") in QGIS via bilinear interpolation. For that purpose, the GRASS GIS tool "Raster – r.resamp.interp" was employed which was accessed through the "QGIS Desktop 3.8.0 with GRASS 7.6.1" software option (GRASS Development Team 2019; QGIS.org 2021).

In the next step, a vector layer was created for trees containing respective area and height information. For that purpose, the workflow and data sources described in the previous sub-sections were employed, where the building areas and heights had been assigned for the Lower Austria U2Os. Note that, this was mainly an approximation where a single height information from the top-level of their canopies was assigned to the tree batches as they were detected from the aerial images.

After that, the next step was to construct the raster files that would be used in SVF calculations. For that purpose, first, an initial "digital surface model" (DSM_B) was generated utilizing the 1-m DTM raster together with the "rasterized" building area and height data.

This was accomplished through the following steps. As a first step, the vector layer constructed for the MBH calculation was adjusted so that the building height information would be given with respect to the sea level, to match the way information is stored in the 1-m DTM raster. As a second step, this layer was converted to the raster format in QGIS, via "GDAL – Vector conversion – Rasterize (vector to raster)" tool (GDAL/OGR contributors 2022). In the last step, this raster was utilized together with the 1-m DTM raster to create the digital surface model, DSM_B, containing the terrain and building forms. This was achieved by employing the SAGA-GIS tool "Mosaic raster layers" in QGIS.

After obtaining the DSM_B, the vector layer representing the trees was also converted to raster format and a tree DSM was obtained as well. These two files were employed in the SVF calculations.

For the SVF calculations of the Lower Austria locations, the UMEP plug-in by Lindberg et al. (2018) was employed in QGIS since, unlike SAGA-GIS, it allowed the tree layer to be defined separately. After a brief assessment (not included here), this approach was found to be more suitable with the available type of data in these U2Os. To compensate for the lack of detail in the tree canopy representation with respect to the Vienna locations, 40% light transmissivity was defined for the tree DSM at UMEP. This threshold was selected based on the observations of Canton et al. (1994), which determined a range between 9% (summer) – 71% (winter) transmissivity amongst a variety of tree types (Canton et al. 1994, as presented in Konarska et al. 2014). The mean value of this interval (i.e., 40%) was applied in the present work.

After the SVF outputs were obtained, the SVF value representing the U2Os were derived via the same workflow as with the Vienna locations.

3.3.2.5. Equivalent building height

The spatial characteristics of the built spaces within the specified U2Os were further explored by calculating the "equivalent building height" (EBH) of these areas (Mahdavi et al. 2016; Vuckovic 2015; Vuckovic et al. 2016). According to Mahdavi et al. (2016), EBH refers to " the ratio of built volume (above terrain) to total ground area" (p. 86). Therefore, it does not only provide information regarding the mean height or total area of the built structures within the investigated areas but provides a more holistic perspective regarding their spatial characteristics. Note that, as mentioned earlier, this metric was also employed (with another terminology) by Irger (2014) in land surface temperature prediction efforts.

In this context, the EBH calculations were performed via the Equation 3.6. below (see also Vuckovic 2015):

$$EBH = \frac{\sum_i^n (BHi * BAi)}{A_{U2O}} \qquad \textit{(Eq. 3.6.)}$$

The same information that was used to calculate "area-weighted mean building height" was utilized in EBH calculations for the specified U2Os.

3.3.2.6. Assessment

As mentioned earlier, the building-related attributes calculated for the specified U2Os were later utilized to explore strategies to facilitate and improve the T_{air} estimations at these settings. This is discussed in the following parts of this chapter.

Moreover, a comparison of these calculation outputs with the previous work of Vuckovic (2015) is also provided in the next chapter for evaluation purposes.

This comparison was conducted to offer only a brief perspective, acknowledging that the footprints of the U2Os defined by both works show dissimilarities, and only four out of seven U2Os specified in this dissertation are situated around the same WS with the work of Vuckovic (2015). Furthermore, the approaches employed to calculate the parameters also show considerable differences between both works and all calculated parameters are not mutually present in both. A comparison between the outputs is presented in the next chapter acknowledging these points.

3.4. Microclimatic assessments

3.4.1. Overview

After obtaining the T_{air} data and evaluating the environmental characteristics of the specified U2Os, the next step was exploring the microclimatic behaviours within these settings. This was carried out by investigating the obtained T_{air} data in relation to the remote sensing (RS) land surface temperature (LST) data acquired over the WS locations (Firat Ors and Mahdavi 2021; Firat Ors et al. 2019).

The (initial) motivation behind this effort was to attain a general perspective concerning how LST and T_{air} data behaved under different circumstances and regarding the changes in one another. This was evaluated on both spatial and temporal (more specifically, diurnal) levels (Firat Ors and Mahdavi 2021). The idea was to establish a basis towards acquiring T_{air} and for that purpose, to illustrate the existing relationship of LST and T_{air} at the selected locations (Firat Ors and Mahdavi 2021; Firat Ors et al. 2019).

3.4.2. Remote sensing data: LST

LST data which belong to Terra and Aqua MODIS acquisitions over the case area was employed in the present study (Aqua 2022; MODIS 2022a; Terra 2022; see also Firat Ors and Mahdavi 2021). Employed data consist of two LST products provided by "Land Processes Distributed Active Archive Center" (LP DAAC) (LP DAAC 2022). LP DAAC is structured under "NASA's Earth Observing System Data and Information System" (EOSDIS). It is a joint effort by the "National Aeronautics and Space Administration" (NASA) and "U.S. Geological Survey" (USGS) (LP DAAC 2022; NASA 2022; NASA_EOSDIS 2022; USGS 2022b).

The utilized LST products are the MOD11A1 (LST_{TERRA}) data of Terra MODIS and the MYD11A1 (LST_{AQUA}) data of Aqua MODIS satellite sensors. Version-6 datasets were utilized for both products (Wan et al. 2015a; 2015b; see also Firat Ors and Mahdavi 2021), as they were the most recent ones available at the time of data processing.

The LST_{TERRA} and LST_{AQUA} datasets offer day-time ($LST_{TERRA\text{-}DAY}$, $LST_{AQUA\text{-}DAY}$) and night-time ($LST_{TERRA\text{-}NIGHT}$, $LST_{AQUA\text{-}NIGHT}$) observations, which were all obtained for the present work (Wan et al. 2015a; 2015b; see also Firat Ors and Mahdavi 2021). These datasets consist of 1km (precisely 0.928km) pixels (i.e., "grids") (Wan 2013; see also Firat Ors and Mahdavi 2021); and were accessed, filtered, pre-processed, and obtained employing Google Earth Engine (GEE) (GEE 2022; GEE_Aqua 2022; GEE_Catalog 2022; GEE_Terra 2022; Gorelick et al. 2017; see also Firat Ors and Mahdavi 2021). These steps are explained in the following parts of this section.

In this context, Table 8 below provides a brief overview of the employed LST products. Further characteristics regarding the M*D11 products were presented earlier in Chapter 2.

Table 8. LST Datasets employed in the present study (modified from Firat Ors and Mahdavi (2021), partially based on MOD11A1_Data (2022); MYD11A1_Data (2022))

Product, Version	Product name	Abbreviation
MOD11A1, v006	MODIS/ Terra Land Surface Temperature/ Emissivity Daily L3 Global 1 km SIN Grid	$LST_{TERRA\text{-}DAY}$
		$LST_{TERRA\text{-}NIGHT}$
MYD11A1, v006	MODIS/ Aqua Land Surface Temperature/ Emissivity Daily L3 Global 1 km SIN Grid	$LST_{AQUA\text{-}DAY}$
		$LST_{AQUA\text{-}NIGHT}$

3.4.2.1. Filtering and pre-processing of the LST data

The pre-processing and filtering steps explained in this sub-section were applied individually to the $LST_{TERRA\text{-}DAY}$, $LST_{AQUA\text{-}DAY}$, $LST_{TERRA\text{-}NIGHT}$ and $LST_{AQUA\text{-}NIGHT}$ datasets, utilizing GEE (Firat Ors and Mahdavi 2021).

The workflow conducted in GEE is as follows. The LST datasets were filtered gradually a couple of times before obtaining the data which would be employed in further inquiries of the present work. A certain level of pre-processing was also performed on the data before exporting it. The purpose behind this was to derive the actual observational information delivered by the bands; and thus, to be able to perform filtering based on that information. These steps are explained in detail below.

Note that, here and in the following text, "bands" refer to the "Scientific Data Sets" (SDS) of the products, following the way they are referred to in GEE (2022) and GEE_Catalog (2022) (MOD11A1_Data 2022; MYD11A1_Data 2022; Wan 2013).

In this context, in the first step, the LST data was filtered regarding the acquisition dates of the images. The time frame utilized for that purpose was determined concerning the limits of available satellite-based and ground-based thermal data (Firat Ors and Mahdavi 2021). This time frame as well as further details regarding the LST datasets as they can be reached from the "Earth Engine Data Catalog" are presented in Table 9 (GEE_Aqua 2022; GEE_Catalog 2022; GEE_Terra 2022).

Table 9. LST datasets as stored in Earth Engine Data Catalog (modified from Firat Ors and Mahdavi (2021), partially based on GEE_Catalog (2022))

Abbreviation	Employed period	Earth Engine Data Catalog Dataset
LST_{TERRA}	05.03.2000 – 01.09.2015	MOD11A1.006 Terra Land Surface Temperature and Emissivity Daily Global 1km
LST_{AQUA}	04.07.2002 – 01.09.2015	MYD11A1.006 Aqua Land Surface Temperature and Emissivity Daily Global 1km

After specifying the temporal limits of the LST data to be called in, the next step was defining the spatial limits of the case area to perform filtering. This decision was of significance because this area would be later utilized in sky condition assessments to employ data with a good observational quality (Firat Ors and Mahdavi 2021).

In this context, first, a "region of interest" (ROI) was selected. In GEE, the case area illustrated in Figure 3 was specified as a rectangular area that covers the selected WS as well as the City of Vienna. The borders of this area were defined so that it would encompass at least a 5km distance (or 5-to-6-pixel footprints of the LST data) from the seven WS. The idea behind this was to obtain a sufficient spatial extent to carry out the sky condition assessments (Firat Ors and Mahdavi 2021). Based on these considerations, a rectangular area covering from 16.15325 E, 47.925 N to 16.654 E, 48.325 N was selected and specified in GEE (Figure 3). Note that, a similar approach was followed by Gawuc and Struzewska (2016), where they included a 10-km band around Warsaw and used it as a base for cloud screening and data filtering, amongst other analyses purposes. In GEE, the temporally filtered LST datasets (Table 9) were spatially filtered based on the specified case area (Firat Ors and Mahdavi 2021). For that purpose, the LST images were clipped with respect to this area and organized in a new "image collection" to be utilized in further pre-processing and filtering steps.

In the third step, this "new" collection was first filtered for cloud conditions, more specifically, for the amount of "valid" LST pixels inside the specified area. This decision stemmed from the data characteristics of the employed LST products. As stated by MOD11A1_Data (2022) and MYD11A1_Data (2022), amongst others, the employed LST data had been through a cloud screening process before it was made available for public use. As a result of this screening, some pixels had been extracted from the products due to a certain level of influence from the clouds (MOD11A1_Data 2022; MYD11A1_Data 2022; Wan 2013). Keeping in mind that, cloudy sky conditions might not be the only basis for a certain pixel not to have a "valid" observation, high amount of valid LST pixels over an area nevertheless implies a strong potential for clear-sky observational conditions. This presumably leads to more representative observations of the actual surface conditions, as risk of un-detected contamination from clouds decreases even further than it may be potentially inherent in the products (see, for instance, Wan 2013).

Based on these considerations, the third stage of filtering was conducted in GEE; and only the LST images with 90% and more pixels over the specified case area were included in further analysis stages (Firat Ors and Mahdavi 2021). Note that, this is parallel with the recommendations of Hu et al. (2014), as the authors recommend eliminating images with less than 90% pixels over the investigated areas for cloud screening purposes (Hu et al. 2014). On the other hand, Gawuc and Struzewska (2016) eliminates the ones with less than 60%.

To summarize, after these steps, the LST data which were acquired between the afore-mentioned dates (Table 9), and which have at least 90% LST pixels over the case area remained for further pre-processing and filtering. Number of available images at each LST dataset after these stages is presented in Table 10.

Table 10. Number of available LST images after temporal filtering and cloud screening processes

	Number of available images			
	$LST_{TERRA-DAY}$	**$LST_{AQUA-DAY}$**	**$LST_{TERRA-NIGHT}$**	**$LST_{AQUA-NIGHT}$**
After temporal filtering	5609	4797	5609	4797
After cloud screening	1222	962	1025	928

Before proceeding with other data filtering steps, certain calculations were performed in the image bands. This was carried out to account for the "scale factor", and in some instances, "additional offset" values that are inherent in the information conveyed by the bands; and to obtain the actual observational information (MOD11A1_Data 2022; MYD11A1_Data 2022). This pre-processing was performed in GEE for bands including information on "view angle", "view time" and "land surface temperature". In GEE, new bands were created for the LST images and outputs from these calculations were stored in these bands. These bands (except for the one where "view time" calculations were stored) later assisted in further filtering efforts. From this point, the following workflow was carried out individually for each of the seven WS locations (instead of the whole case area); and only by considering the pixel (i.e., "grid") at the investigated WS location (Firat Ors and Mahdavi 2021).

In this context, first, a data filtering was conducted to eliminate LST images if they do not have an observation (i.e., "valid pixel") over the investigated WS. This was based on the overall goal of the study, where LST data would be employed in acquiring T_{air}.

Second, from the remaining data, LST observations that have less than -35° or more than 35° "view zenith angles" were eliminated. This was decided based on the works by Monaghan et al. (2014) and Hu et al. (2014) (Firat Ors and Mahdavi 2021). To summarize, the idea behind this decision was to prevent unrepresentative LST observations (mostly due to the effects of "anisotropy"), as MODIS sensors have the capability to provide observations within -/+65° "view (zenith) angles" (Hu et al. 2014; Monaghan et al. 2014; see also MODIS_SDST 1997; Wolfe et al. 1998).

Third, LST observations "flagged" with a certain error range were removed from the datasets. This information is given for each pixel with the "quality indicator" bands, and for the present study, tolerated errors for the pixel at the investigated WS location were decided to be limited at 2K "average LST error" and 0.02 "average emissivity error" (Wan 2013; see also Firat Ors and Mahdavi 2021).

In order to eliminate data with a greater error range than specified above, it was first necessary to know which quality criteria was conveyed by the "bit-encoded" "quality indicator" bands (MOD11A1_Data 2022; MYD11A1_Data 2022; see also Firat Ors and Mahdavi 2021). As suggested by MOD11A1_Data (2022) and MYD11A1_Data (2022), this was accomplished by attaining a subset of the LST data from AppEEARS (AppEEARS Team 2020a; Wan et al. 2015a; 2015b) which provided the necessary, "decoded" explanations (MOD11A1_Data 2022; MYD11A1_Data 2022; see also Firat Ors and Mahdavi 2021). The filtering was then performed employing GEE, by considering the detailed information given by AppEEARS (Firat Ors and Mahdavi 2021).

After this final step, the filtered LST datasets were exported to Google Drive as .csv files. More specifically, the exported data was the values of the single pixels that correspond to the investigated WS location, for all available bands and for four afore-mentioned LST datasets. This process was repeated for each of the seven WS locations (Firat Ors and Mahdavi 2021). Table 11 provides the number of observations remained at each LST dataset after these efforts.

Table 11. Number of available LST observations after data filtering

WS Locations	$LST_{TERRA-DAY}$	$LST_{AQUA-DAY}$	$LST_{TERRA-NIGHT}$	$LST_{AQUA-NIGHT}$
IS	478	363	291	229
HW	567	410	343	278
DF	603	443	354	305
MB	615	489	449	404
GE	601	485	455	404
SC	632	498	460	391
SD	640	484	455	409
All locations	4136	3172	2807	2420

3.4.2.2. Assessment

In order to test the presented filtering and pre-processing steps, several subsets of the LST datasets were additionally acquired from AppEEARS (AppEEARS Team 2020a; 2020b; Wan et al. 2015a; 2015b). AppEEARS stands for "Application for Extracting and Exploring Analysis Ready Samples" and is an LP DAAC data platform (AppEEARS 2022; LP DAAC 2022). The acquired LST data was, again, the information conveyed by the pixels covering the WS location(s). It was provided in .csv format and as already processed. These data were attained so that they would provide information from all seven selected WS points for the period between 01.01.2014 – 01.09.2015. Furthermore, from one WS point (i.e., SC), the attained data included LST information from the whole investigated time period of the study. These data subsets were acquired for both LST_{TERRA} and LST_{AQUA} data (AppEEARS Team 2020a; 2020b; Wan et al. 2015a; 2015b). The workflow below was carried out to compare this data with the data acquired from GEE, and thus, to evaluate the pursued data filtering workflow.

First, the data attained from AppEEARS was manually filtered in Microsoft_Excel (2022) to (content-wise) match the observations that remained after the cloud screening step was completed in GEE (Table 10). This provided a baseline for assessing the data filtering steps conducted in GEE for the WS locations. Second, the remaining data was once more filtered based on the criteria presented in the previous sub-section (i.e., view angle, LST data availability, quality thresholds). The observations remained after this stage were compared with the exported data from GEE to evaluate the pursued workflow.

3.4.3. Data matching

3.4.3.1. View time of the LST data

After exporting the LST data from GEE, first, the datasets were processed so that the view time of the satellite-based data would match the way WS measurements were recorded. This conversion was done to provide the comparability of both datasets.

Employed LST products are provided in "local solar time" (Wan 2013). From the exported .csv files, the pixel values of the "view time" band were therefore converted to the "Central European Time" (CET), which, T_{air} data was recorded at. This conversion was carried out based on the guidelines described by Wan (2013).

Equation 3.7. was employed in the process (Grant 2017; based on Wan 2013):

$$t_{OBS\_UTC} = t_{OBS\_LS} - (long_{GRID} / 15) \quad [h] \quad (Eq.\ 3.7.)$$

In Equation (3.7), t_{OBS_UTC} is the UTC, and t_{OBS_LS} is the Local Solar Time of the observation for the investigated LST pixel (i.e., "grid"). t_{OBS_LS} values were obtained with the pre-processing steps described earlier, by scaling the "view time" band via the corresponding "scale factor" of 0.1 (Wan 2013; see also Grant 2017).

In Equation (3.7), the term $long_{GRID}$ corresponds to the "grid's longitude in degrees" (Wan 2013, p. 17). Here, "grid" is the LST pixel; and its longitude was calculated from its "centroid" following Grant (2017) (Grant (2017) (p.39) refers to a personal communication with Wan).

After obtaining the UTC time of the LST observations, conversion to CET time was simply performed by adding 1 hour (see, for instance, TIME_IS (2021)). "Daylight saving time" was not considered due to the way T_{air} was recorded (personal communication of Josef Lechleitner (TU Wien) with ZAMG (2022b) on July 3rd, 2019).

3.4.3.2. Data matching: T_{air} and LST

In order to explore the T_{air} data with respect to the obtained LST, these ground-based and satellite-based observations were initially "matched" with each other based on the times and locations they were observed (Firat Ors and Mahdavi 2021).

For that purpose, T_{air} data was interpolated based on the following relationship:

$$Q_x = Q_t + (x/60) \cdot (Q_{t+1} - Q_t) \qquad [°C] \qquad (Eq.\ 3.8.)$$

In Equation (3.8), t and t+1 are two consecutive hours within which the LST observation time is listed. Q_t and Q_{t+1} refer to the T_{air} data recorded at hours t and t+1, respectively. The term x refers to the minute of LST observation, and Q_x is the assigned ("matched") T_{air} value for the (corresponding) LST observation.

Based on these principles, data assignment between T_{air} data and LST datasets was carried out.

It is of significance to note here that, there were some unsystematic gaps present in the T_{air} data. Because of these gaps, the hourly data (Q_t and Q_{t+1}) that would have been employed in the interpolation was missing for some of the LST observations. When this occurred, two approaches were followed:

- If only one T_{air} measurement was missing between Q_t and Q_{t+1} pairs, the present one was assigned to the LST data without interpolation (as Q_x). This was applicable for a total of 9 observations.
- If both T_{air} observations of Q_t and Q_{t+1} were missing, corresponding LST observation was removed from the LST dataset and not included in the study.

After this elimination, total number of available LST data (pixel values at WS points from $LST_{TERRA\text{-}DAY}$, $LST_{AQUA\text{-}DAY}$, $LST_{TERRA\text{-}NIGHT}$, $LST_{AQUA\text{-}NIGHT}$) decreased from 12535 to 12454 (Firat Ors and Mahdavi 2021).

In this context, Table 12 includes further information regarding the LST datasets after this data matching effort, whereas Table 13 presents the observation times of these data over the case area. Their monthly distribution is further illustrated in Figure 14.

Table 12. Number of available LST observations after data matching

WS Locations	$LST_{TERRA\text{-}DAY}$	$LST_{AQUA\text{-}DAY}$	$LST_{TERRA\text{-}NIGHT}$	$LST_{AQUA\text{-}NIGHT}$
IS	478	363	291	229
HW	567	410	343	278
DF	599	442	350	302
MB	615	489	449	403
GE	601	485	455	404
SC	625	492	457	386
SD	619	470	452	400
Total, All locations	4104	3151	2797	2402

Table 13. CET Time of Observation of LST datasets over the case area (modified from Firat Ors and Mahdavi 2021)

Dataset	Observation time (min)	Observation time (max)
$LST_{TERRA\text{-}DAY}$	~ 10:30	~ 11:30
$LST_{AQUA\text{-}DAY}$	~ 12:30	~ 13:30
$LST_{TERRA\text{-}NIGHT}$	~ 21:30	~ 22:30
$LST_{AQUA\text{-}NIGHT}$	~ 01:30	~ 02:30

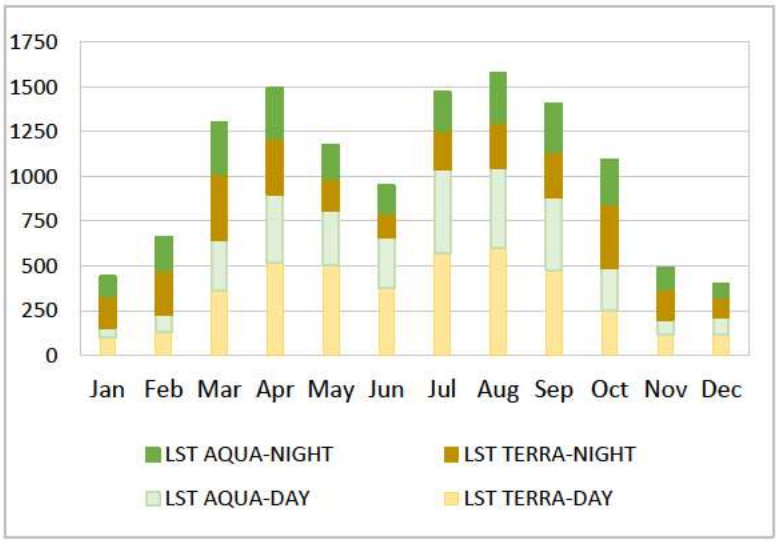

Figure 14. Monthly distribution of LST observations employed in this part of the study

3.4.4. Microclimatic assessments: T_{air} and LST relationship

3.4.4.1. Investigating T_{air} and LST

After the data matching between terrestrial T_{air} and satellite-based LST data were completed, these datasets were investigated with respect to each other at the selected WS locations. This inquiry was carried out gradually via linear regression, employing Microsoft_Excel (2022) and Analysis_Toolpak (2022).

Alexopoulos (2010) provides a detailed review on linear regression method and defines the approach as follows: The method devises a "linear equation" by estimating the associated "coefficients" that the numerical "dependent variable" can be predicted by with the closest fit through the equation. The equation employs "independent variables" that are either single or multiple (Alexopoulos 2010). According to the author, in regression, "to predict Y on the basis of X or to describe how Y depends on X (regression line or curve)" (p. 24) is the main goal (Alexopoulos 2010).

In cases where only one parameter is considered as the "independent variable" and one as the "dependent variable", like described in the workflow below, the analysis is referred to as "simple linear regression" (Alexopoulos 2010; Fávero and Belfiore 2019; Holmes et al. 2017; PennState 2018a).

This approach was employed in this stage of the present dissertation to illustrate and quantify how LST datasets relate to the observed T_{air} within the case area (Firat Ors and Mahdavi 2021; see also Firat Ors et al. 2019). In these inquiries, the dependent variable was T_{air} with LST as the independent variable.

In the described workflow below, the agreement between T_{air} and LST was explored through two metrics: R^2 – namely – the Coefficient of Determination, and RMSE, Root-Mean-Squared-Error. Note that these metrics were also employed by Vuckovic (2015) to assess the performance of a "predictive model".

The "best-fitting lines" of the investigated datasets and their scatter-plots were further employed to better evaluate the above-mentioned outcomes and to allow for initial T_{air} estimations over the case area (Firat Ors and Mahdavi 2021; Firat Ors et al. 2019).

In this context, Equation 3.9. describes the "best-fitting line" of the "simple linear regression", which was utilized in this part of the present dissertation (Alexopoulos 2010; Fávero and Belfiore 2019; Holmes et al. 2017; PennState 2018b):

$$y = b_0 + b_1 x \qquad \textit{(Eq. 3.9.)}$$

In Equation (3.9), b_0 refers to the "y-intercept" and b_1 to the "slope".

Likewise, the Equation 3.10. below gives the "predicted value" for the dependent variable (i.e., $\hat{y}_i$) from a single point belonging to the independent variable, which is x_i (Alexopoulos 2010; Fávero and Belfiore 2019; Holmes et al. 2017; PennState 2018b).

$$\hat{y}_i = b_0 + b_1 x_i \qquad \textit{(Eq. 3.10.)}$$

In this context, the Root-Mean-Squared-Error (RMSE) – or the "standard deviation of residual" – implies how scattered the data is with respect to the best-fitting line (Alexopoulos 2010; PennState 2018c). It is calculated via the Equation (3.11) below (Alexopoulos 2010; PennState 2018c).

$$RMSE = \sqrt{\frac{\sum(y_i - \hat{y}_i)^2}{DF}} \qquad \textit{(Eq. 3.11.)}$$

In Equation (3.11), $(y_i - \hat{y}_i)$ is termed as the "residual", showing the difference between the actual and "predicted" data points of the "dependent variable" (Alexopoulos 2010; Fávero and Belfiore 2019; Holmes et al. 2017; PennState 2018c).

The term DF refers to the "degrees of freedom" for residual inquiries. It is taken as "n-2" for the Simple Linear Regression, where n corresponds to the number of data points (Alexopoulos 2010; PennState 2018c).

On the other hand, the second metric employed in the present dissertation, i.e., R^2 (the Coefficient of Determination) is calculated via Equation (3.12) below (Fávero and Belfiore 2019).

$$R^2 = \frac{\sum_{i=1}^{n}(\hat{y}_i - \bar{y})^2}{\sum_{i=1}^{n}(\hat{y}_i - \bar{y})^2 + \sum_{i=1}^{n}(y_i - \hat{y}_i)^2} \qquad \textit{(Eq. 3.12.)}$$

where, $\bar{y}$ refers to the "average" of the dependent variable y (Fávero and Belfiore 2019).

R^2 values can be within the range of 0 to 1, where greater values indicate a better agreement of the investigated datasets (Fávero and Belfiore 2019; PennState 2018d; see also Firat Ors et al. 2019; Vuckovic 2015).

In the light of these points, the following steps were pursued to explore the agreement between T_{air} and LST data within the case area (Firat Ors and Mahdavi 2021):

- First, LST data from day-time acquisitions (a total of 7255 data points from $LST_{TERRA\text{-}DAY}$ and $LST_{AQUA\text{-}DAY}$) and night-time acquisitions (5199 data points from $LST_{TERRA\text{-}NIGHT}$ and $LST_{AQUA\text{-}NIGHT}$) were compared individually with the related T_{air} data.

- Next, LST data was organized under four groups depending on the products and acquisition times (namely, $LST_{TERRA\text{-}DAY}$, $LST_{AQUA\text{-}DAY}$, $LST_{TERRA\text{-}NIGHT}$, $LST_{AQUA\text{-}NIGHT}$) which were compared with the related T_{air} data.

- In the final step, four groups stated above were further divided into sub-groups based on their acquisitions over seven stations and compared with the T_{air} data.

Results from these stages are presented in the next chapter, where they are evaluated regarding the temporal and spatial considerations discussed earlier.

3.4.4.2. Investigating T_{air} and LST: Temporal considerations

Up to this point, investigations of T_{air} and LST datasets were performed based on the data filtering and matching constraints presented earlier. In order to further investigate the spatio-temporal tendencies of both data types, additional filtering criteria were introduced to the datasets. Note that, this stage of data elimination was only employed in this part of the study (i.e., this sub-section) and does not affect the following parts of the presented approach.

As mentioned earlier, four groups had been formed from LST-T_{air} "pairs" based on the four LST datasets ($LST_{TERRA\text{-}DAY}$, $LST_{AQUA\text{-}DAY}$, $LST_{TERRA\text{-}NIGHT}$, $LST_{AQUA\text{-}NIGHT}$). The following workflow was applied to each of these groups separately.

First, a data subset was formed so that, the LST-T_{air} "pairs" of a certain date remained in the subset only if there were valid LST observations at each of the seven WS points for that specific date. The goal was to explore T_{air} and LST relationship with a more direct focus on the investigated locations by limiting, to the extent possible, potential influencing factors such as seasonal and weather conditions.

Next, this remaining data were sorted based on the LST acquisition times over the rural WS. The idea behind this was to inquire how the behaviours of LST and T_{air} data differed between rural and more urbanized locations. For that purpose, SD WS was specified as the rural station (following Vuckovic 2015; Vuckovic et al. 2016).

After organizing the data based on the viewing time over the SD station, these data were further divided into two sub-sections, so that a maximum of 30-minute difference would remain among the observation times over the SD WS (Table 13). The goal was once more to limit potential affects that may arise from viewing time differences and to obtain a more homogeneous dataset for this round of spatial assessments. Note that, among the WS points, there was a maximum of 6-minute difference in the viewing times of the same date observations.

After these data were organized, they were assessed by means of box-plots to allow for a sufficient comparison amongst investigated locations. Findings from these inquiries are presented in the next chapter. Also, Table 14 presents additional details regarding the employed data in these assessments and the associated viewing time intervals over the SD WS.

Table 14. Details regarding LST datasets employed in the spatio-temporal assessments over the case area

Dataset group	Observation times (CET) of the data sub-sections	Number of observations at each WS point
$LST_{TERRA\text{-}DAY}$	10:36 – 11:00	192
	11:06 – 11:36	190
$LST_{AQUA\text{-}DAY}$	12:30 – 12:48	125
	12:54 – 13:18	148
$LST_{TERRA\text{-}NIGHT}$	21:30 – 21:48	117
	21:54 – 22:18	94
$LST_{AQUA\text{-}NIGHT}$	01:42 – 02:00	93
	02:06 – 02:30	108

3.5. Deriving near-surface temperatures

After obtaining information on the behaviours of LST and T_{air} datasets with respect to one another at the specified U2Os, the derived relationships between these data were further addressed with an effort to attain T_{air} with a better agreement (Firat Ors and Mahdavi 2021).

For that purpose, additional input parameters that may potentially assist this objective was explored. This was carried out building upon a considerable number of previous works as discussed earlier in the background chapter (see, Benali et al. 2012; Irger 2014; Schneider dos Santos 2020; Shi et al. 2016; Yoo et al. 2018; Zakšek and Schroedter-Homscheidt 2009 amongst others).

3.5.1. Complementary datasets

3.5.1.1. Building-related attributes of the U2Os

Based on the afore-mentioned considerations, as a first step, the building-related attributes calculated for the specified U2Os were included to the "matched" datasets of ground- and satellite-based thermal observations (LST and T_{air}) (Firat Ors and Mahdavi 2021).

As discussed earlier, these parameters represent the geometrical features of the (built) environment within a "radius" which potentially affects the observed T_{air} ("circle of influence" (see, for instance, Oke 2006; Skarbit et al. 2017; Stewart and Oke 2009; 2012). The idea behind considering these parameters stemmed from this, hypothesizing that employing these parameters might lead to a better performance in deriving T_{air} (Firat Ors and Mahdavi 2021; see also Irger 2014; Ho et al. 2016).

Hence, these parameters were added to the relevant, "matched" T_{air} and LST observations for all acquired data; and a larger dataset was constructed this way (Firat Ors and Mahdavi 2021). This dataset was later employed in further statistical inquiries as described later in this chapter.

3.5.1.2. Additional parameters

In addition to the afore-mentioned list of parameters that reflect the built environment within the U2Os, and only for the day-time assessments, additional parameters of "Solar Zenith Angle" (SZA) and "Black Sky Albedo" (BSA) (following Schneider dos Santos, amongst others) were also employed (Firat Ors and Mahdavi 2021).

Besides the motivation of building upon and contributing to the listed literature above, the idea behind considering these parameters is discussed in the next chapter, in relation with the findings of the previous inquiries where the relationships between the acquired thermal datasets are explored.

In this context, these parameters were added to the day-time datasets which now consisted of the related T_{air} and LST data, and the calculated geometrical attributes of the U2Os (Firat Ors and Mahdavi 2021).

Both parameters, i.e., the SZA and BSA data were selected from MODIS products (Schaaf and Wang 2015a; Vermote and Wolfe 2015a; 2015b; see also Firat Ors and Mahdavi 2021). The data distributer of these products is NASA EOSDIS LP DAAC (LP DAAC 2022).

AppEEARS (Application for Extracting and Exploring Analysis Ready Samples) was selected to access and acquire both datasets, as no pre-processing was necessary for the data to be obtained (AppEEARS 2022; AppEEARS Team 2020c; Schaaf and Wang 2015a; Vermote and Wolfe 2015a; 2015b; see also Firat

Ors and Mahdavi 2021). This was a practical option, as all relevant data filtering steps had been already carried out in GEE (2022) when the LST data was first attained.

In order to obtain SZA and BSA data, the WS points were defined in AppEEARS (2022) by their latitude and longitude (see Table 7), and the datasets were requested individually. When the processing by AppEEARS Team (2020c) was complete, the data was accessed and downloaded. By pursuing this workflow, the data provided by the pixel ("grid") covering the WS location was obtained for each of the seven WS locations in the present work and individually for SZA_{TERRA}, SZA_{AQUA} and BSA_{T+A} datasets (AppEEARS Team 2020c; Schaaf and Wang 2015a; Vermote and Wolfe 2015a; 2015b).

The SZA_{TERRA} and SZA_{AQUA} datasets, more specifically the acquired data from the listed Terra MODIS and Aqua MODIS SZA products which contained the "solar zenith angle" information, were provided in (around) 1km resolution (Vermote et al. 2015). The data was included to this part of the analyses in order to account for the influence of solar radiation (Firat Ors and Mahdavi 2021). As the LST data employed in the present dissertation belonged to cloud-free conditions (MOD11A1_Data 2022; MYD11A1_Data 2022), solar angles potentially provide viable insights on the solar radiation arriving to the land surfaces. This is further discussed in the next chapter in relation with the research findings. Other studies considering Solar Zenith Angle for deriving T_{air} include Huang et al. (2017) and Schneider dos Santos (2020), amongst others.

On the other hand, the BSA_{T+A} data was acquired from "Black-Sky Albedo for shortwave band" and it is a joint product from Terra MODIS and Aqua MODIS (MCD43A3_Data 2022). The BSA is defined as "albedo in the absence of a diffuse component" (MCD43A3_UserGuide 2021) and the employed BSA_{T+A} data gives this information for 0.3-5.0µm interval, for the "local solar noon" and in 500m resolution (MCD43A3_UserGuide 2021). The data is provided as "temporally weighted to the ninth day of the 16 day" (MCD43A3_Data 2022). Other studies considering Black-sky Albedo for deriving T_{air} include Chen et al. 2016 and Schneider dos Santos (2020), amongst others.

Here, note that at the time of the data processing of the present dissertation, Version 6 data was the most recent version available for the MCD43A3 products. MCD43A3 products are distributed with a note of caution, stating that the outcomes provided by MCD43A3 products "may have" been influenced, "particularly over arid bright surfaces", due to "the incorrect representation of the aerosol quantities (low average high)" in other products that are employed in MCD43A3 data processing (MCD43A3_Data 2022). For that reason, and "and a few other issues", MCD43A3_Data (2022) advised "to avoid substantial use of the C6 MCD43A3 products and wait for the C6.1 products" (MCD43A3_Data 2022). A further recommendation was to consult the more detailed quality information provided with the MCD43A2 product (MCD43A3_Data 2022). Thus, this was carried out by accessing the MCD43A2 product through GEE (GEE_MCD43A2 2022; Schaaf and Wang 2015b), and after a brief assessment, it was decided to perform no further filtering on the BSA_{T+A} data other than the temporal filtering that was necessary to match these observations with the LST datasets (as mentioned below). Due to time-related concerns regarding waiting for the introduction of Version 6.1 data, and because it was considered sufficient for the purposes of the present dissertation, provided pixel values by the Version 6 of the BSA_{T+A} data products were utilized.

In this context, the obtained SZA_{TERRA}, SZA_{AQUA} and BSA_{T+A} were filtered to be assigned to the related day-time datasets based on the image dates of the LST_{DAY} data and the WS locations. Note that, as BSA_{T+A} data stem from both Terra and Aqua satellites (MCD43A3_Data 2022) and as this data assignment was performed based on the WS locations and the imaging dates, the same date $LST_{TERRA\text{-}DAY}$ and $LST_{AQUA\text{-}DAY}$ observations were matched with the same BSA_{T+A} data point.

During this process, it was noticed that some BSA_{T+A} observations were missing for some of these dates. Thus, the total number of day-time observations available for this step of the study decreased from 7255 to 6714 after these assignments (Firat Ors and Mahdavi 2021).

Note that, the linear regression results of LST and T_{air} data from the afore-mentioned categories (i.e., LST_{DAY}-T_{air}, $LST_{TERRA\text{-}DAY}$-T_{air}, $LST_{AQUA\text{-}DAY}$-T_{air}) after this data elimination can be found in Appendix 7.2.

In the light of these points, an overview of the employed SZA and BSA data is given in Table 15.

Table 16 provides the updated data distribution (that occurred due to missing BSA data) with respect to individual WS points and the LST datasets.

Table 15. SZA and BSA Datasets employed in the study (partially based on Schaaf and Wang 2015a; Vermote and Wolfe 2015a; 2015b)

Product, Version	Product name	Abbreviation
MOD09GA, v006	MODIS/ Terra Surface Reflectance Daily L2G Global 1km and 500m SIN Grid	SZA_{TERRA}
MYD09GA, v006	MODIS/ Aqua Surface Reflectance Daily L2G Global 1km and 500m SIN Grid	SZA_{AQUA}
MCD43A3, v006	MODIS/ Terra+Aqua Albedo Daily L3 Global 500m SIN Grid	BSA_{T+A}

Table 16. Number of available observations after including the BSA data

WS Locations	TERRA-DAY	AQUA-DAY	TERRA-NIGHT	AQUA-NIGHT
IS	363	285	291	229
HW	541	400	343	278
DF	550	412	350	302
MB	580	475	449	403
GE	580	469	455	404
SC	556	449	457	386
SD	597	457	452	400
All WS Locations	3767	2947	2797	2402

3.5.2. Approach

In order to explore obtaining T_{air} based on the points discussed earlier, the constructed datasets were first grouped into day-time and night-time observations. These two groups of data were explored via "multiple linear regression analyses" (see Irger 2014 amongst others).

In these inquiries, the "dependent variable" was selected as T_{air} whereas the "independent variables" were selected from the afore-mentioned parameters in the previous sub-section 3.5.1 (Firat Ors and Mahdavi 2021).

An initial overview of these parameters is given in Table 17, with respect to their (potential) employment in day-time and night-time assessments.

Table 17. List of variables employed in day-time and night-time analyses (partially based on Firat Ors and Mahdavi 2021)

Independent variables		**Evaluated models**	
Abr.	**Variable**	**Day-time**	**Night-time**
BSF	Building Surface Fraction	✓	✓
ISF	Impervious Surface Fraction	✓	✓
PSF	Pervious Surface Fraction	✓	✓
MBH	Area-weighted Mean Building Height	✓	✓
EBH	Equivalent Building Height	✓	✓
SVF	Sky View Factor	✓	✓
SZA	Solar Zenith Angle	✓	×
BSA	Black-sky Albedo	✓	×
LST_{DAY}	Land Surface Temperature (day-time)	✓	×
LST_{NIGHT}	Land Surface Temperature (night-time)	×	✓

3.5.2.1. Exploring the independent variables

For obtaining T_{air} with a good performance, and preferably through a simple procedure as possible, the independent variables listed in Table 17 were explored through several steps. The workflow described below was applied individually to the day-time and night-time datasets.

In this context, first, the inter-relationship among the independent variables were tested through correlation inquiries (following Irger 2014). This provided an initial perspective to consider which parameters together and to (preferably) refrain from using which ones within the same model. This is further explained in the text below.

Second, a series of multiple regression analyses were conducted with different combinations of the independent variables (Table 17). Here, the aim was to find the best performing model amongst the explored alternatives. This was accomplished by considering (urban-)climate-related aspects, initial insights gained from the correlation inquiries, as well as the results obtained from each considered multiple regression step. The latter two of these assessments were conducted based on the concepts, criteria and metrics described below.

As a first step, potential (multi-)collinearity among the variables were explored. For that purpose, the Variance Inflation Factors (VIFs) were calculated for the independent variables of each explored regression inquiry (following Irger 2014; Yoo et al. 2018). These VIF values and the correlation findings described earlier were evaluated together to gain insights regarding the (potential) relationships among the investigated parameters (Dormann et al. 2013; Fávero and Belfiore 2019; Hoffman 2019; Tsagris and Pandis 2021; Vu et al. 2015; see also Irger 2014; Yoo et al. 2018).

(Multi-)collinearity is a potential issue in regression inquiries where there is a certain degree of inter-relationship amongst – at least two of – the explored "independent variables" (see, for instance, Dormann et al. 2013; Fávero and Belfiore 2019; Hoffman 2019; Holmes et al. 2017; Tsagris and Pandis 2021; Vu et al. 2015).

When this situation is present, the regression "coefficients" may not reflect the actual behaviours of the related parameters on the investigated "dependent variable", besides other potential issues (Alexopoulos 2010; Dormann et al. 2013; Fávero and Belfiore 2019; Hoffman 2019; Holmes et al. 2017; Salmerón Gómez et al. 2020; Tsagris and Pandis 2021; Vu et al. 2015).

Furthermore, such an inter-relationship creates a tendency to influence the performance of the models when they are applied to new "samples" with dissimilar backgrounds (see, for instance, Dormann et al. 2013; Fávero and Belfiore 2019; Hoffman 2019; Vu et al. 2015).

In this context VIF is commonly employed metric in multi-collinearity inquiries (for instance, Irger 2014; Yoo et al. 2018). Depending on the research problem, and the discipline, the considered threshold for VIF differs, anyhow, thresholds of 5 and 10 have been commonly utilized (Dormann et al. 2013; Hoffman 2019; Irger 2014; Salmerón Gómez et al. 2020; Tsagris and Pandis 2021; Vu et al. 2015; see also Fávero and Belfiore 2019).

VIF is calculated via the Equation 3.13 below (Fávero and Belfiore 2019; Hoffman 2019; Salmerón Gómez et al. 2020; Vu et al. 2015; see also Dormann et al. 2013):

$$VIF_{(k)} = 1/(1-R_k^2) \qquad \textit{(Eq. 3.13)}$$

In Equation 3.13, R_k^2 refers to the R^2 value resulting from the multiple regression inquiry where the dependent variable is X_k, the investigated independent variable from the original multiple regression model, and the independent variables are the remaining independent variables of the original model (Dormann et al. 2013; Hoffman 2019; Salmerón Gómez et al. 2020; Vu et al. 2015; see also Fávero and Belfiore 2019).

In the present dissertation, the VIF threshold is taken as 10 (Dormann et al. 2013; Salmerón Gómez et al. 2020; see also Fávero and Belfiore 2019; Hoffman 2019). Furthermore, the regression results which contain independent variables with VIFs ranging from 5 to 10 were decided to be evaluated with caution (Vu et al. 2015, see also Irger 2014). Here, note that Hoffman (2019) suggests this evaluation range should start from 4, which is further supported by the notes of Fávero and Belfiore (2019). Irger (2014), on the other hand, practically employs a threshold of 3, while also reporting the VIFs greater than 5 (Irger 2014).

For the correlation inquiries, no strict threshold was applied in the present dissertation. As mentioned earlier, the correlation results were employed to gain a preliminary perspective between the variable pairs; and to make initial decisions regarding the regression inquiries.

Outcomes from these efforts are further discussed in the next chapter, in relation with the multiple regression analysis results.

In this context, as a second step to select the "best" performing model for the air temperature inquiries, performances of the obtained regression models were evaluated via the RMSE and Adjusted R^2 metrics.

RMSE calculation was described earlier in Equation (3.11) for the simple linear regression analyses. In multiple regression inquiries, the degrees-of-freedom (DF) term in the denominator of Equation (3.11) is taken as "n-(k+1)" (PennState 2018e). Here, "k" corresponds to how many independent variables are there in the multiple regression model (PennState 2018e).

On the other hand, the Adjusted R^2 is commonly utilized in multiple regression inquiries to assess whether including a certain variable improves the model's performance and to obtain the better performing model (PennState 2018e; 2018f). It is calculated via Equation 3.14 below (see, for instance, Karch 2020; PennState 2018e; 2018f).

$$Adjusted\ R^2 = 1 - \frac{n-1}{n-k-1}\ (1\ -\ R^2) \qquad \textit{(Eq. 3.14.)}$$

Note that, these inquiries described above were performed utilizing Microsoft_Excel (2022), Analysis_ToolPak (2022) and MATLAB® (MathWorks® 2018). RStudio (RStudio Team 2018) further assisted at some points for data evaluation purposes. Next chapter includes the results from these efforts.

3.5.2.2. Deriving day-time and night-time T_{air}

In the light of the presented framework, the initial relationships for estimating day-time and night-time near-surface air temperatures are presented in the Equations 3.15 to 3.17 below.

$$\hat{T}_{air} = b_0 + (b_1 \cdot LST_{DAY}) + (b_2 \cdot SZA) + (b_3 \cdot BSA) + LF \quad [°C] \quad (Eq.\ 3.15)$$

Equation (3.15) represents the initial relationships to be explored for deriving day-time T_{air}. The term b_0 is the intercept, whereas b_1 to b_3 refer to the estimated coefficients.

The term LF denotes the "location factor" illustrating the building-related attributes of the investigated U2O. It is represented by the Equation (3.16) below:

$$LF = (\beta_1 \cdot BSF) + (\beta_2 \cdot ISF) + (\beta_3 \cdot PSF) + (\beta_4 \cdot MBH) + (\beta_5 \cdot SVF) + (\beta_6 \cdot EBH) \quad (Eq.\ 3.16)$$

In this context, the initial relationships explored for estimating night-time T_{air} is given in Equation (3.17):

$$\hat{T}_{air} = a_0 + (a_1 \cdot LST_{NIGHT}) + LF \quad [°C] \quad (Eq.\ 3.17)$$

where, a_0 is the intercept and a_1 is the estimated coefficient for night-time LST.

As already mentioned, within the scope of the present dissertation, the relationships presented in Equations (3.15) to (3.17) were explored based on the selected regression metrics to attain the "best performing models" of the present work. The refined relationships representing these models are presented in the next chapter with further details.

4. RESULTS AND DISCUSSION

This chapter is structured under four distinctive groups of inquiries whose goals, approach, and tools are detailly presented in the previous chapter.

As such, the first group of results present the specified study areas in a quantitative manner via the calculation results from the LCZ and U2O variables (Mahdavi et al. 2013; Stewart and Oke 2012). As already mentioned, these results are further compared with the previous research effort by Vuckovic (2015) that was conducted in a subset of similar settings.

The second group of results include the initial microclimatic assessments of the selected locations by exploring LST and T_{air} interactions. Likewise, the third group includes a more focused assessment of LST and T_{air} by considering a smaller number of observations that are mutually-available at each location for the investigated dates.

Lastly, the final group of results present the outcomes of multiple regression inquiries by examining different combinations of potential influencing parameters (i.e., building-related attributes and other observational conditions) towards deriving T_{air}. Application of these findings to the specified study areas are also explored to evaluate the selected models.

4.1. Physical description of the specified areas

In the light of the points presented above, the results indicating the built environment properties of the seven specified U2Os are presented in Figures 15 and 16.

Table 18 provides an overview of these results. Further details regarding these assessments can be found in Appendix 7.1.

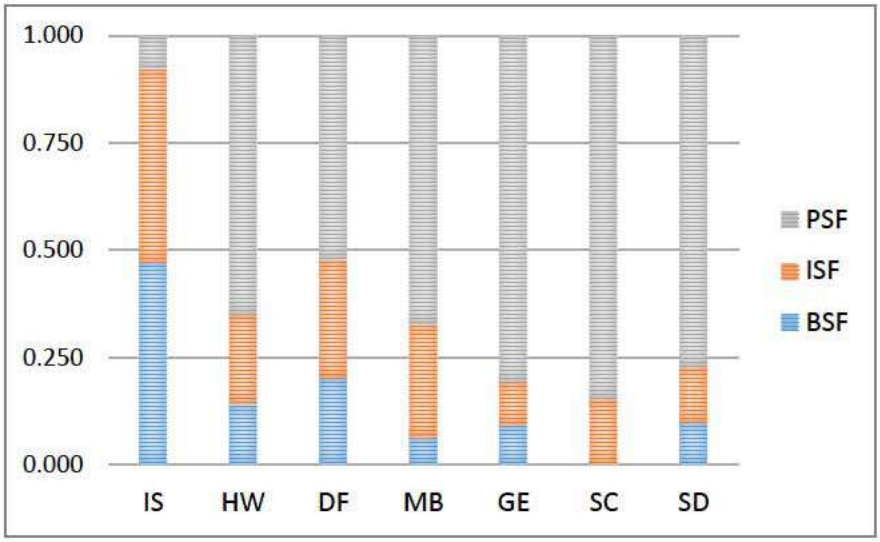

Figure 15. Calculated surface fractions for the specified U2Os (modified from Firat Ors and Mahdavi 2021)

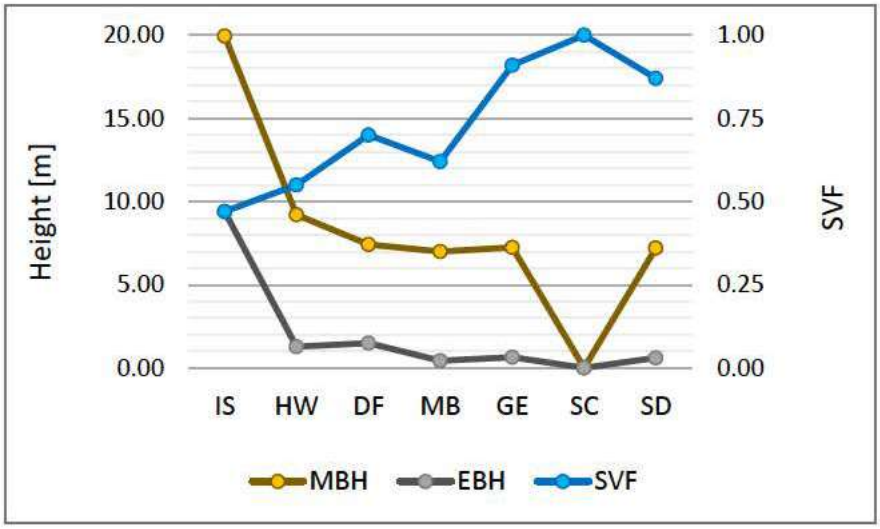

Figure 16. Relationship of SVF, MBH and EBH at different U2Os (modified from Firat Ors and Mahdavi 2021)

Table 18. Calculated building-related attributes for the specified U2Os

U2Os	BSF	ISF	PSF	MBH (m)	EBH (m)	SVF
IS	0.471	0.450	0.079	19.95	9.39	0.47
HW	0.139	0.211	0.650	9.21	1.28	0.55
DF	0.201	0.275	0.524	7.41	1.49	0.70
MB	0.062	0.264	0.674	6.99	0.43	0.62
GE	0.090	0.103	0.807	7.24	0.65	0.91
SC	0	0.153	0.847	0	0	1
SD	0.096	0.131	0.773	7.20	0.61	0.87

4.1.1. Results evaluation

Table 19 provides the comparison of the findings presented above with the results of Vuckovic (2015) for evaluation purposes. Note that, the differences in the approaches and study areas between the two works were discussed in the previous chapter.

Table 19. Comparison of the calculation results with Vuckovic (2015)

U2Os	BSF	ISF	PSF	SVF	EBH
IS - Present Work	**0.471**	**0.450**	**0.079**	**0.47**	**9.39**
IS - Vuckovic 2015	0.41	0.45	0.14	0.47	9.18
HW - Present Work	**0.139**	**0.211**	**0.650**	**0.55**	**1.28**
HW - Vuckovic 2015	0.18	0.34	0.48	0.59	1.43
DF - Present Work	**0.201**	**0.275**	**0.524**	**0.70**	**1.49**
DF - Vuckovic 2015	0.20	0.31	0.49	0.75	1.20
SD - Present Work	**0.096**	**0.131**	**0.773**	**0.87**	**0.61**
SD - Vuckovic 2015	0.08	0.09	0.83	0.87	0.45

4.2. Microclimatic behaviours: Thermal datasets

4.2.1. Obtained relationships over the case area

This sub-section includes the results obtained from the linear regression analyses conducted between the LST and T_{air} datasets.

The linear equations and further details derived from these inquiries are given in Table 20. Figures 17-22 present the scatter-plot graphs attained from these efforts. Note that, these results convey the comparison of LST and T_{air} data that were acquired over all selected locations for the present dissertation (Firat Ors and Mahdavi 2021).

Note that, in an initial visual assessment of the scatter-plots conducted between LST – T_{air} datasets, it was observed that seven data points that belong to $LST_{AQUA\text{-}NIGHT}$ data provided outlier LSTs. At a closer inspection, it was seen that all these points belonged to the same acquisition day, i.e., 04.02.2010. Therefore, these data points were removed from the datasets and were not included to any of the analysis stages in this dissertation.

Note that, Microsoft_Excel (2022) including Analysis_ToolPak (2022), and RStudio Team (2018) were employed in these afore-mentioned inquiries. MATLAB® (MathWorks® 2018) further assisted in some calculation stages.

Further regression statistics of these assessments can be found in Appendix 7.2.

Table 20. Overview of the linear regression analyses (source: modified from Firat Ors and Mahdavi 2021)

Datasets	n	R^2	SE (K)	Linear relationships (Best-fitting-lines)
LST_{DAY} - T_{air}	7255	0.903	2.60	$T_{air} = 0.7755\ LST_{DAY} - 0.1768$
LST_{NIGHT} - T_{air}	5192	0.971	1.50	$T_{air} = 0.9829\ LST_{NIGHT} + 1.8572$
$LST_{TERRA\text{-}DAY}$ - T_{air}	4104	0.904	2.60	$T_{air} = 0.7763\ LST_{TERRA\text{-}DAY} - 0.2487$
$LST_{AQUA\text{-}DAY}$ - T_{air}	3151	0.899	2.60	$T_{air} = 0.7727\ LST_{AQUA\text{-}DAY} - 0.0356$
$LST_{TERRA\text{-}NIGHT}$ - T_{air}	2797	0.975	1.42	$T_{air} = 0.9877\ LST_{TERRA\text{-}NIGHT} + 2.2809$
$LST_{AQUA\text{-}NIGHT}$ - T_{air}	2395	0.973	1.39	$T_{air} = 0.9694\ LST_{AQUA\text{-}NIGHT} + 1.4131$

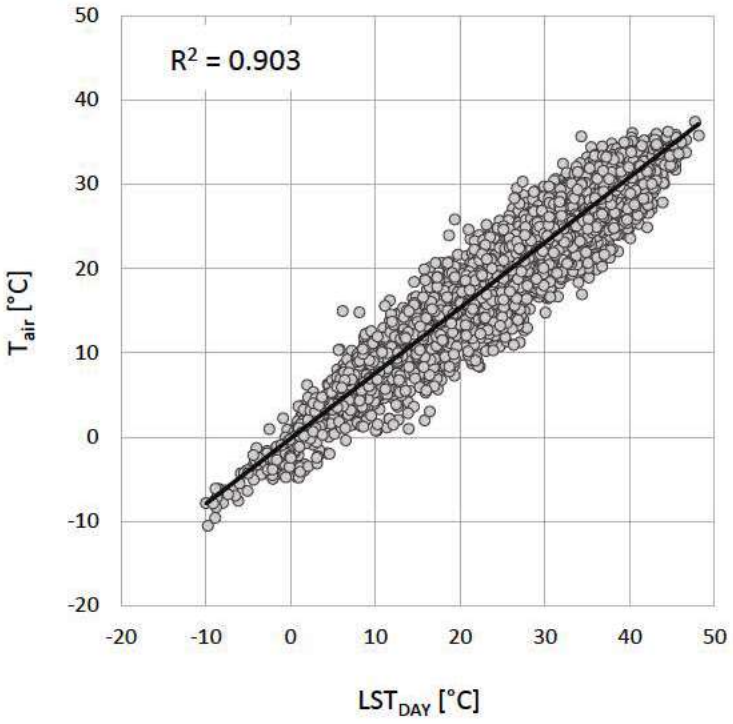

Figure 17. Relationship between day-time LST and T_{air} datasets (source: modified from Firat Ors and Mahdavi 2021)

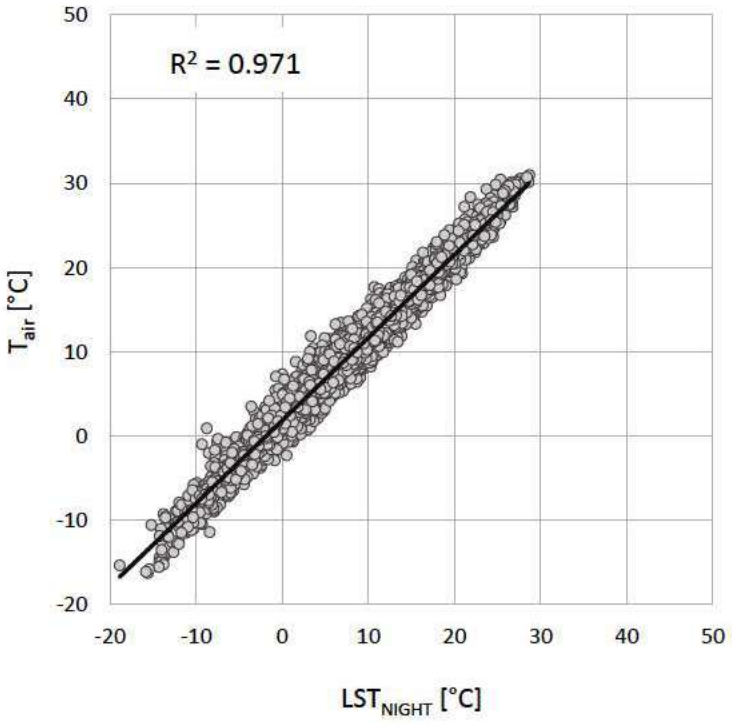

Figure 18. Relationship between night-time LST and T_{air} datasets (source: modified from Firat Ors and Mahdavi 2021)

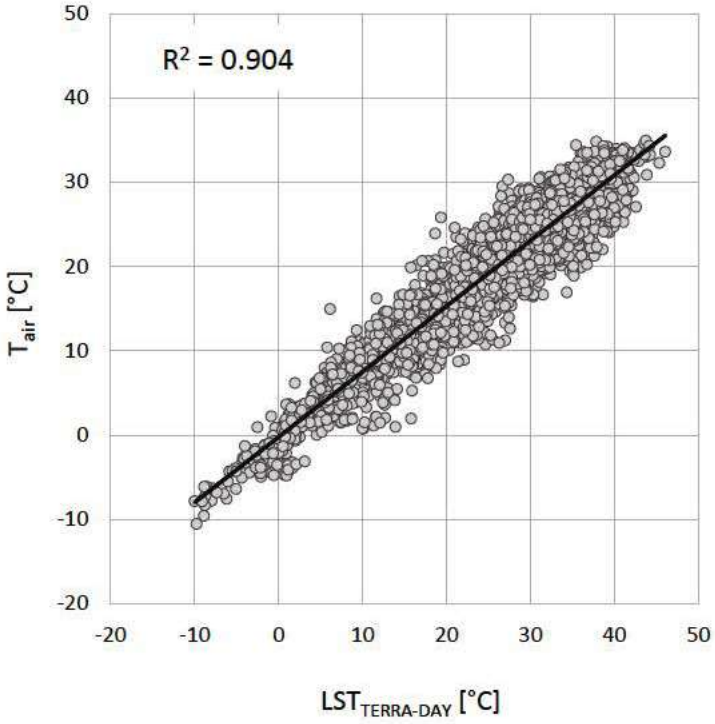

Figure 19. $LST_{TERRA\text{-}DAY}$ and T_{air} relationship

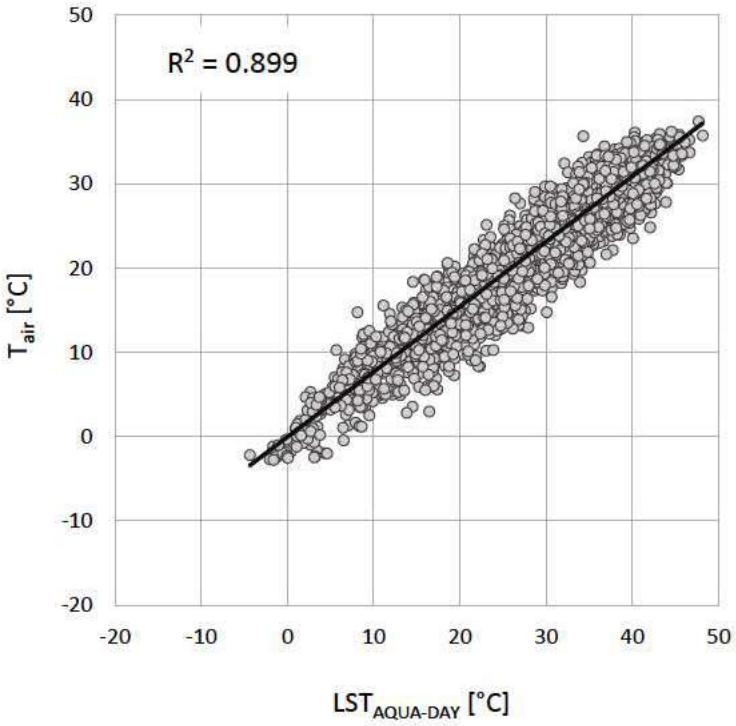

Figure 20. $LST_{AQUA\text{-}DAY}$ and T_{air} relationship

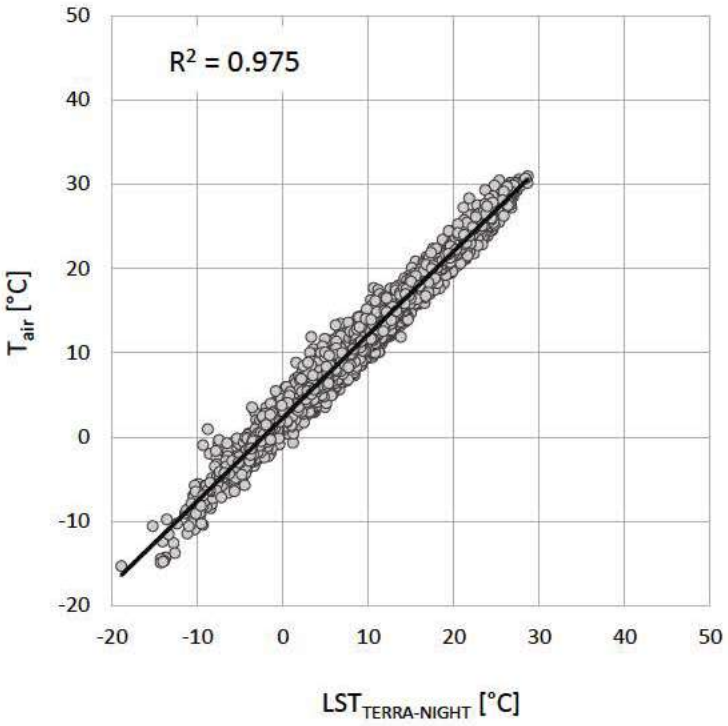

Figure 21. $LST_{TERRA\text{-}NIGHT}$ and T_{air} relationship

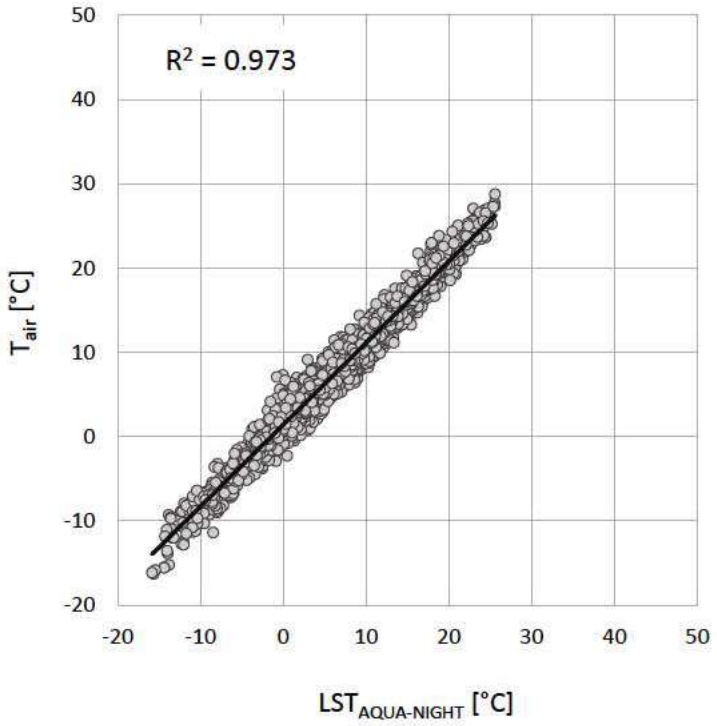

Figure 22. $LST_{AQUA\text{-}NIGHT}$ and T_{air} relationship

As indicated by the presented outcomes, all investigated combinations of LST-T_{air} data yield good relationships with each other over the case area (Firat Ors and Mahdavi 2021). As the "best-fitting lines" of these inquiries imply, T_{air} is estimated to be lower than LSTs for temperatures (approximately) greater than 0°C during the day-time overpasses of Terra and Aqua MODIS over the study area. This corresponds to late-morning and early-afternoon hours in the local time, respectively (see, Table 14). This trend seems to largely reverse during the night-time overpasses and T_{air} values are expected to be (slightly) higher than LST (Figures 18, 21, 22). These behaviours are in-line with the LST-T_{air} behaviours anticipated from the (urban) climate perspective (for instance, Voogt and Oke 1997). Moreover, findings presented by Marzban (2020) also indicate a somehow similar tendency for day-time and night-time behaviours of $LST_{TERRA\text{-}DAY}$, $LST_{TERRA\text{-}NIGHT}$, $LST_{AQUA\text{-}DAY}$ and $LST_{AQUA\text{-}NIGHT}$ (version-5) data with respect to the T_{air} measured between 2007 and 2013 by 20 WS in Berlin (Marzban 2020; Marzban et al. 2018a; 2018b (as mentioned in Marzban 2020)).

Furthermore, it is also evident from the presented outcomes that LST-T_{air} agreement is strong for each investigated dataset, and especially during night-time (Firat Ors and Mahdavi 2021). This finding is further discussed in the following parts of this chapter, in relation with the multiple regression inquiries. However, it is interesting to note that this better night-time agreement does not match with the reports of Marzban (2020) for Berlin where the author reported a better fit for the day-time comparisons (Marzban 2020). Marzban (2020) mentions this point as "contradictory" to other similar efforts which yielded better night-time agreements, giving Benali et al. (2012) as an example (Marzban 2020). Although there are differences in the approach employed by Benali et al. (2012) such as excluding Aqua data as well as other aspects that may arise from differences in "geographical location" as pointed out by Marzban (2020), one point contributing to this "contradiction" reported for Berlin in Marzban (2020) may also stem from the pursued data filtering approaches, as the presented scatter plots show considerable scattering of the data points especially in the sub-zero (°C) LSTs.

4.2.2. Obtained relationships at WS points

After presenting the obtained LST-T_{air} behaviours for all specified locations, Tables 21-24 and Figures 23-26 below include linear regression outcomes attained for the individual WS locations.

These results belong to the datasets that include $LST_{TERRA\text{-}DAY}$, $LST_{AQUA\text{-}DAY}$, $LST_{TERRA\text{-}NIGHT}$, and $LST_{AQUA\text{-}NIGHT}$ data individually, with the corresponding T_{air}.

Table 21. Relationship between $LST_{TERRA\text{-}DAY}$ and T_{air} at WS points

Location	$LST_{TERRA\text{-}DAY}$ and T_{air}			
	n	R^2	SE [K]	Linear relationships (Best-fitting-lines)
IS	478	0.880	2.44	$T_{air} = 0.7376\ LST_{TERRA\text{-}DAY} - 1.6016$
HW	567	0.938	2.08	$T_{air} = 0.8136\ LST_{TERRA\text{-}DAY} - 1.4479$
DF	599	0.937	2.15	$T_{air} = 0.7869\ LST_{TERRA\text{-}DAY} - 0.7333$
MB	615	0.944	1.97	$T_{air} = 0.8776\ LST_{TERRA\text{-}DAY} - 0.1758$
GE	601	0.939	2.13	$T_{air} = 0.8255\ LST_{TERRA\text{-}DAY} - 1.3358$
SC	625	0.931	2.25	$T_{air} = 0.7804\ LST_{TERRA\text{-}DAY} - 0.6444$
SD	619	0.914	2.55	$T_{air} = 0.8099\ LST_{TERRA\text{-}DAY} - 0.754$

Table 22. Relationship between $LST_{AQUA\text{-}DAY}$ and T_{air} at WS points

Location	$LST_{AQUA\text{-}DAY}$ and T_{air}			
	n	R^2	SE [K]	Linear relationships (Best-fitting-lines)
IS	363	0.886	2.42	$T_{air} = 0.7608\ LST_{AQUA\text{-}DAY} - 1.9663$
HW	410	0.926	2.07	$T_{air} = 0.8082\ LST_{AQUA\text{-}DAY} - 1.1533$
DF	442	0.925	2.33	$T_{air} = 0.7676\ LST_{AQUA\text{-}DAY} - 0.2641$
MB	489	0.935	2.02	$T_{air} = 0.839\ LST_{AQUA\text{-}DAY} - 0.1471$
GE	485	0.916	2.45	$T_{air} = 0.7949\ LST_{AQUA\text{-}DAY} - 0.8221$
SC	492	0.917	2.42	$T_{air} = 0.8179\ LST_{AQUA\text{-}DAY} - 0.4165$
SD	470	0.901	2.68	$T_{air} = 0.7824\ LST_{AQUA\text{-}DAY} - 0.3114$

Table 23. Relationship between $LST_{TERRA\text{-}NIGHT}$ and T_{air} at WS points

Location	$LST_{TERRA\text{-}NIGHT}$ and T_{air}			
	n	R^2	SE [K]	Linear relationships (Best-fitting-lines)
IS	291	0.992	0.92	$T_{air} = 0.9904\ LST_{TERRA\text{-}NIGHT} + 2.9438$
HW	343	0.989	1.01	$T_{air} = 0.9783\ LST_{TERRA\text{-}NIGHT} + 1.3731$
DF	350	0.986	1.13	$T_{air} = 0.9993\ LST_{TERRA\text{-}NIGHT} + 2.2953$
MB	449	0.980	1.16	$T_{air} = 0.9812\ LST_{TERRA\text{-}NIGHT} + 0.862$
GE	455	0.983	1.14	$T_{air} = 0.9948\ LST_{TERRA\text{-}NIGHT} + 2.6945$
SC	457	0.976	1.32	$T_{air} = 0.9617\ LST_{TERRA\text{-}NIGHT} + 3.0968$
SD	452	0.981	1.22	$T_{air} = 1.0118\ LST_{TERRA\text{-}NIGHT} + 2.7007$

Table 24. Relationship between $LST_{AQUA\text{-}NIGHT}$ and T_{air} at WS points

Location	$LST_{AQUA\text{-}NIGHT}$			
	n	R^2	SE [K]	Linear relationships (Best-fitting-lines)
IS	228	0.995	0.70	$T_{air} = 0.9901\ LST_{AQUA\text{-}NIGHT} + 2.3707$
HW	277	0.990	0.86	$T_{air} = 0.9690\ LST_{AQUA\text{-}NIGHT} + 0.9085$
DF	301	0.985	1.07	$T_{air} = 0.9789\ LST_{AQUA\text{-}NIGHT} + 0.8389$
MB	402	0.982	1.07	$T_{air} = 0.9778\ LST_{AQUA\text{-}NIGHT} - 0.2000$
GE	403	0.984	1.01	$T_{air} = 0.9568\ LST_{AQUA\text{-}NIGHT} + 1.6983$
SC	385	0.977	1.25	$T_{air} = 0.9326\ LST_{AQUA\text{-}NIGHT} + 2.4787$
SD	399	0.978	1.23	$T_{air} = 0.9930\ LST_{AQUA\text{-}NIGHT} + 1.9319$

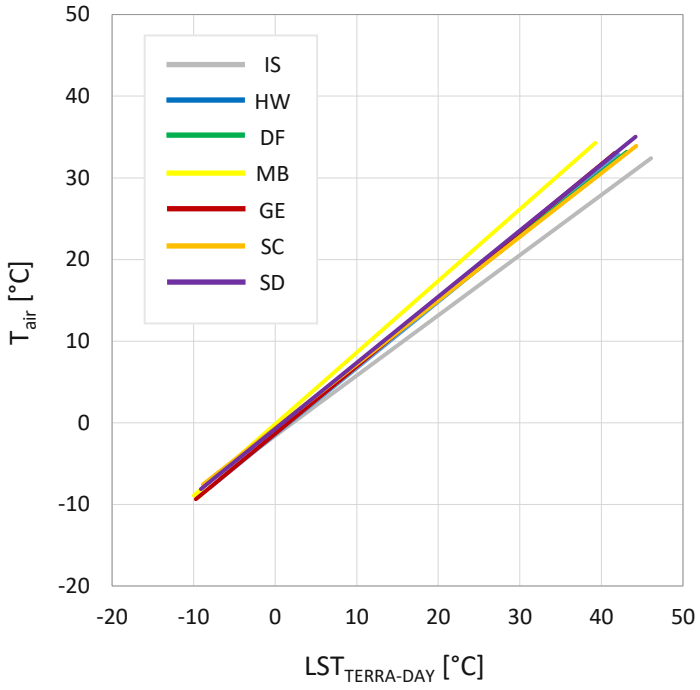

Figure 23. Relationship between $LST_{TERRA\text{-}DAY}$ and T_{air} at WS points

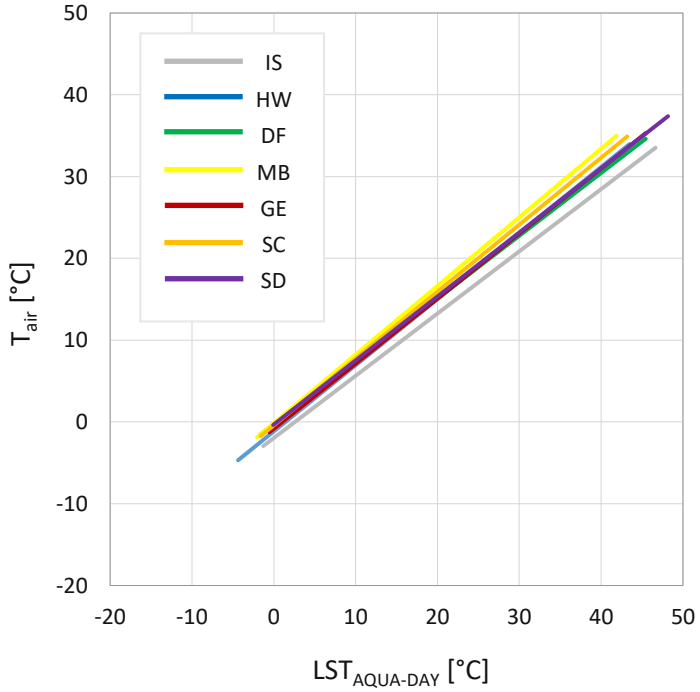

Figure 24. Relationship between $LST_{AQUA\text{-}DAY}$ and T_{air} at WS points

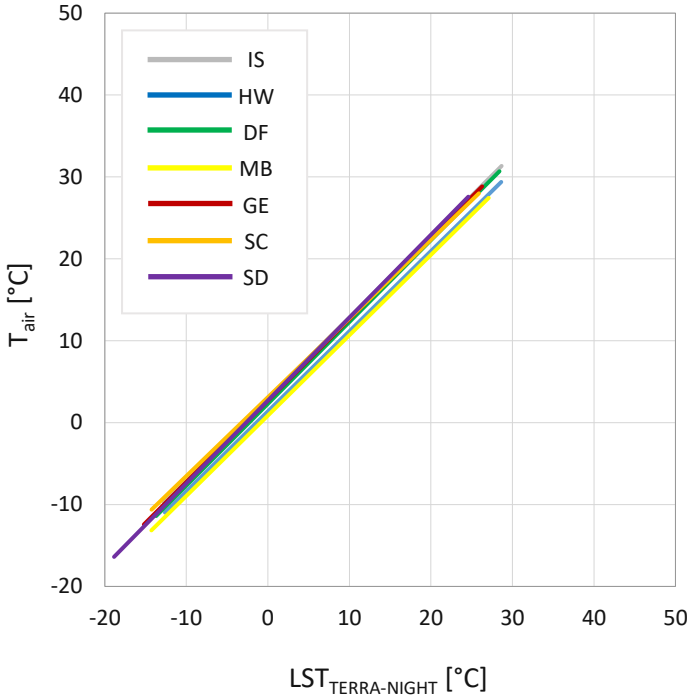

Figure 25. Relationship between $LST_{TERRA\text{-}NIGHT}$ and T_{air} at WS points

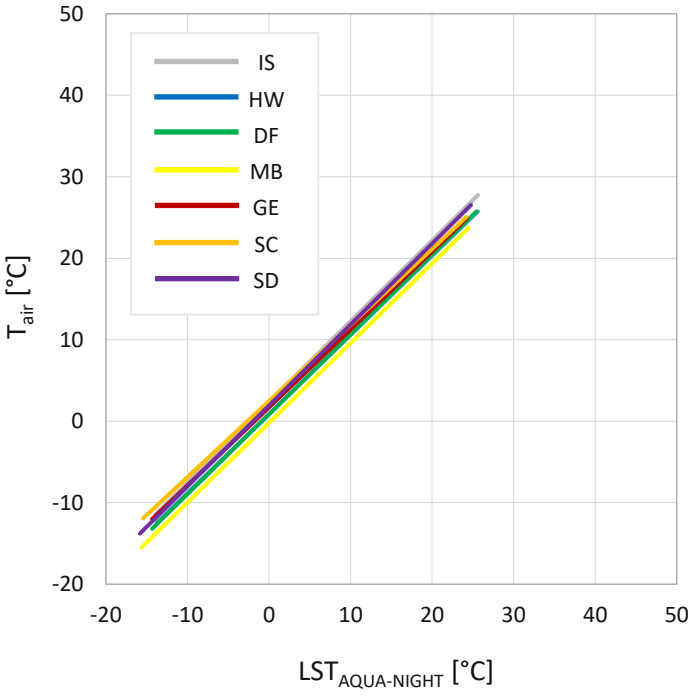

Figure 26. Relationship between $LST_{AQUA\text{-}NIGHT}$ and T_{air} at WS points

Presented outcomes above clearly illustrate the differences in the spatio-temporal tendencies of LST and T_{air} within the case area.

The day-time results suggest a more distinctive differentiation in LST-T_{air} relationship among the investigated locations. This differentiation appears to be more evident in greater temperatures, and between IS and MB locations. Moreover, the outcomes conveyed in Figures 23 and 24 suggest that the temperature difference between LST and T_{air} is expected to be smallest at the MB location, and largest at the IS location when the same LST values that are greater than (around) O°C are considered for each location in T_{air} estimations.

The night-time results imply a differentiation in LST-T_{air} behaviours among the investigated locations as well, though with more subtle differences. The behaviours at IS and MB locations again indicate a notable difference with respect to each other.

As already presented, the IS U2O presents more "urban" characteristics when compared with the other investigated locations (Table 18, Figures 15 and 16). According to the day-time results, it is associated with the largest LST-T_{air} differences, and the lowest estimated T_{air} values when the same, positive LSTs are considered for all locations. The night-time inquiries also associate the location with one of the largest T_{air} and LST differences (this time with one of the highest T_{air} estimations); but the results indicate much "smaller" differences among the investigated locations with respect to day-time.

As discussed earlier, the LST-T_{air} relationships derived for the MB location also stands out from the other WS locations, which lead to (generally) the greatest day-time and lowest night-time T_{air} estimations when the same LST value is considered across the locations.

4.2.3. Investigating LST and T_{air} at WS points

Figures 27 to 34 present the box-plots which belong to the subsets of LST and T_{air} datasets. As already mentioned, these subsets consist of same-date observations that are mutually available in all investigated locations.

Number of observations considered at each of these assessments were presented earlier in Table 14.

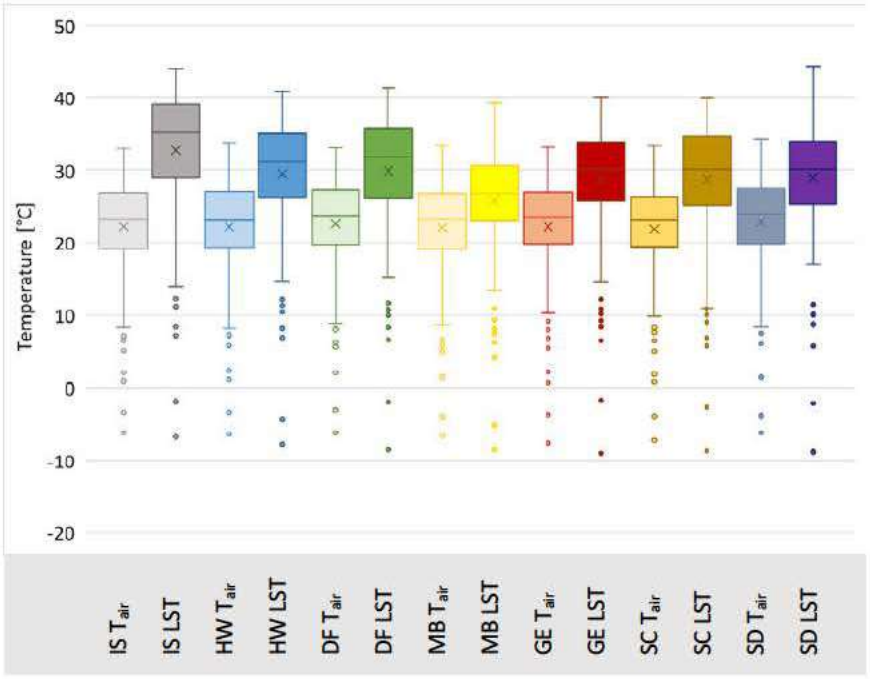

Figure 27. Distribution of T_{air} and $LST_{TERRA\text{-}DAY}$ subset-1 at selected WS points (time period: 10:36 - 11:00 CET, see Table 14)

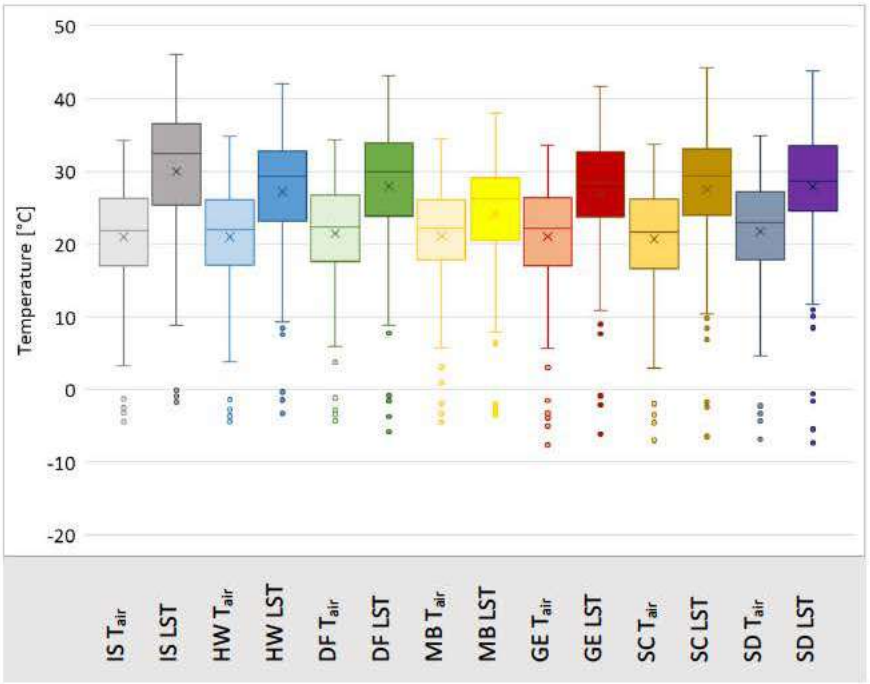

Figure 28. Distribution of T_{air} and $LST_{TERRA\text{-}DAY}$ subset-2 at selected WS points (time period: 11:06 - 11:36 CET, see Table 14)

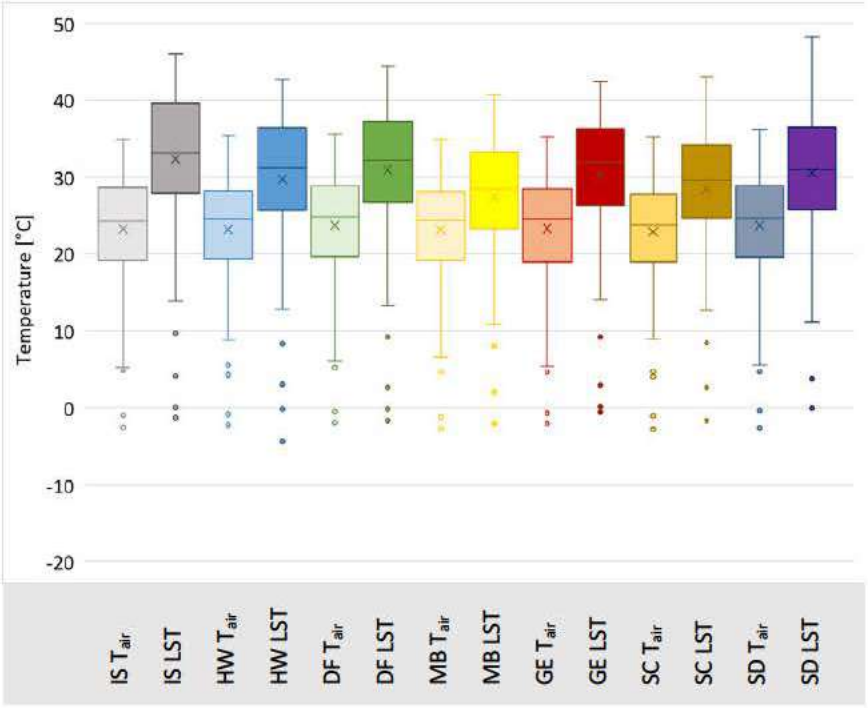

Figure 29. Distribution of T_{air} and $LST_{AQUA\text{-}DAY}$ subset-1 at selected WS points (time period: 12:30 - 12:48 CET, see Table 14)

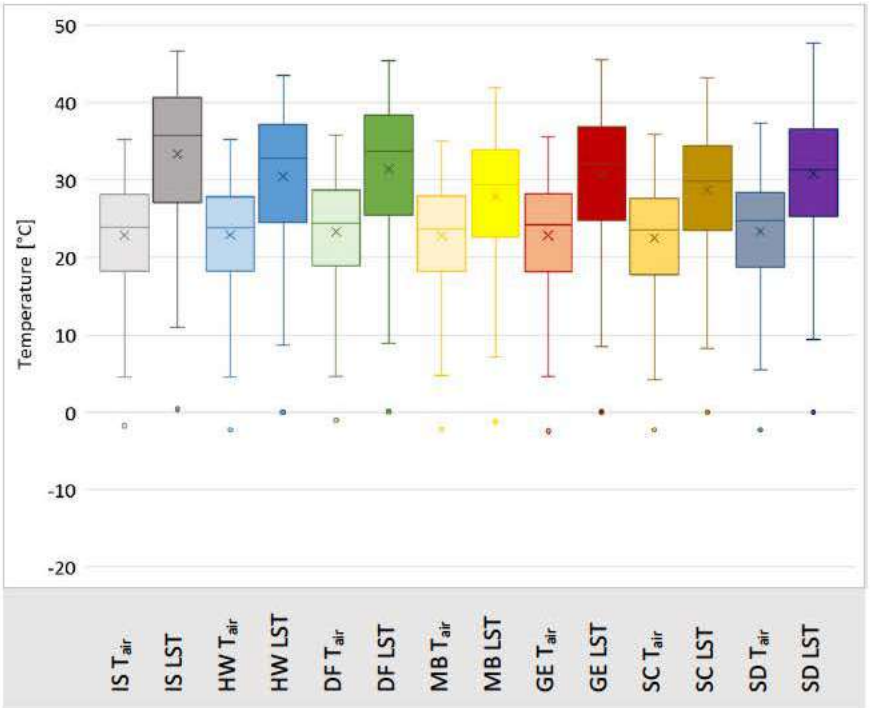

Figure 30. Distribution of T_{air} and $LST_{AQUA\text{-}DAY}$ subset-2 at selected WS points (time period: 12:54 - 13:18 CET, see Table 14)

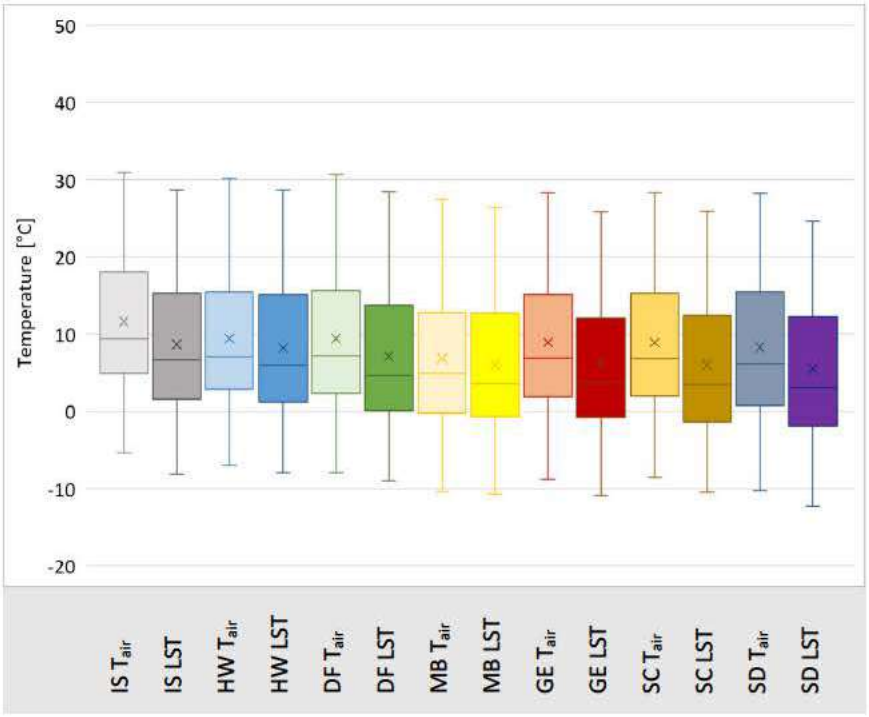

Figure 31. Distribution of T_{air} and $LST_{TERRA\text{-}NIGHT}$ subset-1 at selected WS points (time period: 21:30 - 21:48 CET, see Table 14)

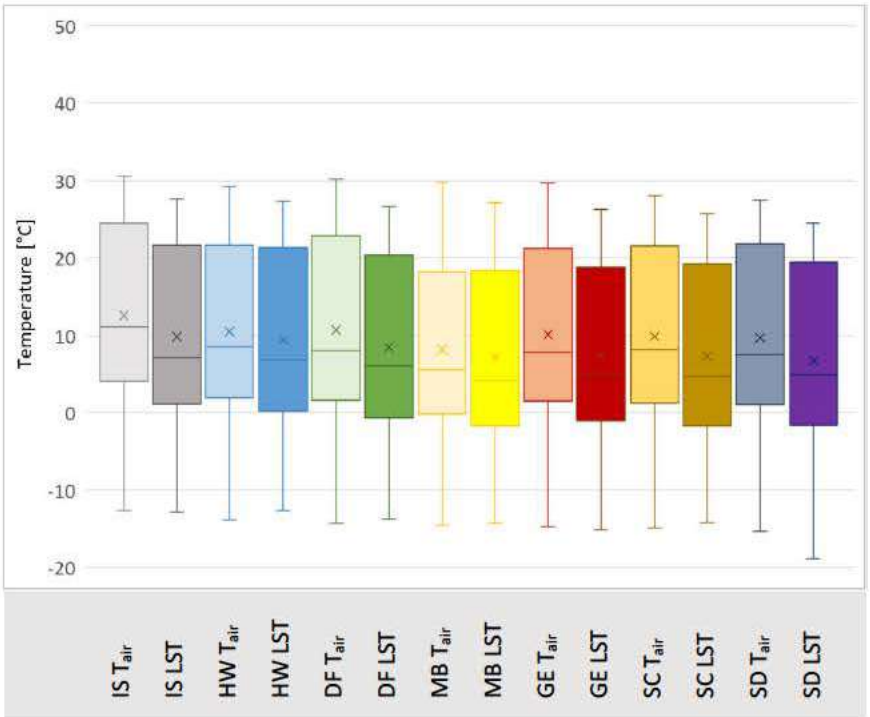

Figure 32. Distribution of T_{air} and $LST_{TERRA\text{-}NIGHT}$ subset-2 at selected WS points (time period: 21:54 - 22:18 CET, see Table 14)

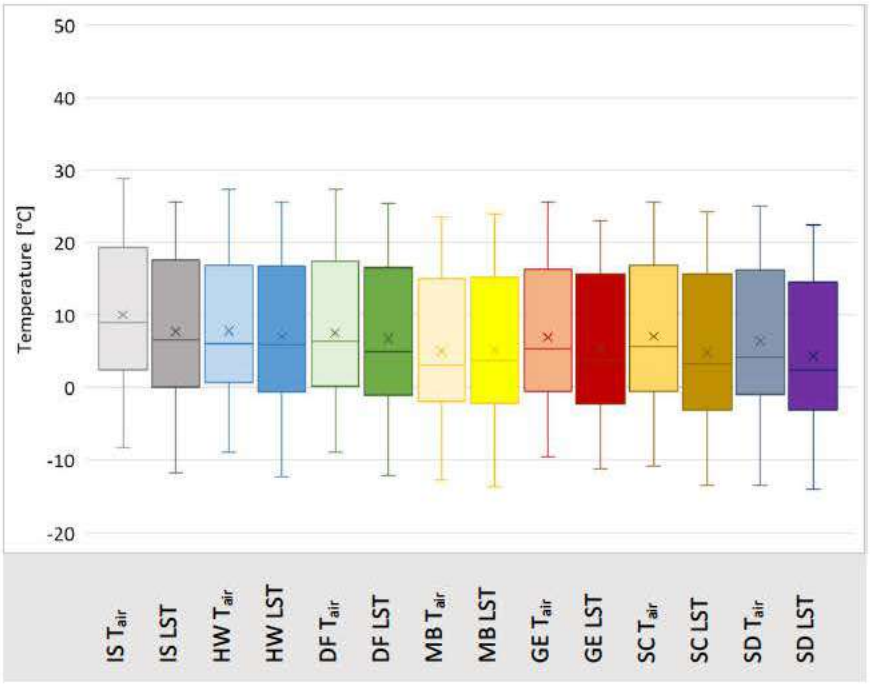

Figure 33. Distribution of T_{air} and $LST_{AQUA\text{-}NIGHT}$ subset-1 at selected WS points (time period: 01:42 - 02:00 CET, see Table 14)

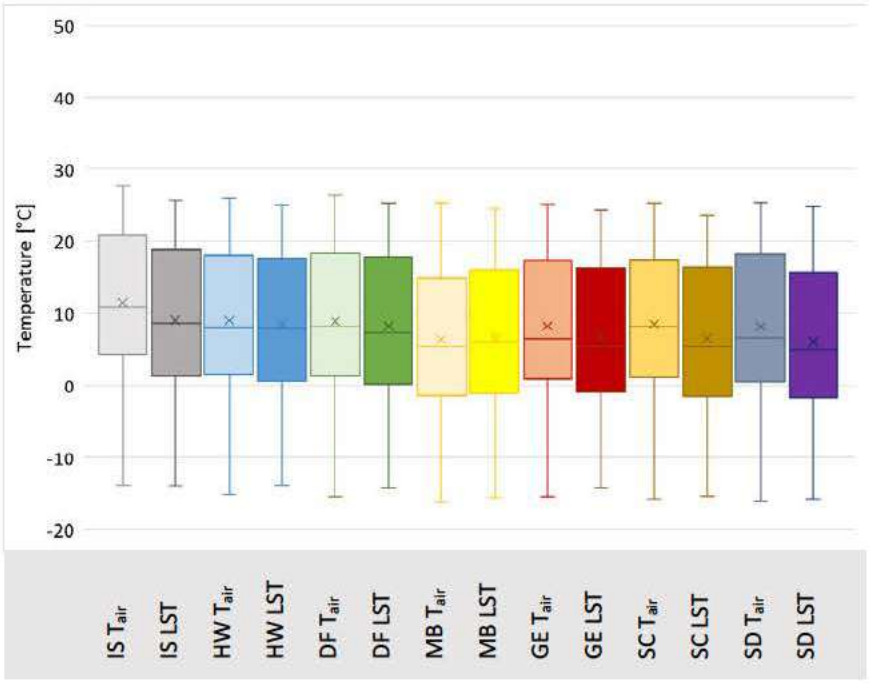

Figure 34. Distribution of T_{air} and $LST_{AQUA\text{-}NIGHT}$ subset-2 at selected WS points (time period: 02:06 - 02:30 CET, see Table 14)

The results conveyed in Figures 27-34 are to a large extent in-line with the linear regression outcomes presented in the previous sub-section.

The daytime findings indicate greater LST profiles with respect to T_{air} (Figures 27-30). Furthermore, the variation in LSTs is also higher than T_{air} among the investigated locations. This is consistent with the box-plot findings of Yoo et al. (2018) over Los Angeles and Seoul WS, where they compared the highest T_{air} (daily) with $LST_{TERRA\text{-}DAY}$ and $LST_{AQUA\text{-}DAY}$ data (Version 5) (Yoo et al. 2018).

In this context, Zakšek and Schroedter-Homscheidt (2009) explored LST-T_{air} differences in one-hour increments from 04:00 UTC to 20:00 UTC for Central Europe and concluded that LST-T_{air} difference becomes the greatest around noon, creating a sine wave plot responsive to the "solar zenith angle". For clear-sky conditions, such as the observations within the present dissertation, Zakšek and Schroedter-Homscheidt (2009) states that this pattern leads to positive day-time LST-T_{air} differences due to surface heating from sun. Furthermore, they associated the behaviour of this attained sine-wave shaped plot (in terms of its "amplitude") with the nature of surface cover, i.e., "vegetation status" (Zakšek and Schroedter-Homscheidt 2009).

In the light of these points, the results provided in Figures 27-30 are parallel with the previous findings presented in the previous sub-section and MB stands out among the other locations with a notably lower LST profile. This differentiation is more pronounced during the Terra MODIS overpasses, i.e., in earlier time frames (Figures 27, 28). On the other hand, the day-time T_{air} profiles do not present a significant differentiation among the specified U2Os.

Likewise, parallel with the earlier linear regression results, the night-time ranges of LST and T_{air} present a lower variation among the investigated locations (Figures 31-34). Again, this is consistent with the box plot analysis of Yoo et al. (2018), where they explored the lowest daily T_{air} with corresponding $LST_{TERRA\text{-}NIGHT}$ and $LST_{AQUA\text{-}NIGHT}$ data (Version 5) over Seoul and Los Angeles WS (Yoo et al. 2018).

Furthermore, the box-plots presented in Figures 31-34 indicate that T_{air} data from the IS U2O shows slightly higher characteristics with respect to the other U2Os. This is in-line with the expected T_{air} profile from the most "urbanized" study area amongst the specified U2Os, as discussed earlier in the context of the urban heat island effect (see, for instance, Voogt 2002).

It is also observed that MB T_{air} presents a lower nocturnal profile with respect to the other locations, including when it is compared with SD, i.e., the "rural" station considered for the present dissertation (see also Vuckovic 2015; Vuckovic et al. 2016 amongst others).

Parallel with these findings, Solman (2020) evaluated both locations as potential "rural" stations to be employed in urban climate simulations, and also concluded that, in general, MB presented a lower thermal profile than SD. The study outcomes further emphasized this finding where the simulation inquiries performed better when MB was considered as the rural station instead of SD (Solman 2020).

4.3. Deriving T_{air}: Day-time and night-time results

4.3.1. Day-time assessments

The results from the correlation analysis conducted among all considered parameters for day-time assessments are presented in Table 25 below. Note that, Analysis_Toolpak (2022) was employed in this inquiry.

In order to interpret the correlation analysis results, a threshold of +/- 0.90 was specified for the correlation coefficient (R). As discussed earlier, this value was not employed as a strict upper-limit but served as a first guidance towards identifying potential relationships between the variables.

Table 25. Explored parameters to derive day-time T_{air}, and associated correlation coefficients

	LST_{DAY}	BSF	ISF	PSF	MBH	SVF	EBH	SZA	BSA
LST_{DAY}	1.00								
BSF	0.21	1.00							
ISF	0.15	0.82	1.00						
PSF	-0.19	**-0.96**	**-0.94**	1.00					
MBH	0.18	**0.93**	0.73	-0.88	1.00				
SVF	-0.11	-0.68	-0.81	0.77	-0.76	1.00			
EBH	0.21	**0.95**	0.82	**-0.94**	0.89	-0.60	1.00		
SZA	-0.85	-0.08	-0.08	0.08	-0.08	0.06	-0.09	1.00	
BSA	-0.18	-0.33	-0.39	0.38	-0.40	0.53	-0.28	0.09	1.00

In this context, by considering the correlation analysis results in relation with the urban-climate-related aspects, the following decisions were initially made:

- It was decided that the models would only include two out of three surface fraction variables. For the first round of inquiries, ISF was decided to be excluded from the model, since keeping BSF and PSF in the models were hypothesized as potentially more insightful for the urban microclimate assessments.

- It was decided that BSF and MBH variables would enter or leave the models together, although the correlation results yield a strong relationship between them. In order to compensate this, it was decided to interpret their outcomes with caution by critically evaluating the associated coefficients and VIFs. Keeping both variables in the model was found to be significant for illustrating the built environment at the investigated U2Os to the extent possible.

- Following the previous point, and considering the correlation results, it was decided that the models would either include EBH, or BSF and MBH variables. From the built environment perspective, EBH – in a way – conveys a parallel information that are given by the combination of BSF and MBH variables for the "representation" of an U2O (see, Mahdavi et al. 2016; Vuckovic 2015). Therefore, it was found to be sufficient as an approach to consider them separately in the models.

In the light of these points, a series of multiple regression inquiries were conducted to derive day-time T_{air}. Following Tables 26-29 include the selected outcomes from these efforts that represent the above-mentioned workflow and the performances of the established relationships.

Note that further statistics regarding these assessments as well as other intermittent regression steps that are not provided below are presented in Appendix 7.3.1.

Note that, these inquiries were conducted by Microsoft_Excel (2022), Analysis_ToolPak (2022) and MATLAB® (MathWorks® 2018). RStudio (RStudio Team 2018) was further employed for evaluation purposes, including VIF calculations performed via the "car package" by Fox and Weisberg (2019).

Table 26. Multiple regression results for day-time: without ISF-EBH, without ISF-BSF-MBH-EBH, without ISF-PSF-EBH variables

	without ISF, EBH		without ISF, BSF, MBH, EBH		without ISF, PSF, EBH	
	Coefficients	**VIF**	**Coefficients**	**VIF**	**Coefficients**	**VIF**
Intercept	1.563	X	-7.2765	X	-2.9997	X
LST_{DAY}	0.89916	4.08	0.87708	3.97	0.89285	4.05
BSF	-34.069	**53.19**	X	X	-14.737	**7.40**
ISF	X	X	X	X	X	X
PSF	-10.082	**36.52**	7.3573	2.66	X	X
MBH	0.24947	**15.12**	X	X	0.073723	**9.35**
SVF	-0.53424*	**6.62***	-5.7679	3.07	-4.3988	2.90
EBH	X	X	X	X	X	X
SZA	0.087674	3.83	0.073448	3.76	0.083145	3.81
BSA	7.0365	1.46	6.4656	1.45	7.0172	1.46
Models' Performance						
Adjusted R^2	0.920		0.913		0.918	
RMSE (K)	2.26		2.35		2.29	
n	6714		6714		6714	

* p-value for SVF variable is greater than 0.05 (see Appendix 7.3.1, Table 43)

As presented in Table 26, an initial assessment where ISF and EBH variables were not considered in the regression model yielded significantly high VIF results for BSF, MBH and PSF variables. Based on these findings, BSF - MBH variables and PSF variable were not included to the next two multiple regression inquiries, respectively.

In these two assessments, it was observed that the "p-value" for all investigated variables were now lower than 0.05, indicating that all evaluated parameters had a significant influence on day-time T_{air} (for instance, PennState 2018g; see Appendix 7.3.1, Tables 44 and 45). These results further indicated that, the coefficient for SZA variable was considerably close to 0 for both inquiries. Therefore, the models were once more tested without SZA variable to assess if keeping the variable in the models was beneficial in terms of models' performance. The outcomes are presented in Table 27.

Table 27. Multiple regression results for day-time T_{air}: without ISF-BSF-MBH-SZA-EBH and without ISF-PSF-SZA-EBH variables

	without ISF, BSF, MBH, SZA, EBH		without ISF, PSF, SZA, EBH	
	Coefficients	**VIF**	**Coefficients**	**VIF**
Intercept	-1.7752	X	2.6999	X
LST_{DAY}	0.79489	1.07	0.79926	1.08
BSF	X	X	-13.265	**7.28**
ISF	X	X	X	X
PSF	6.6945	2.57	X	X
MBH	X	X	0.067668	**9.35**
SVF	-5.1205	3.01	-3.7905	2.86
EBH	X	X	X	X
SZA	X	X	X	X
BSA	4.1885	1.43	4.4129	1.43
Models' Performance				
Adjusted R^2	0.910		0.913	
RMSE (K)	2.40		2.35	
n	6714		6714	

As the Adjusted R^2 and SE values given in Table 27 suggest, including the SZA variable lead to a better performance for both inquiries. However, it was observed that the associated coefficients and VIF values for LST_{DAY} variable was noticeably influenced when SZA was not considered in the models.

Furthermore, it was noted that, the models where ISF, PSF, and EBH variables were not considered (with and without SZA) yielded better results with respect to the other explored models with reasonable (but, with a higher range of) VIFs. From the urban-climate related aspects, it was not found to be a sufficient "representation" of the surrounding built environment when ISF and PSF variables were both missing from the models. Thus, it was decided that it would be more insightful to explore this point with a spatial dataset with richer variations than the present study employed.

Considering these points, and in-line with the initial decisions presented earlier about simultaneously considering (or not considering) which parameters together, multiple regression analyses were conducted without BSF and MBH variables (instead of EBH) to evaluate the models' performance. These outcomes are presented in Table 28.

Note that, in the first step, this approach provided the opportunity to test ISF and PSF variables and EBH variable within the same model, illustrating pervious and impervious surfaces as well as the buildings within the investigated U2Os.

Table 28. Multiple regression results for day-time T_{air}: without BSF-MBH, without BSF-MBH-PSF, without BSF-MBH-ISF variables

	without BSF, MBH		**without BSF, MBH, PSF**		**without BSF, MBH, ISF**	
	Coefficients	**VIF**	**Coefficients**	**VIF**	**Coefficients**	**VIF**
Intercept	-16.11	X	-6.4322	X	-4.0714	X
LST_{DAY}	0.89446	4.06	0.88487	4.00	0.88181	3.99
BSF	X	X	X	X	X	X
ISF	17.155	**13.09**	6.8172	**5.88**	X	X
PSF	11.244	**39.66**	X	X	0.96437*	**17.81***
MBH	X	X	X	X	X	X
SVF	-3.1071	4.09	-1.5585	3.56	-3.8595	4.00
EBH	-0.17601	**13.74**	-0.65061	3.31	-0.45564	**11.35**
SZA	0.084177	3.82	0.077338	3.77	0.075393	3.76
BSA	6.5058	1.45	6.5304	1.45	6.835	1.45
Models' Performance						
Adjusted R^2	0.919		0.916		0.915	
RMSE (K)	2.28		2.31		2.33	
n	6714		6714		6714	

* p-value for the PSF variable is greater than 0.05 (see Appendix 7.3.1, Table 51)

The results presented in Table 28 indicate VIFs that are notably greater than the specified threshold of 10 for ISF, PSF and EBH variables when only BSF and MBH were excluded from the analysis. Therefore, it was decided to individually exclude ISF and PSF from the models in the next two steps, respectively (Table 28).

As already mentioned, this was also guided by the motivation that at least two variables illustrating the surface fractions would be included to the models at the same analysis. This would also allow for – indirectly – considering the third fraction variable. These inquiries yielded a better performance when PSF variable was not considered within the model (Table 28). Due to the considerations mentioned earlier about the SZA variable, further inquiries were performed by excluding SZA from this model. Additionally, SVF variable was also excluded in the final step to observe how the coefficients, the associated VIFs, and the model performance would respond. This decision was made to observe the VIFs and associated coefficients among the location factor variables, as VIF of ISF was slightly higher than 5 (Table 28). The results are given in Table 29.

Table 29. Multiple regression results for day-time T_{air}: without PSF-BSF-MBH-SZA and without PSF-BSF-MBH-SZA-SVF variables

	without PSF, BSF, MBH, SZA		**without PSF, BSF, MBH, SZA, SVF**	
	Coefficients	**VIF**	**Coefficients**	**VIF**
Intercept	-0.7371	X	-1.8266	X
LST_{DAY}	0.79812	1.08	0.7974	1.07
BSF	X	X	X	X
ISF	6.1959	**5.86**	8.1508	3.36
PSF	X	X	X	X
MBH	X	X	X	X
SVF	-1.2982	3.56	X	X
EBH	-0.59256	3.22	-0.60549	3.15
SZA	X	X	X	X
BSA	4.1578	1.43	2.3376	1.22
Models' Performance				
Adjusted R^2	0.912		0.912	
RMSE (K)	2.36		2.37	
n	6714		6714	

Based on the presented results in Tables 26-29, the model where BSF, MBH and PSF variables were not considered in T_{air} estimations (Table 28) was decided to be selected as the better performing model for the daytime assessments of the present dissertation.

This model is utilized in the next steps of the work for deriving day-time T_{air}, in order to test its performance at each specified U2O individually. This is presented later in the chapter.

However, it is of significance to note here that, in an additional analysis (see Appendix 7.3.1, Table 54) it was found that excluding SVF variable from this model yielded a similar performance for deriving day-time T_{air} for the investigated dataset. This was also decided to be evaluated as a part of a future study with a richer dataset in terms of spatial characteristics and detail.

Moreover, it would also be beneficial for future efforts to test the inclusion of SZA variable, as well as the elevated VIFs in ISF variable to see if keeping these variables in the models yield also better results for other explored samples.

All in all, when compared with the initial case where only T_{air} and LST_{DAY} data were explored, the obtained results show an improvement from R^2 0.896 (see Appendix 7.2, Table 42) to the adjusted R^2 0.916 and from RMSE 2.57K to RMSE 2.31K for the day-time assessments.

4.3.2. Night-time assessments

A similar workflow with the day-time assessments was followed to obtain a relationship that would derive night-time T_{air} with a good performance over the investigated locations. Table 30 presents an initial assessment of the considered parameters for this objective.

In this context, the selection of independent variables that would be employed in each step was also conducted following the principles presented earlier for the day-time inquiries, employing the afore-mentioned tools (Analysis_ToolPak 2022; Fox and Weisberg 2019; MathWorks® 2018; Microsoft_Excel 2022; RStudio Team 2018). Tables 31 and 32 present the outcomes from these efforts.

Further details regarding these assessments and additional steps that are not presented below can be found in Appendix 7.3.2, Tables 56 to 63.

Table 30. Explored parameters to derive night-time T_{air}, and associated correlation coefficients

	LST_{NIGHT}	BSF	ISF	PSF	MBH	SVF	EBH
LST_{NIGHT}	1.00						
BSF	0.05	1.00					
ISF	0.04	0.82	1.00				
PSF	-0.05	**-0.96**	**-0.94**	1.00			
MBH	0.05	**0.93**	0.73	-0.88	1.00		
SVF	-0.04	-0.69	-0.83	0.78	-0.77	1.00	
EBH	0.05	**0.96**	0.82	**-0.94**	0.89	-0.62	1.00

Table 31. Multiple regression results for night-time: without ISF-EBH, without ISF-BSF-MBH-EBH, without ISF-PSF-EBH variables

	without ISF, EBH		**without ISF, BSF, MBH, EBH**		**without ISF, PSF, EBH**	
	Coefficients	**VIF**	**Coefficients**	**VIF**	**Coefficients**	**VIF**
Intercept	-4.2038	X	-0.21346	X	-3.4867	X
LST_{NIGHT}	0.98291	1.00	0.98351	1.00	0.98303	1.00
BSF	10.324	**56.75**	X	X	7.3418	**7.55**
ISF	X	X	X	X	X	X
PSF	1.5566	**39.21**	-4.5617	2.60	X	X
MBH	-0.032671	**16.69**	X	X	-0.0043805*	**9.85***
SVF	5.2057	**6.98**	6.6976	2.60	5.8411	2.52
EBH	X	X	X	X	X	X
Models' Performance						
Adjusted R^2	0.979		0.978		0.979	
RMSE (K)	1.27		1.30		1.27	
n	5192		5192		5192	

* p-value for the MBH variable is greater than 0.05 (see Appendix 7.3.2, Table 58)

Similar with the day-time assessments, the regression results given in Table 31 indicate undesirably high VIF values for BSF, PSF and MBH variables suggesting that the estimated coefficients would be more reliable when these parameters would not be considered together within the same model (for instance, Alexopoulos 2010).

On the other hand, when ISF, PSF and EBH parameters were not included to the night-time analyses, the results further demonstrate considerably high VIF values for MBH and BSF variables, but also indicating that MBH parameter did not have a significant contribution to the model (see Appendix 7.3.2, Table 58).

Based on these results, the model which did not consider ISF, BSF, MBH and EBH variables yielded notably better VIFs and a good performance. Once more, it was decided to be evaluated within the scope of a future work with more spatial variation to see if the captured agreement in deriving T_{air} would remain similar. In this context, further analyses were performed with different combinations of the considered variables. The outcomes from these efforts are presented in Table 32.

Table 32. Multiple regression results for night-time: without BSF-MBH, without BSF-MBH-PSF, without BSF-MBH-ISF variables

	without BSF, MBH		**without BSF, MBH, PSF**		**without BSF, MBH, ISF**	
	Coefficients	**VIF**	**Coefficients**	**VIF**	**Coefficients**	**VIF**
Intercept	1.5378	X	-1.366	X	-2.6482	X
LST_{NIGHT}	0.98284	1.00	0.98289	1.00	0.98308	1.00
BSF	X	X	X	X	X	X
ISF	-6.2076	**12.88**	-3.086	**6.22**	X	X
PSF	-3.6798	**43.02**	X	X	0.10307*	**20.78***
MBH	X	X	X	X	X	X
SVF	4.9175	3.97	4.344	3.26	5.1941	3.89
EBH	0.21322	**15.63**	0.37572	3.20	0.32257	**12.87**
Models' Performance						
Adjusted R^2	0.980		0.979		0.979	
RMSE (K)	1.26		1.27		1.27	
n	5192		5192		5192	

* p-value for the PSF variable is greater than 0.05 (see Appendix 7.3.2, Table 62)

Among all explored combinations of investigated building-related parameters for the night-time assessments, the model which excluded BSF, MBH and PSF variables yielded a better performance in deriving T_{air} based on the criteria and considerations discussed earlier. A further assessment (see Appendix 7.3.2, Table 63) also indicated a similar performance when the ISF variable was also not considered in this model. This is also an interesting point to explore in further studies.

All in all, the model which does not include BSF, MBH and PSF variables was selected to be employed in deriving T_{air} over the selected WS locations (Table 32). The outcomes from these efforts are presented in the next sub-section to better assess the presented results.

Furthermore, it is of interest to note that a slight improvement was observed in the obtained results, when compared with the simple linear regression outcomes between LST_{NIGHT} and T_{air}, from 0.971 R^2 to the adjusted R^2 of 0.979 and RMSE of 1.50K to RMSE of 1.27K.

4.3.3. Model performance

Based on the presented outcomes earlier, the multiple regression equations that were employed to derive day-time T_{air} is presented in Equation (4.1) below:

$$\hat{T}_{air} = -6.4322 + (0.88487 \cdot LST_{DAY}) + (0.077338 \cdot SZA) + (6.5304 \cdot BSA) + LF_{DAY} \quad [°C] \quad \text{(Eq. 4.1)}$$

In Equation (4.1), LF_{DAY} is the "location factor" of the investigated U2O to be employed in deriving day-time T_{air}. It is calculated via Equation (4.2) below (see Table 28, Equation (3.16)):

$$LF_{DAY} = (6.8172 \cdot ISF) - (1.5585 \cdot SVF) - (0.65061 \cdot EBH) \quad \text{(Eq. 4.2.)}$$

On the other hand, Equation (4.3) represents the equation employed to derive night-time T_{air}, based on Table 32.

$$\hat{T}_{air} = -1.366 + (0.98289 \cdot LST_{NIGHT}) + LF_{NIGHT} \quad \text{(Eq. 4.3.)}$$

In Equation (4.3), LF_{NIGHT} is the "location factor" of the investigated area to be employed in deriving night-time T_{air}. It is calculated based on Equation 4.4 below (see Table 32, Equation (3.16)):

$$LF_{NIGHT} = (-3.086 \cdot ISF) + (4.344 \cdot SVF) + (0.37572 \cdot EBH) \qquad (Eq.\ 4.4.)$$

In this context, Tables 33 and 34 present the RMSE outcomes for the individual U2Os when Equations (4.1) – (4.4) were employed to derive T_{air}. Note that, in these assessments, related data that belongs to the same datasets utilized in multiple regression inquiries were employed. Furthermore, the "degrees of freedom" term in the denominator of RMSE formula (see Equation (3.11)) is taken as n, i.e., "the number of observations", when calculating RMSE for this part of calculations. Figures 34 and 35 further illustrate the box-plots that were generated from the estimation "errors" that result from the difference between T_{air} observations and corresponding $\hat{T}_{air}$, where the former was subtracted from the latter.

Table 33. Performance of the selected day-time model for deriving T_{air} over the specified U2Os

	IS	HW	DF	MB	GE	SC	SD
RMSE (K)	2.32	2.02	2.23	2.25	2.24	2.28	2.73
n	648	941	962	1055	1049	1005	1054

Table 34. Performance of the selected night-time model for deriving T_{air} over the specified U2Os

	IS	HW	DF	MB	GE	SC	SD
RMSE (K)	0.89	1.01	1.40	1.29	1.31	1.38	1.34
n	519	620	651	851	858	842	851

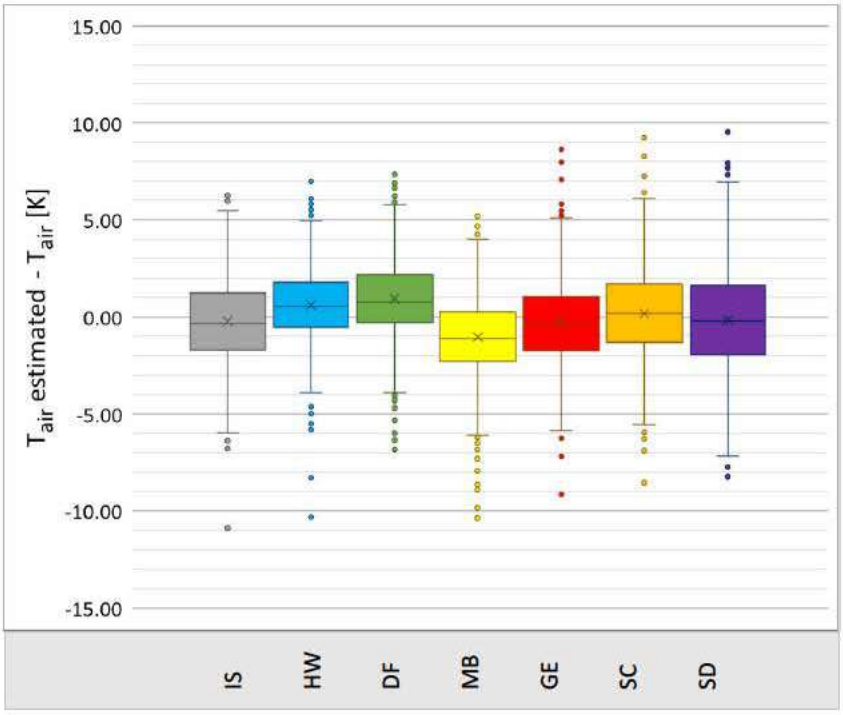

Figure 35. Box-plot analyses describing the differences between estimated and observed day-time air temperatures over WS locations

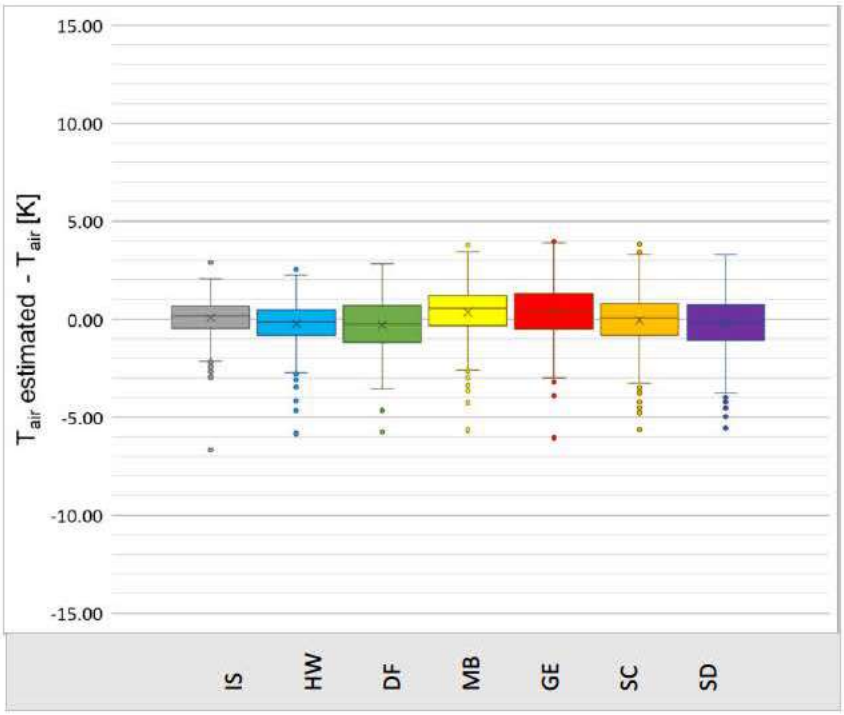

Figure 36. Box-plot analyses describing the differences between estimated and observed night-time air temperatures over WS locations

5. CONCLUSION

The present dissertation addressed the inter-relationship between the building-related features and the microclimatic conditions displayed by the urbanized settings (Firat Ors et al. 2019; Firat Ors and Mahdavi 2021; see also Irger 2014; Vuckovic 2015 amongst others). This interaction was explored by utilizing remote-sensing data including land surface temperatures, derived from satellite-based acquisitions by Moderate Resolution Imaging Spectroradiometer (MODIS) sensors (MODIS 2022a; Salomonson et al. 1989). Furthermore, terrestrially-detected near-surface air temperatures and GIS-based calculation and documentation of the building-related attributes were further employed. Calculation of the latter relied upon urban-climate-related classification efforts by Stewart and Oke (2012), i.e., Local Climate Zones (LCZs), and Mahdavi et al. (2013), i.e., Urban Units of Observations (U2Os) (Stewart and Oke 2012; Mahdavi et al. 2013).

Building on and contributing to the previous efforts (Benali et al. 2012; Irger 2014; Schneider dos Santos 2020; Shi et al. 2016; Yoo et al. 2018; Zakšek and Schroedter-Homscheidt 2009 – to name a few), the overall goal was to derive relationships that would facilitate, potentially, a rich spatial estimation of near surface air temperatures with a strong agreement (Firat Ors and Mahdavi 2021; see also Firat Ors et al. 2019). This objective was explored pursuing several steps and the associated findings are outlined as follows (partially based on Firat Ors and Mahdavi 2021; see also Firat Ors et al. 2019).

In the first step of the inquiries, significant relationships were detected – for two day-time and two night-time intervals – between the LST and T_{air} behaviours over the inspected locations: seven WS points in Austria, more specifically city of Vienna and surroundings (Firat Ors and Mahdavi 2021; see also Firat Ors et al. 2019). For these temporal and spatial conditions, it was observed that the interaction between LST and T_{air} displays a much closer agreement at the inspected night-time intervals (Firat Ors and Mahdavi 2021).

Furthermore, for the afore-mentioned assessments, the "best-fitting lines" of LST-T_{air} indicated lower T_{air} estimations with respect to LSTs for the day-time investigations. The exception here was noted for LSTs that are below, approximately, the 0°C threshold. For the inspected night-time intervals, this trend is expected to display a largely reversed behaviour. Here, T_{air} is estimated to be greater than LSTs, but with lower differences with respect to the day-time.

In the next steps of the inquiries, spatio-temporal variations were observed among the WS locations in the LST and T_{air} interactions, which are again stronger at the inspected day-time intervals. It was further gathered that, for the day-time assessments, these variations show a somehow consistent tendency for the most urbanized WS location, i.e., IS. For the same, positive LSTs across all locations, the IS location is estimated to yield the lowest T_{air} values for the day-time inquiries.

A closer inspection yielded larger LST-T_{air} differences as well as higher LST profiles for the location with respect to the other investigated locations, for each specified day-time interval. This was confirmed by comparing the medians of LST and T_{air} (via box-plots) attained over the WS locations by further grouping the data into subsets with respect to the observation times of the same-date observations. It was also noted that T_{air} profiles among the locations did not show a considerable variation in the day-time intervals. For the night-time, the box-plots indicated the highest T_{air} profiles for the most urbanized IS location, which is in-line with the spatio-temporal dynamics of the UHI phenomenon (for instance, Voogt 2002). It was also observed that the location once more yields a higher LST profile in each specified night-time interval. This was again determined based on the medians of the LST datasets, as can be observed in the box-plots.

These inquiries further yielded a distinctive profile for the MB location, which was regarded as a potential "rural" station by Solman (2020). Based on the derived relationships, the estimated T_{air} values for the location was found to be – generally – the lowest (night-time) and the highest (day-time) among the inspected locations for the same LSTs across the locations. Furthermore, it was observed that the medians of the presented box plots associate the location with the lowest LST-T_{air} differences and the lowest LSTs for the day-time inquiries when the datasets were further grouped and organized into subsets based on the same-date observations and closer observation times.

Based on these findings, it was concluded that the microclimatic conditions within the selected U2Os vary, and to a certain extent, this can be evaluated as a potential response to the built environment features of these settings (Mahdavi et al. 2013; Stewart and Oke 2012; see also Irger 2014; Vuckovic 2015; Vuckovic et al. 2016 amongst others). The last step of the inquiries explored specifically this point and sought to derive near-surface air temperature data by benefiting from the built environment attributes of the specified locations (see also, Irger 2014 amongst others).

The multiple regression results carried out for that purpose yielded that by employing LST_{DAY}, SZA, BSA parameters together with the determined "location factors" based on ISF, SVF, and EBH of the inspected U2Os, T_{air} can be estimated over all selected WS points of the present dissertation with an adjusted R^2 of 0.916 and RMSE of 2.31K for the day-time inquiry. Note that, the attained relationship between LST_{DAY} and T_{air} had yielded R^2 of 0.896, RMSE of 2.57K at the earlier steps (Firat Ors and Mahdavi 2021). For the night-time assessment, the multiple regression yielded an adjusted R^2 of 0.979 and RMSE of 1.27K when the independent variables of the model were determined as LST_{NIGHT} and the night-time "location factor" of the inspected U2O, which is calculated from, once more, ISF, SVF, and EBH of the investigated U2O. Here, the initial analyses had yielded an R^2 of 0.971 with RMSE of 1.50K between LST_{NIGHT} and T_{air}. When these two models were applied to the individual U2Os specified for the present research, RMSEs were noted between 2.02K – 2.73K for day-time and 0.89K – 1.40K for night-time, depending on the U2O. Note that, the data used in these assessments belonged to the same datasets that were used to generate these models, they were not independent samples.

Generally speaking, it can be concluded that the present research effort provided encouraging results, when all selected locations were taken into account. As such, the models can be suggested to benefit, at least slightly, from the consideration of the explored parameters. As it can be derived from the presented findings, day-time results yield a better "improvement" with respect to the night-time when the models are investigated considering all study locations. It is not a surprising outcome, considering the diurnal dynamics where the absence of incoming solar radiation limiting the LST-T_{air} interactions (for instance, Oke 1982). As already mentioned, the initial agreement between these two different thermal data types is also considerably better at the inspected

night-time intervals, emphasizing this point and also making it not an easy task for model improvement for the night-time conditions.

However, it is also evident that the performance of the models shows a variation among the inspected locations, both for day-time and night-time assessments. It is difficult to gain a good sense of the models' performance at the individual locations, given the limited spatial data availability and without introducing a new, independent sample.

This point is somehow related to one of the objectives of the present dissertation, which was to obtain a detailed spatial overview of the investigated study areas, in the basis of quantifying the building-related attributes. Here, the focus was given specifically to the "circle of influence" (for instance Oke 2006; Stewart and Oke 2012) of the weather stations at the selected study sites as the dependent variable at question was the near-surface air temperatures. Thus, GIS-based calculations of the parameters were performed accordingly, for the specified areas. As the ground-based observations were employed from seven WS points, special attention was not given to more rapid calculation possibilities for these variables, such as utilizing automatic computation techniques (see, Glawischnig et al. 2014 for their efforts in Vienna), and the employment of potential land-cover or DEM data sources via GIS or remote-sensing. Future studies may further explore the benefits and drawbacks of such approaches in relation with the obtained models (see, for instance, Hammerberg et al. 2018).

This point also leads to a potential limitation for the present dissertation, where the footprints of the obtained remote-sensing data sources and calculated building-related attributes differed from each other. Here, as already mentioned, the decision was to explore built environment characteristics based on the "circle of influence" (Oke 2006; Stewart and Oke 2012) of the terrestrial stations, and to use the pixel values of the remote-sensing data sources that correspond to the inspected weather station. The specific locations of these stations within these pixels vary from being more centrally located to being situated notably close to the pixel borders. Special attention was not given to these situations.

Furthermore, the conveyed findings reflect only the clear-sky conditions. Also, as documented by Zakšek and Schroedter-Homscheidt (2009), the LST-T_{air} interaction does not remain stable within a diurnal cycle. Although the LST_{TERRA} and LST_{AQUA} datasets provided insights from four temporal intervals, the diurnal dynamics nevertheless would make an impact on the performance

of the proposed models. Future inquiries may explore these diurnal variations to adjust the obtained models for different intervals.

Also, as mentioned briefly in the background chapter, research efforts such as Irger (2014) explore land surface temperature as a dependent variable with respect to the independent variables "representing" the built environment properties. Although the potential inter-relationships of the explored independent variables in the present dissertation were tried to be limited by consulting correlation outcomes (Irger 2014) and associated VIFs (Irger 2014; Yoo et al. 2018), the interaction of LSTs and other independent variables in the proposed models nevertheless should be further examined in future efforts with richer spatial datasets.

6. REFERENCES

Abougendia, S.M., Ayad, H.M. and El-Sayad, Z.T. (2020) 'Classification framework of Local Climate Zones using World Urban Database And Access Portal Tools: case study of Alexandria City, Egypt', in Syngellakis, S. and Hernández, S., eds., *WIT Transactions on Ecology and the Environment. Volume 241. Eleventh International Conference on Sustainable Development and Planning & Second International Conference on Urban Growth and the Circular Economy. Sustainable Development and Planning 2020. Incorporating Urban Growth 2020.*, Held online, 09 September - 11 September 2020, WIT Press, 309-322, available: https://doi.org/10.2495/SDP200251.

Akbari, H. and Matthews, H.D. (2012) 'Global cooling updates: reflective roofs and pavements', *Energy and Buildings*, 55, 2-6, available: https://doi.org/10.1016/j.enbuild.2012.02.055.

Aleksandrowicz, O., Vuckovic, M., Kiesel, K. and Mahdavi, A. (2017) 'Current trends in urban heat island mitigation research: observations based on a comprehensive research repository', *Urban Climate*, 21, 1-26, available: https://doi.org/10.1016/j.uclim.2017.04.002.

Alexopoulos, E.C. (2010) 'Introduction to multivariate regression analysis', *Hippokratia*, 14(Suppl 1), 23-28.

Ali-Toudert, F. (2021) 'Exploration of the thermal behaviour and energy balance of urban canyons in relation to their geometrical and constructive properties', *Building and Environment*, 188, 107466, available: https://doi.org/10.1016/j.buildenv.2020.107466.

Almeida, C.R.d., Teodoro, A.C. and Gonçalves, A. (2021) 'Study of the Urban Heat Island (UHI) using remote sensing data/techniques: a systematic review', *Environments*, 8(10), 105, available: https://doi.org/10.3390/environments8100105.

Analysis_Toolpak (2022) *Microsoft – Use the Analysis ToolPak to perform complex data analysis*, available: https://support.microsoft.com/en-us/office/use-the-analysis-toolpak-to-perform-complex-data-analysis-6c67ccf0-f4a9-487c-8dec-bdb5a2cefab6 [accessed 09 April 2022].

AppEEARS (2022) *The Application for Extracting and Exploring Analysis Ready Samples (AppEEARS),* available: https://lpdaac.usgs.gov/tools/appeears/ [accessed 23 January 2022].

AppEEARS Team (2020a) *Application for Extracting and Exploring Analysis Ready Samples (AppEEARS). Ver. 2.39. NASA EOSDIS Land Processes Distributed Active Archive Center (LP DAAC), USGS/Earth Resources Observation and Science (EROS) Center, Sioux Falls, South Dakota, USA*, available: https://lpdaacsvc.cr.usgs.gov/appeears [accessed 11 April 2020, 12 April 2020].

AppEEARS Team (2020b) *Application for Extracting and Exploring Analysis Ready Samples (AppEEARS). Ver. 2.46. NASA EOSDIS Land Processes Distributed Active Archive Center (LP DAAC), USGS/Earth Resources Observation and Science (EROS) Center, Sioux Falls, South Dakota, USA*, available: https://lpdaacsvc.cr.usgs.gov/appeears [accessed 05 October 2020].

AppEEARS Team (2020c) *Application for Extracting and Exploring Analysis Ready Samples (AppEEARS). Ver. 2.51. NASA EOSDIS Land Processes Distributed Active Archive Center (LP DAAC), USGS/Earth Resources Observation and Science (EROS) Center, Sioux Falls, South Dakota, USA*, available: https://lpdaacsvc.cr.usgs.gov/appeears [accessed 27 December 2020, 28 December 2020].

Aqua (2022) *NASA - Aqua Earth-observing satellite mission*, available: https://aqua.nasa.gov/ [accessed 09 April 2022].

Arnfield, A.J. (1982) 'An approach to the estimation of the surface radiative properties and radiation budgets of cities', *Physical Geography*, 3(2), 97-122, available: https://doi.org/10.1080/02723646.1982.10642221.

Arnfield, A.J. (2003) 'Two decades of urban climate research: a review of turbulence, exchanges of energy and water, and the urban heat island', *International Journal of Climatology*, 23(1), 1-26, available: https://doi.org/10.1002/joc.859.

ASHRAE (2009) *2009 ASHRAE handbook: fundamentals - IP edition*, Atlanta, GA: American Society of Heating, Refrigeration and Air-Conditioning Engineers.

ASTER (2022) *NASA - Jet Propulsion Laboratory - California Institute of Technology - ASTER Advanced Spaceborne Thermal Emission and Reflection Radiometer*, available: https://asterweb.jpl.nasa.gov/ [accessed 25 March 2022].

AustrianElevation (2022) *OGD Österreich Anwendung AustrianElevation1m (OGD Austria Application AustrianElevation1m) Official Q-GIS 3 Plug-in. Contact: Manfred Egger (https://www.egger-gis.at/)* [dataset], available: https://www.data.gv.at/anwendungen/austrianelevation1m/ [accessed 09 April 2022].

Bailey, W.G., Oke, T.R. and Rouse, W.R. (1997) *Surface climates of Canada*, Montreal, Quebec: McGill-Queen's University Press.

Barlow, J.F. (2014) 'Progress in observing and modelling the urban boundary layer', *Urban Climate*, 10, 216-240, available: https://doi.org/10.1016/j.uclim.2014.03.011.

Basemap_HIGHDPI (2021) *Basemap.at Raster HIGHDPI - Datenquelle: basemap.at/ (Data source: basemap.at/)* [dataset], available: https://basemap.at/highdpi/ [accessed 21 September 2021].

Bauer, R., Fendt, C., Jost, D., Lukacsy, M., Seidl, R. and Trautinger, F. (2020) *Vienna in figures 2020*, Vienna, Austria: Statistics Vienna, available: https://www.wien.gv.at/statistik/publikationen/uebersicht-pub.html#wiz [accessed 12 January 2022].

Benali, A., Carvalho, A.C., Nunes, J.P., Carvalhais, N. and Santos, A. (2012) 'Estimating air surface temperature in Portugal using MODIS LST data', *Remote Sensing of Environment*, 124, 108-121, available: https://doi.org/10.1016/j.rse.2012.04.024.

Benas, N., Finkensieper, S., Stengel, M., van Zadelhoff, G.J., Hanschmann, T., Hollmann, R. and Meirink, J.F. (2017) 'The MSG-SEVIRI-based cloud property data record CLAAS-2', *Earth System Science Data*, 9(2), 415-434, available: https://doi.org/10.5194/essd-9-415-2017.

Bernard, J., Bocher, E., Petit, G. and Palominos, S. (2018) 'Sky view factor calculation in urban context: computational performance and accuracy analysis of two open and free GIS tools', *Climate*, 6(3), 60, available: https://doi.org/10.3390/cli6030060.

Bretz, S., Akbari, H. and Rosenfeld, A. (1998) 'Practical issues for using solar-reflective materials to mitigate urban heat islands', *Atmospheric Environment*, 32(1), 95-101, available: https://doi.org/10.1016/S1352-2310(97)00182-9.

Cai, M., Ren, C., Xu, Y., Lau, K.K.-L. and Wang, R. (2018) 'Investigating the relationship between local climate zone and land surface temperature using an improved WUDAPT methodology – a case study of Yangtze River Delta, China', *Urban Climate*, 24, 485-502, available: https://doi.org/10.1016/j.uclim.2017.05.010.

Campbell, G.S. and Norman, J.M. (1998) *An introduction to environmental biophysics*, New York: Springer-Verlag.

Cantón, M.A., Cortegoso, J.L. and de Rosa, C. (1994) 'Solar permeability of urban trees in cities of western Argentina', *Energy and Buildings*, 20(3), 219-230, available: https://doi.org/10.1016/0378-7788(94)90025-6.

CCRS (2019) *Canada Centre for Mapping and Earth Observation (formerly Canada Centre for Remote Sensing), Natural Resources Canada. Fundamentals of Remote Sensing Tutorial*, available: https://www.nrcan.gc.ca/maps-tools-publications/satellite-imagery-air-photos/tutorial-fundamentals-remote-sensing/9309 [accessed 27 May 2021].

Chakraborty, S., Maity, I., Patel, P.P., Dadashpoor, H., Pramanik, S., Follmann, A., Novotný, J. and Roy, U. (2021) 'Spatio-temporal patterns of urbanization in the Kolkata Urban Agglomeration: a dynamic spatial territory-based approach', *Sustainable Cities and Society*, 67, 102715, available: https://doi.org/10.1016/j.scs.2021.102715.

Chapman, S., Watson, J.E.M. and McAlpine, C.A. (2016) 'Large seasonal and diurnal anthropogenic heat flux across four Australian cities', *Journal of Southern Hemisphere Earth Systems Science*, 66(3), 342-360, available: https://doi.org/10.1071/ES16022.

Chen, Y., Quan, J., Zhan, W. and Guo, Z. (2016) 'Enhanced statistical estimation of air temperature incorporating nighttime light data', *Remote Sensing*, 8(8), 656, available: https://doi.org/10.3390/rs8080656.

City of Vienna (2021a) *Wiener Stadtgebiet 2021 - Geografische eckdaten (Vienna urban area 2021 – Geographic key data)*, available: https://www.wien.gv.at/statistik/lebensraum/tabellen/stadtgebiet-eckdaten.html [accessed 15 January 2022].

City of Vienna (2021b) *Stadtgebiet - Statistiken (Urban area - Statistics)*, available: https://www.wien.gv.at/statistik/lebensraum/stadtgebiet/index.html#erlaeuterungen [accessed 18 April 2021].

City of Vienna (2021c) *Die Donau in Wien (The Danube in Vienna)*, available: https://www.wien.gv.at/umwelt/gewaesser/donau/ [accessed 18 April 2021].

City of Vienna (2021d) *Urban area*, available: https://www.wien.gv.at/english/administration/statistics/urban-area.html [accessed 18 April 2021].

City of Vienna (2021e) *Langjährige Klimamittelwerte 1981-2010 (Long-term climate averages 1981-2010)*, available: https://www.wien.gv.at/statistik/lebensraum/tabellen/klimamittelwerte-zr.html [accessed 18 April 2021].

City of Vienna (2021f) *Stadt Wien (City of Vienna)*, available: https://www.wien.gv.at/ [accessed 30 May 2021].

Conrad, O., Bechtel, B., Bock, M., Dietrich, H., Fischer, E., Gerlitz, L., Wehberg, J., Wichmann, V. and Böhner, J. (2015) 'System for Automated Geoscientific Analyses (SAGA) v. 2.1.4', *Geoscientific Model Development*, 8(7), 1991-2007, available: https://doi.org/10.5194/gmd-8-1991-2015.

Coseo, P. and Larsen, L. (2014) 'How factors of land use/land cover, building configuration, and adjacent heat sources and sinks explain Urban Heat Islands in Chicago', *Landscape and Urban Planning*, 125, 117-129, available: https://doi.org/10.1016/j.landurbplan.2014.02.019.

Crawley, D.B. (2008) 'Estimating the impacts of climate change and urbanization on building performance', *Journal of Building Performance Simulation*, 1(2), 91-115, available: https://doi.org/10.1080/19401490802182079.

Crawley, D.B. and Barnaby, C.S. (2019) 'Weather and climate in building performance simulation' in Hensen, J. L. M. and Lamberts, R., eds., *Building performance simulation for design and operation*, London (UK): Routledge, 191-220.

Dimitrova, B., Vuckovic, M., Kiesel, K. and Mahdavi, A. (2014) 'Trees and the microclimate of the urban canyon: A case study', in *Proceedings of the 2nd ICAUD International Conference in Architecture and Urban Design*, Epoka University, Tirana, Albania, 08-10 May 2014, Paper No. 262.

Dormann, C.F., Elith, J., Bacher, S., Buchmann, C., Carl, G., Carré, G., Marquéz, J.R.G., Gruber, B., Lafourcade, B., Leitão, P.J., Münkemüller, T., McClean, C., Osborne, P.E., Reineking, B., Schröder, B., Skidmore, A.K., Zurell, D. and Lautenbach, S. (2013) 'Collinearity: a review of methods to deal with it and a simulation study evaluating their performance', *Ecography*, 36(1), 27-46, available: https://doi.org/10.1111/j.1600-0587.2012.07348.x.

DSM_NOE (2020) *OGD NOE - Digitales Oberflächenmodell - 10m Niederösterreich (Digital surface model - 10m Lower Austria) Datenquelle: Land Niederösterreich - data.noe.gv.at (Data source: State of Lower Austria - data.noe.gv.at)* [dataset], available: https://www.noe.gv.at/noe/OGD_Detailseite.html?id=17c00cca-e08e-42d0-a6c9-bf8861d7f9ac [accessed 26 November 2020].

DSM_Vienna (2020) *Stadt Wien - Oberflächenmodell (DOM) (City of Vienna - Surface model (DOM)) Datenquelle: Stadt Wien – data.wien.gv.at (Data source: City of Vienna – data.wien.gv.at)* [dataset], available: https://www.wien.gv.at/stadtentwicklung/stadtvermessung/geodaten/als/ [accessed 08 December 2020].

DTM_NOE (2020) *OGD NOE - Digitales Geländemodell - 10m Niederösterreich (Digital terrain model - 10m Lower Austria) Datenquelle: Land Niederösterreich - data.noe.gv.at (Data source: State of Lower Austria - data.noe.gv.at)* [dataset], available: https://www.noe.gv.at/noe/OGD_Detailseite.html?id=46a7a06a-f69b-405e-aac2-77f775449ad3 [accessed 26 November 2020].

EOS (2022) *EOS (Earth Observing System) - NDVI*, available: https://eos.com/make-an-analysis/ndvi/ [accessed 31 March 2022].

EPA (2008) *U.S. Environmental Protection Agency (EPA). Reducing urban heat islands: compendium of strategies. Draft.*, available: https://www.epa.gov/heat-islands/heat-island-compendium [accessed 27 May 2021].

ESA_Data (2022) *The European Space Agency (ESA) Earth Online* available: https://earth.esa.int/eogateway/ [accessed 09 April 2022].

Espindola, G.M.d., Carneiro, E.L.N.d.C. and Façanha, A.C. (2017) 'Four decades of urban sprawl and population growth in Teresina, Brazil', *Applied Geography*, 79, 73-83, available: https://doi.org/10.1016/j.apgeog.2016.12.018.

Estacio, I., Babaan, J., Pecson, N.J., Blanco, A.C., Escoto, J.E. and Alcantara, C.K. (2019) 'GIS-based mapping of local climate zones using fuzzy logic and cellular automata', in Blanco, A. C., Sarmiento, C. J. S., Tupas, M. E. A. and Rahman, A. A., eds., *The International Archives of the Photogrammetry, Remote Sensing and Spatial Information Sciences, Volume XLII-4/W19, 2019, PhilGEOS x GeoAdvances 2019*, Manila, Philippines, 14–15 November 2019, 199-206, available: https://doi.org/10.5194/isprs-archives-XLII-4-W19-199-2019

Fávero, L.P. and Belfiore, P. (2019) 'Chapter 13 - Simple and Multiple Regression Models' in Fávero, L. P. and Belfiore, P., eds., *Data Science for Business and Decision Making,* Academic Press, 443-538.

Firat Ors, P. and Mahdavi, A. (2021) 'Derivation of high-resolution local thermal conditions from satellite-based data', in *Proceedings of Building Simulation 2021 Conference*, Bruges, Belgium, 1-3 September 2021.

Firat Ors, P., Vuckovic, M. and Mahdavi, A. (2019) 'Utilization of satellite-based remote-sensing for the representation of external boundary conditions in building energy modelling', in Corrado, V., Fabrizio, E., Gasparella, A. and Patuzzi, F., eds., *Proceedings of Building Simulation 2019: 16th Conference of IBPSA*, Rome, Italy, 2-4 September 2019, 4746-4753, available: https://doi.org/10.26868/25222708.2019.210126

Fox, J. and Weisberg, S. (2019) *An R companion to applied regression, Third Edition*, Thousand Oaks, CA: Sage. available: https://socialsciences.mcmaster.ca/jfox/Books/Companion/ [accessed 13 April 2022].

Gawuc, L. and Struzewska, J. (2016) 'Impact of MODIS quality control on temporally aggregated urban surface temperature and long-term surface urban heat island intensity', *Remote Sensing*, 8(5), 374, available: https://doi.org/10.3390/rs8050374.

GDAL/OGR contributors (2022) 'GDAL/OGR Geospatial Data Abstraction software Library. Open Source Geospatial Foundation.' available: https://gdal.org [accessed 10 April 2022].

GEE (2022) *Google Earth Engine (GEE)*, available: https://earthengine.google.com/ [accessed 21 January 2022].

GEE_Aqua (2022) *Earth Engine Data Catalog - MYD11A1.006 Aqua Land Surface Temperature and Emissivity Daily Global 1km* [dataset] , available: https://developers.google.com/earth-engine/datasets/catalog/MODIS_006_MYD11A1 [accessed 09 April 2022].

GEE_Catalog (2022) *Earth Engine Data Catalog*, available: https://developers.google.com/earth-engine/datasets [accessed 09 April 2022].

GEE_MCD43A2 (2022) *Earth Engine Data Catalog - MCD43A2.006 MODIS BRDF-Albedo Quality Daily 500m* [dataset], available: https://developers.google.com/earth-engine/datasets/catalog/MODIS_006_MCD43A2 [accessed 09 April 2022].

GEE_Terra (2022) *Earth Engine Data Catalog - MOD11A1.006 Terra Land Surface Temperature and Emissivity Daily Global 1km* [dataset], available: https://developers.google.com/earth-engine/datasets/catalog/MODIS_006_MOD11A1 [accessed 09 April 2022].

Geoland_Basemap Orthofoto (2021) *Katalog Orthofoto Österreich. (Catalog Orthophoto Austria). Datenquelle: basemap.at/ (Data source: basemap.at/)* [dataset], available: https://www.data.gv.at/katalog/dataset/254757be-69ef-4a6c-a4c1-1432815d7522 [accessed 21 September 2021].

Geoland_map (2022) *Geoland.at web GIS viewer - Map application*, available: https://www.geoland.at/webgisviewer/geoland/map/Geoland_Viewer/Geoland [accessed 09 April 2022].

Glawischnig, S., Hammerberg, K., Vuckovic, M., Kiesel, K. and Mahdavi, A. (2014) 'A case study of geometry-based automated calculation of microclimatic attributes', in Mahdavi, A., Martens, B. and Scherer, R., eds., *ECPPM 2014 eWork and eBusiness in Architecture, Engineering and Construction. Proceedings of the 10th European Conference on Product and Process Modelling (ECPPM 2014)*, Vienna, Austria, 17-19 September 2014, London: Taylor and Francis-Balkema, 231-236.

Google Earth (2022a) *Aerial Imagery from Gross-Enzersdorf Area - © Google - Camera: 611m, 48°11'55"N 16°33'26"E, 161m*, available: https://earth.google.com/web/search/Gro%c3%9f-Enzersdorf/@48.19937061,16.5579398,154.28225603a,566.13831337d,35y,34.31595095h,36.30115952t,0r/data=CigiJgokCfx_WaYpD0hAEQxuv9XqDkhAGaBIO0eYlTBAIWwRXhRHlDBA [accessed 14 January 2022].

Google Earth (2022b) *Aerial Imagery from Schwechat Airport Area - © Google - Camera: 965m, 48°07'00" N 16°34'53" E, 181m*, available: https://earth.google.com/web/@48.11736405, 16.58142951,180.51010191a,843.68853598d,35y,-14.8026567h,21.68003412t,0r [accessed 14 January 2022].

Google Earth (2022c) *Aerial Imagery from Seibersdorf Area - Google "Imagery ©2022 CNES / Airbus, European Space Imaging, Geoimage Austria, Maxar Technologies, Map data ©2022 Austria"* available: https://www.google.com/maps/@47.9763128,16.5069064,1023m/data=!3m1!1e3 [accessed 14 January 2022].

Gorelick, N., Hancher, M., Dixon, M., Ilyushchenko, S., Thau, D. and Moore, R. (2017) 'Google Earth Engine: Planetary-scale geospatial analysis for everyone', *Remote Sensing of Environment*, 202, 18-27, available: https://doi.org/10.1016/j.rse.2017.06.031.

Grant, G.E. (2017) *Exploring antarctic land surface temperature extremes using condensed anomaly databases*, thesis (Doctor of Philosophy), University of Colorado available: https://scholar.colorado.edu/concern/graduate_thesis_or_dissertations/bv73c0488 [accessed 09 April 2022].

GRASS Development Team (2019) 'Geographic Resources Analysis Support System (GRASS) Software, Version 7.6. Open Source Geospatial Foundation'. available: https://grass.osgeo.org [accessed 09 April 2022].

Grimmond, C.S.B., Roth, M., Oke, T.R., Au, Y.C., Best, M., Betts, R., Carmichael, G., Cleugh, H., Dabberdt, W., Emmanuel, R., Freitas, E., Fortuniak, K., Hanna, S., Klein, P., Kalkstein, L.S., Liu, C.H., Nickson, A., Pearlmutter, D., Sailor, D. and Voogt, J. (2010) 'Climate and more sustainable cities: climate information for improved planning and management of cities (Producers/capabilities perspective)', *Procedia Environmental Sciences*, 1, 247-274, available: https://doi.org/10.1016/j.proenv.2010.09.016.

Grimmond, S. (2007) 'Urbanization and global environmental change: local effects of urban warming', *The Geographical Journal*, 173(1), 83-88, available: https://doi.org/10.1111/j.1475-4959.2007.232_3.x.

Gubareff, G.G., Janssen, J.E. and Torborg, R.H. (1960) *Thermal radiation properties survey: a review of the literature*, Minneapolis, MN: Honeywell Research Center; Minneapolis-Honeywell Regulator Company.

Hammerberg, K., Brousse, O., Martilli, A. and Mahdavi, A. (2018) 'Implications of employing detailed urban canopy parameters for mesoscale climate modelling: a comparison between WUDAPT and GIS databases over Vienna, Austria', *International Journal of Climatology*, 38(S1), e1241-e1257, available: https://doi.org/10.1002/joc.5447.

Hammerberg, K.F. (2014) *Accounting for the role of trees in urban energy balance modeling using GIS techniques*, thesis (Diplom-Ingenieur), Technischen Universität Wien, reposiTUm, available: https://doi.org/10.34726/hss.2014.16409.

Han, Y., Taylor, J.E. and Pisello, A.L. (2015) 'Toward mitigating urban heat island effects: investigating the thermal-energy impact of bio-inspired retro-reflective building envelopes in dense urban settings', *Energy and Buildings*, 102, 380-389, available: https://doi.org/10.1016/j.enbuild.2015.05.040.

Harlan, S.L., Brazel, A.J., Prashad, L., Stefanov, W.L. and Larsen, L. (2006) 'Neighborhood microclimates and vulnerability to heat stress', *Social Science & Medicine*, 63(11), 2847-2863, available: https://doi.org/10.1016/j.socscimed.2006.07.030.

Ho, H.C., Knudby, A., Xu, Y., Hodul, M. and Aminipouri, M. (2016) 'A comparison of urban heat islands mapped using skin temperature, air temperature, and apparent temperature (Humidex), for the greater Vancouver area', *Science of The Total Environment*, 544, 929-938, available: https://doi.org/10.1016/j.scitotenv.2015.12.021.

Hoffman, J.I.E. (2019) 'Chapter 30 - Multiple regression' in Hoffman, J. I. E., ed., *Basic biostatistics for medical and biomedical practitioners (Second Edition)* Academic Press, 525-560.

Holmes, A., Illowsky, B. and Dean, S. (2017) '13.4 The regression equation' in *Introductory business statistics*, OpenStax, available: https://openstax.org/books/introductory-business-statistics/pages/13-4-the-regression-equation [accessed 23 January 2022].

Hu, L., Brunsell, N.A., Monaghan, A.J., Barlage, M. and Wilhelmi, O.V. (2014) 'How can we use MODIS land surface temperature to validate long-term urban model simulations?', *Journal of Geophysical Research: Atmospheres*, 119(6), 3185-3201, available: https://doi.org/10.1002/2013JD021101.

Huang, W., Li, J., Guo, Q., Mansaray, L.R., Li, X. and Huang, J. (2017) 'A satellite-derived climatological analysis of urban heat island over Shanghai during 2000–2013', *Remote Sensing*, 9(7), 641, available: https://doi.org/10.3390/rs9070641.

Irger, M. (2014) *The Effect of Urban Form on Urban Microclimate*, thesis (PhD Doctorate), The University of New South Wales, available: https://doi.org/10.26190/unsworks/16956.

Kaloustian, N. and Diab, Y. (2015) 'Effects of urbanization on the urban heat island in Beirut', *Urban Climate*, 14, 154-165, available: https://doi.org/10.1016/j.uclim.2015.06.004.

Kantzioura, A., Kosmopoulos, P., Dimoudi, A. and Zoras, S. (2015) 'Experimental investigation of microclimatic conditions in relation to the built environment in a central urban area in Thessaloniki (Northern Greece): A case study', *Sustainable Cities and Society*, 19, 331-340, available: https://doi.org/10.1016/j.scs.2015.03.006.

Karch, J. (2020) 'Improving on adjusted R-Squared', *Collabra: Psychology*, 6(1), 45 available: https://doi.org/10.1525/collabra.343.

Konarska, J., Lindberg, F., Larsson, A., Thorsson, S. and Holmer, B. (2014) 'Transmissivity of solar radiation through crowns of single urban trees—application for outdoor thermal comfort modelling', *Theoretical and Applied Climatology*, 117(3), 363-376, available: https://doi.org/10.1007/s00704-013-1000-3.

Kourtidis, K., Georgoulias, A.K., Rapsomanikis, S., Amiridis, V., Keramitsoglou, I., Hooyberghs, H., Maiheu, B. and Melas, D. (2015) 'A study of the hourly variability of the urban heat island effect in the Greater Athens Area during summer', *Science of The Total Environment*, 517, 162-177, available: https://doi.org/10.1016/j.scitotenv.2015.02.062.

Kousis, I., Pigliautile, I. and Pisello, A.L. (2021) 'Intra-urban microclimate investigation in urban heat island through a novel mobile monitoring system', *Scientific Reports*, 11, 9732, available: https://doi.org/10.1038/s41598-021-88344-y.

Krüger, E.L. (2015) 'Urban heat island and indoor comfort effects in social housing dwellings', *Landscape and Urban Planning*, 134, 147-156, available: https://doi.org/10.1016/j.landurbplan.2014.10.017.

LAADS DAAC (2022) *LAADS DAAC - Level-1 and Atmosphere Archive & Distribution System Distributed Active Archive Center - Terra & Aqua Moderate Resolution Imaging Spectroradiometer (MODIS)*, available: https://ladsweb.modaps.eosdis.nasa.gov/missions-and-measurements/modis/ [accessed 31 March 2022].

Landsat (2022) *NASA Landsat Science*, available: https://landsat.gsfc.nasa.gov/ [accessed 25 March 2022].

Latitude (2021) *Latitude – Articles by country – Austria – Vienna*, available: https://latitude.to/articles-by-country/at/austria/153/vienna [accessed 18 April 2021].

Lelovics, E., Gál, T. and Unger, J. (2013) 'Mapping local climate zones with a vector-based GIS method', in *Proceedings of the Air and Water Components of the Environment: Conference Dedicated to World Meteorological Day and World Water Day*, Cluj-Napoca, Romania, 2013, 423-430.

Lelovics, E., Unger, J., Gál, T. and Gál, C.V. (2014) 'Design of an urban monitoring network based on Local Climate Zone mapping and temperature pattern modelling', *Climate research*, 60(1), 51-62, available: https://doi.org/10.3354/cr01220.

Li, Z.-L., Tang, B.-H., Wu, H., Ren, H., Yan, G., Wan, Z., Trigo, I.F. and Sobrino, J.A. (2013) 'Satellite-derived land surface temperature: current status and perspectives', *Remote Sensing of Environment*, 131, 14-37, available: https://doi.org/10.1016/j.rse.2012.12.008.

Lillesand, T., Kiefer, R.W. and Chipman, J. (2015) *Remote sensing and image interpretation*, 7th Edition, United States of America: John Wiley & Sons.

Lim, S.J., Vuckovic, M., Kiesel, K. and Mahdavi, A. (2014) 'The variance of the urban microclimate in the City of Vienna, Austria', in *Proceedings of the 2nd ICAUD International Conference in Architecture and Urban Design*, Epoka University, Tirana, Albania, 08-10 May 2014, Paper No. 259.

Lindberg, F., Grimmond, C.S.B., Gabey, A., Huang, B., Kent, C.W., Sun, T., Theeuwes, N.E., Järvi, L., Ward, H.C., Capel-Timms, I., Chang, Y., Jonsson, P., Krave, N., Liu, D., Meyer, D., Olofson, K.F.G., Tan, J., Wästberg, D., Xue, L. and Zhang, Z. (2018) 'Urban Multi-scale Environmental Predictor (UMEP): An integrated tool for city-based climate services', *Environmental Modelling & Software*, 99, 70-87, available: https://doi.org/10.1016/j.envsoft.2017.09.020.

LP DAAC (2022) *The Land Processes Distributed Active Archive Center (LP DAAC)*, available: https://lpdaac.usgs.gov/ [accessed 10 April 2022].

LP DAAC_ASTER (2022) *LP DAAC USGS - ASTER Overview*, available: https://lpdaac.usgs.gov/data/get-started-data/collection-overview/missions/aster-overview/ [accessed 10 April 2022].

MA41_Geodata (2021) *Stadt Wien - Geodatenviewer der Stadtvermessung Wien (City of Vienna – Geodata viewer of the City Survey Vienna)* available: https://www.wien.gv.at/ma41datenviewer/public/ [accessed 27 May 2021].

Magee, N., Curtis, J. and Wendler, G. (1999) 'The urban heat island effect at Fairbanks, Alaska', *Theoretical and Applied Climatology*, 64, 39-47, available: https://doi.org/10.1007/s007040050109.

Mahdavi, A. (2018) 'Approaches to the evaluation and mitigation of the urban microclimate' in Hofbauer, C. K., Madadi-Kandjani, E. and Meuwissen, J. M. C., eds., *Climate change and sustainable heritage*, Newcastle upon Tyne (UK): Cambridge Scholars Publishing, 1-37.

Mahdavi, A., Kiesel, K. and Vuckovic, M. (2013) 'A framework for the evaluation of urban heat island mitigation measures', in *Proceedings of SB13 Munich: Implementing Sustainability – Barriers and Chances Conference*, Munich (Germany), 24-26 April 2013.

Mahdavi, A., Kiesel, K. and Vuckovic, M. (2014) 'Empirical and computational assessment of the urban heat island phenomenon and related mitigation measures', *Geographia Polonica*, 87(4), 505-516, available: http://dx.doi.org/10.7163/GPol.2014.34.

Mahdavi, A., Kiesel, K. and Vuckovic, M. (2016) 'Methodologies for UHI analysis' in Musco, F., ed., *Counteracting urban heat island effects in a global climate change scenario*, Cham: Springer International Publishing, 71-91.

Maleki, A., Orehounig, K. and Mahdavi, A. (2012) 'Monitoring and modeling of the urban micro-climate', in *Proceedings of 1-ICAUD 1st International Conference on Architecture & Urban Design* EPOKA University, Tirana (Albenia), 19-21 April 2012, 1019-1028.

Marzban, F. (2020) *Estimation of near-surface Air temperature during day and night-time from MODIS over Different LC/LU Using machine learning methods in Berlin*, thesis (Dr. rer. nat.), Freie Universität Berlin, available: https://refubium.fu-berlin.de/handle/fub188/28282.2 [accessed 09 April 2022].

Marzban, F., Conrad, T., Marban, P. and Sodoudi, S. (2018a) 'Estimation of the Near-Surface Air Temperature during the Day and Nighttime from MODIS in Berlin, Germany', *International Journal of Advanced Remote Sensing and GIS*, 7(1).

Marzban, F., Sodoudi, S. and Preusker, R. (2018b) 'The influence of land-cover type on the relationship between NDVI–LST and LST-Tair', *International Journal of Remote Sensing*, 39(5), 1377-1398, available: https://doi.org/10.1080/01431161.2017.1402386.

Mathew, A., Khandelwal, S. and Kaul, N. (2018) 'Analysis of diurnal surface temperature variations for the assessment of surface urban heat island effect over Indian cities', *Energy and Buildings*, 159, 271-295, available: https://doi.org/10.1016/j.enbuild.2017.10.062.

MathWorks® (2018) 'MATLAB - Copyright 2018 The MathWorks, Inc.'.

Maykut, G.A. (1985) *An introduction to ice in the polar oceans. Report 2nd printing, APL-UW 8510*, Department of Atmospheric Sciences, University of Washington, Seattle, WA.

MCD43A3_Data (2022) *LP DAAC Data Catalog - MCD43A3 v006 MODIS/Terra+Aqua Albedo Daily L3 Global 500 m SIN Grid* available: https://lpdaac.usgs.gov/products/mcd43a3v006/ [accessed 10 April 2022].

MCD43A3_UserGuide (2021) *University of Massachussets Boston - Professor Cyrstal Schaaf's Lab - MODIS User Guide V006 and V006.1 for MCD43 products: MCD43A3 Albedo Product*, available: https://www.umb.edu/spectralmass/terra_aqua_modis/v006/mcd43a3_albedo_product [accessed 27 May 2021].

Microsoft_Excel (2022) 'Microsoft 365 – Excel'. available: https://www.microsoft.com/en-gb/microsoft-365/excel [accessed: 10 April 2022].

Mills, G. (2014) 'Urban climatology: history, status and prospects', *Urban Climate*, 10, 479-489, available: https://doi.org/10.1016/j.uclim.2014.06.004.

Mirzaei, P.A. and Haghighat, F. (2010) 'Approaches to study Urban Heat Island – Abilities and limitations', *Building and Environment*, 45(10), 2192-2201, available: https://doi.org/10.1016/j.buildenv.2010.04.001.

MOD11 (2022) *NASA - MODIS Land -Land Surface Temperature/Emissivity (MOD11)*, available: https://modis-land.gsfc.nasa.gov/temp.html [accessed 31 March 2022].

MOD11A1_Data (2022) *LP DAAC Data Catalog - MOD11A1 v006 MODIS/Terra Land Surface Temperature/Emissivity Daily L3 Global 1 km SIN Grid*, available: https://lpdaac.usgs.gov/products/mod11a1v006/ [accessed 21 January 2022].

MOD21 (2022) *NASA - MODIS Land - Land Surface Temperature/Emissivity (MOD21)*, available: https://modis-land.gsfc.nasa.gov/temp21.html [accessed 31 March 2022].

MOD21_Data (2022) *LP DAAC Data Catalog - MOD21 v061 MODIS/Terra Land Surface Temperature/3-Band Emissivity 5-Min L2 1 km*, available: https://lpdaac.usgs.gov/products/mod21v061/ [accessed 31 March 2022].

MODIS (2022a) *NASA - Moderate Resolution Imaging Spectroradiometer (MODIS)*, available: https://modis.gsfc.nasa.gov/about/ [accessed 10 April 2022].

MODIS (2022b) *NASA - Moderate Resolution Imaging Spectroradiometer (MODIS) - Specifications*, available: https://modis.gsfc.nasa.gov/about/specifications.php [accessed 31 March 2022].

MODIS_SDST (1997) *MODIS Science Data Support Team - MODIS Level 1A Earth Location: Algorithm Theoretical Basis Document Version 3.0* available: https://modis.gsfc.nasa.gov/data/atbd/atbd_mod28_v3.pdf [accessed 21 January 2022].

MODLAND (2017) *MODLAND Tile Calculator*, available: https://landweb.modaps.eosdis.nasa.gov/cgi-bin/developer/tilemap.cgi [accessed 31 March 2022].

MODLAND (2021a) *NASA - MODIS Land - MODIS Grids*, available: https://modis-land.gsfc.nasa.gov/MODLAND_grid.html [accessed 31 March 2022].

MODLAND (2021b) *NASA - MODIS Land - MODIS Validation Strategy*, available: https://modis-land.gsfc.nasa.gov/MODLAND_val.html?_ga=2.142246641.2145581044.1647635978-80034865.1647635978 [accessed 31 March 2022].

Monaghan, A.J., Hu, L., Brunsell, N.A., Barlage, M. and Wilhelmi, O.V. (2014) 'Evaluating the impact of urban morphology configurations on the accuracy of urban canopy model temperature simulations with MODIS', *Journal of Geophysical Research: Atmospheres*, 119(11), 6376-6392, available: https://doi.org/10.1002/2013JD021227.

MYD11A1_Data (2022) *LP DAAC Data Catalog - MYD11A1 v006 MODIS/Aqua Land Surface Temperature/Emissivity Daily L3 Global 1 km SIN Grid*, available: https://lpdaac.usgs.gov/products/myd11a1v006/ [accessed 21 January 2022].

NASA (2022) *National Aeronautics and Space Administration (NASA)*, available: https://www.nasa.gov/ [accessed 09 April 2022].

NASA_Data (2022) *DATA.NASA.GOV: A catalog of publicly available NASA datasets*, available: https://data.nasa.gov/ [accessed 09 April 2022].

NASA_EOSDIS (2022) *NASA Earth Observing System Data and Information System (EOSDIS)*, available: https://earthdata.nasa.gov/eosdis [accessed 21 January 2022].

NASA_Weather (2021) *Archeological Remote Sensing Electromagnetic Spectrum - NASA Webpage - (Responsible Official: Dr. James L. Smoot, Page Author: Tom Sever, Page Curator: Diane Samuelson)*, available: https://weather.msfc.nasa.gov/archeology/remote_sensing_spectrum.html [accessed 27 May 2021].

Ng, E. (2009) 'Policies and technical guidelines for urban planning of high-density cities – air ventilation assessment (AVA) of Hong Kong', *Building and Environment*, 44(7), 1478-1488, available: https://doi.org/10.1016/j.buildenv.2008.06.013.

Ngarambe, J., Oh, J.W., Su, M.A., Santamouris, M. and Yun, G.Y. (2021) 'Influences of wind speed, sky conditions, land use and land cover characteristics on the magnitude of the urban heat island in Seoul: an exploratory analysis', *Sustainable Cities and Society*, 71, 102953, available: https://doi.org/10.1016/j.scs.2021.102953.

Nunez, M. and Oke, T.R. (1977) 'The energy balance of an urban canyon ', *Journal of Applied Meteorology and Climatology*, 16(1), 11-19, available: https://doi.org/10.1175/1520-0450(1977)016<0011:TEBOAU>2.0.CO;2.

OGD_NOE (2020) *Open Government Data - Land Niederösterreich (Open Government Data - State of Lower Austria) Datenquelle: Land Niederösterreich - data.noe.gv.at (Data source: State of Lower Austria - data.noe.gv.at)*, available: https://noe.gv.at/noe/Open-Government-Data/Open-Government-Data.html [accessed 26 November 2020].

OGD_Vienna (2021) *City of Vienna - Open Government Data (OGD) in Vienna. "Datenquelle: Stadt Wien - data.wien.gv.at" (Data source: City of Vienna - data.wien.gv.at)*, available: https://digitales.wien.gv.at/open-data/ [accessed 27 May 2021].

OGD_Vienna FMZK (2021) *Open Data Österreich – Katalog Flächen-Mehrzweckkarte Vektordaten Wien (Open Data Austria – Catalog Area Multi-purpose Map Vector Data Vienna)*, available: https://www.data.gv.at/katalog/dataset/7cf0da04-1f77-4321-929e-78172c74aa0b [accessed 1 October 2021].

Oke, T.R. (1976) 'The distinction between canopy and boundary-layer urban heat islands', *Atmosphere*, 14(4), 268-277, available: https://doi.org/10.1080/00046973.1976.9648422.

Oke, T.R. (1982) 'The energetic basis of the urban heat island', *Quarterly Journal of the Royal Meteorological Society*, 108(455), 1-24, available: https://doi.org/10.1002/qj.49710845502.

Oke, T.R. (1983) 'Surfaces, scales and scale interactions in urban climatology', presented at the *Int. Assoc. Meteorol. Atmos. Physics, IUGG Congress*, Hamburg, Abstract CL-1, 54.

Oke, T.R. (1984) 'Methods in urban climatology', in Kirchhofer, W., Ohmura, A. and Wanner, H., eds., *Applied Climatology - 25th International Geographical Congress Symposium No. 18: Applied Geography*, Zurich, 21 August 1984 - *Zürcher Geographische Schriften, 14,* 19-29.

Oke, T.R. (1987) *Boundary layer climates*, 2nd Edition ed., London: Routledge.

Oke, T.R. (1988) 'The urban energy balance', *Progress in Physical Geography: Earth and Environment*, 12(4), 471-508, available: https://doi.org/10.1177/030913338801200401.

Oke, T.R. (1995) 'The heat island of the urban boundary layer: characteristics, causes and effects' in Cermak, J. E., Davenport, A. G., Plate, E. J. and Viegas, D. X., eds., *Wind climate in cities. NATO ASI Series, vol 277*, Dordrecht: Springer Netherlands, 81-107.

Oke, T.R. (2006) *Initial guidance to obtain representative meteorological observations at urban sites. Instruments and observing methods. Report No. 81, WMO/TD-No. 1250* World Meteorological Organization, available: https://library.wmo.int/index.php?lvl=notice_display&id=9262%20#.YlLWmshBxMs [accessed 10 April 2022].

Oke, T.R., Mills, G., Christen, A. and Voogt, J.A. (2017) *Urban climates*, Cambridge: Cambridge University Press.

OpenStreetMap contributors (2021) *OpenStreetMap. "© OpenStreetMap contributors"*, available: https://www.openstreetmap.org/copyright [accessed 07 June 2021].

Orthofoto (2014) *Open Data Österreich Katalog Orthofoto 2014 Wien (Open Data Austria Orthofoto 2014 Vienna) Datenquelle: Stadt Wien – data.wien.gv.at (Data source: City of Vienna – data.wien.gv.at)* [dataset], available: https://www.data.gv.at/katalog/dataset/stadt-wien_orthofotowien2014 [accessed 27 May 2021].

Orthofoto (2015) *Open Data Österreich Katalog Orthofoto 2015 Wien - Entzerrtes Luftbild (Open Data Austria Orthofoto 2015 Vienna - Rectified aerial photo). Datenquelle: Stadt Wien – data.wien.gv.at (Data source: City of Vienna – data.wien.gv.at)* [dataset], available: https://www.data.gv.at/katalog/en/dataset/stadt-wien_orthofotowien2015 [accessed 10 April 2022].

Paulina, W., Poh-Chin, L. and Melissa, H. (2015) 'Temporal statistical analysis of urban heat islands at the microclimate level', *Procedia Environmental Sciences*, 26, 91-94, available: https://doi.org/10.1016/j.proenv.2015.05.006.

PennState (2018a) *PennState Eberly College of Science - STAT 462 Applied Regression Analysis - Lesson 2: Simple Linear Regression (SLR) Model - 2.1 What is Simple Linear Regression (Lesson notes "reorganized and supplemented by Dr. Iain Pardoe, based on original notes by Dr. Laura Simon and Dr. Derek Young".)*, available: https://online.stat.psu.edu/stat462/node/91/ [accessed 04 November 2021].

PennState (2018b) *PennState Eberly College of Science - STAT 462 Applied Regression Analysis - Lesson 2: Simple Linear Regression (SLR) Model - 2.2 What is the "Best Fitting Line"? (Lesson notes "reorganized and supplemented by Dr. Iain Pardoe, based on original notes by Dr. Laura Simon and Dr. Derek Young".)*, available: https://online.stat.psu.edu/stat462/node/92/ [accessed 04 November 2021].

PennState (2018c) *PennState Eberly College of Science - STAT 462 Applied Regression Analysis - Lesson 2: Simple Linear Regression (SLR) Model - 2.4 What is the Common Error Variance? (Lesson notes "reorganized and supplemented by Dr. Iain Pardoe, based on original notes by Dr. Laura Simon and Dr. Derek Young".)*, available: https://online.stat.psu.edu/stat462/node/94/ [accessed 04 November 2021].

PennState (2018d) *PennState Eberly College of Science - STAT 462 Applied Regression Analysis - Lesson 2: Simple Linear Regression (SLR) Model - 2.5 The Coefficient of Determination, r-squared (Lesson notes "reorganized and supplemented by Dr. Iain Pardoe, based on original notes by Dr. Laura Simon and Dr. Derek Young".)*, available: https://online.stat.psu.edu/stat462/node/95/ [accessed 04 November 2021].

PennState (2018e) *PennState Eberly College of Science - STAT 462 Applied Regression Analysis - Lesson 5: Multiple Linear Regression (MLR) Model & Evaluation - 5.3 - The Multiple Linear Regression Model (Lesson notes "reorganized and supplemented by Dr. Iain Pardoe, based on original notes by Dr. Laura Simon and Dr. Derek Young".)*, available: https://online.stat.psu.edu/stat462/node/131/ [accessed 26 January 2022].

PennState (2018f) *PennState Eberly College of Science - STAT 462 Applied Regression Analysis - Lesson 11: Model Building - 11.3 - Best Subsets Regression, Adjusted R-Sq, Mallows Cp (Lesson notes "reorganized and supplemented by Dr. Iain Pardoe, based on original notes by Dr. Laura Simon and Dr. Derek Young".)*, available: https://online.stat.psu.edu/stat462/node/197/ [accessed 26 January 2022].

PennState (2018g) *PennState Eberly College of Science - STAT 462 Applied Regression Analysis - Lesson 3: SLR Evaluation - 3.6 - Further SLR Evaluation Examples (Lesson notes "reorganized and supplemented by Dr. Iain Pardoe, based on original notes by Dr. Laura Simon and Dr. Derek Young".)*, available: https://online.stat.psu.edu/stat462/node/108/ [accessed 31 March 2022].

Prata, A.J., Caselles, V., Coll, C., Sobrino, J.A. and Ottlé, C. (1995) 'Thermal remote sensing of land surface temperature from satellites: current status and future prospects', *Remote Sensing Reviews*, 12(3-4), 175-224, available: https://doi.org/10.1080/02757259509532285.

QGIS.org (2021) 'QGIS Geographic Information System. QGIS Association', available: http://www.qgis.org [accessed: 10 April 2022].

Rizwan, A.M., Dennis, L.Y.C. and Liu, C. (2008) 'A review on the generation, determination and mitigation of Urban Heat Island', *Journal of Environmental Sciences*, 20(1), 120-128, available: https://doi.org/10.1016/S1001-0742(08)60019-4.

Rotach, M.W., Vogt, R., Bernhofer, C., Batchvarova, E., Christen, A., Clappier, A., Feddersen, B., Gryning, S.E., Martucci, G., Mayer, H., Mitev, V., Oke, T.R., Parlow, E., Richner, H., Roth, M., Roulet, Y.A., Ruffieux, D., Salmond, J.A., Schatzmann, M. and Voogt, J.A. (2005) 'BUBBLE – an Urban Boundary Layer Meteorology Project', *Theoretical and Applied Climatology*, 81(3), 231-261, available: https://doi.org/10.1007/s00704-004-0117-9.

RStudio Team (2018) 'RStudio: Integrated Development for R. RStudio, Inc., Boston, MA URL'. available: http://www.rstudio.com/ [accessed: 10 April 2022].

Salata, F., Golasi, I., de Lieto Vollaro, R. and de Lieto Vollaro, A. (2016) 'Urban microclimate and outdoor thermal comfort. A proper procedure to fit ENVI-met simulation outputs to experimental data', *Sustainable Cities and Society*, 26, 318-343, available: https://doi.org/10.1016/j.scs.2016.07.005.

Salmerón Gómez, R., Rodríguez Sánchez, A., García, C.G. and García Pérez, J. (2020) 'The VIF and MSE in Raise Regression', *Mathematics*, 8(4), 605, available: https://doi.org/10.3390/math8040605.

Salomonson, V.V., Barnes, W.L., Maymon, P.W., Montgomery, H.E. and Ostrow, H. (1989) 'MODIS: advanced facility instrument for studies of the Earth as a system', *IEEE Transactions on Geoscience and Remote Sensing*, 27(2), 145-153, available: https://doi.org/10.1109/36.20292.

Santamouris, M., Cartalis, C., Synnefa, A. and Kolokotsa, D. (2015) 'On the impact of urban heat island and global warming on the power demand and electricity consumption of buildings—A review', *Energy and Buildings*, 98, 119-124, available: https://doi.org/10.1016/j.enbuild.2014.09.052.

Schaaf, C. and Wang, Z. (2015a) *MCD43A3 MODIS/Terra+Aqua BRDF/Albedo Daily L3 Global - 500m V006* [dataset], NASA EOSDIS Land Processes DAAC, available: https://doi.org/10.5067/MODIS/MCD43A3.006 [accessed 27 December 2020].

Schaaf, C. and Wang, Z. (2015b) *MCD43A2 MODIS/Terra+Aqua BRDF/Albedo Quality Daily L3 Global - 500m V006* [dataset], NASA EOSDIS Land Processes DAAC, available: https://doi.org/10.5067/MODIS/MCD43A2.006 [accessed 09 April 2022].

Schneider dos Santos, R. (2020) 'Estimating spatio-temporal air temperature in London (UK) using machine learning and earth observation satellite data', *International Journal of Applied Earth Observation and Geoinformation*, 88, 102066, available: https://doi.org/10.1016/j.jag.2020.102066.

Schneider dos Santos, R., Taylor, J., Davies, M., Mavrogianni, A. and Symonds, P. (2016) 'Modelling and monitoring tools to evaluate the urban heat island's contribution to the risk of indoor overheating', in *Proceedings of the 3rd IBPSA-England Conference BSO16*, Great North Museum, Newcastle, UK, 12 - 14 September 2016, 1134.

Schwarz, N., Lautenbach, S. and Seppelt, R. (2011) 'Exploring indicators for quantifying surface urban heat islands of European cities with MODIS land surface temperatures', *Remote Sensing of Environment*, 115(12), 3175-3186, available: https://doi.org/10.1016/j.rse.2011.07.003.

Selvam, S., Manisha, A., Vidhya, J. and Venkatramanan, S. (2019) 'Chapter 1 - Fundamentals of GIS' in Venkatramanan, S., Prasanna, M. V. and Chung, S. Y., eds., *GIS and Geostatistical techniques for groundwater science,* Elsevier, 3-15.

Shi, L., Liu, P., Kloog, I., Lee, M., Kosheleva, A. and Schwartz, J. (2016) 'Estimating daily air temperature across the Southeastern United States using high-resolution satellite data: a statistical modeling study', *Environmental Research*, 146, 51-58, available: https://doi.org/10.1016/j.envres.2015.12.006.

Shi, Y. and Zhang, Y. (2022) 'Urban morphological indicators of urban heat and moisture islands under various sky conditions in a humid subtropical region', *Building and Environment*, 214, 108906, available: https://doi.org/10.1016/j.buildenv.2022.108906.

Skarbit, N., Stewart, I.D., Unger, J. and Gál, T. (2017) 'Employing an urban meteorological network to monitor air temperature conditions in the 'local climate zones' of Szeged, Hungary', *International Journal of Climatology*, 37(S1), 582-596, available: https://doi.org/10.1002/joc.5023.

Snyder, W.C., Wan, Z., Zhang, Y. and Feng, Y.Z. (1998) 'Classification-based emissivity for land surface temperature measurement from space', *International Journal of Remote Sensing*, 19(14), 2753-2774, available: https://doi.org/10.1080/014311698214497.

Sobrino, J.A., Oltra-Carrió, R., Sòria, G., Bianchi, R. and Paganini, M. (2012) 'Impact of spatial resolution and satellite overpass time on evaluation of the surface urban heat island effects', *Remote Sensing of Environment*, 117, 50-56, available: https://doi.org/10.1016/j.rse.2011.04.042.

Sola, A., Corchero, C., Salom, J. and Sanmarti, M. (2018) 'Simulation tools to build urban-scale energy models: a review', *Energies*, 11(12), available: https://doi.org/10.3390/en11123269.

Solman, M. (2020) *The representation of urban climate for effective building energy performance simulation*, thesis (Diploma Thesis), Technische Universität Wien, reposiTUm, available: https://doi.org/10.34726/hss.2020.45904.

Stathopoulou, M., Synnefa, A., Cartalis, C., Santamouris, M., Karlessi, T. and Akbari, H. (2009) 'A surface heat island study of Athens using high-resolution satellite imagery and measurements of the optical and thermal properties of commonly used building and paving materials', *International Journal of Sustainable Energy*, 28(1-3), 59-76, available: https://doi.org/10.1080/14786450802452753.

Stewart, I. and Oke, T. (2009) 'Classifying urban climate field sites by “local climate zones”: The case of Nagano, Japan', *ICUC-7 The Seventh International Conference on Urban Climate* Yokohama, Japan, 29 June - 3 July 2009, Extended Abstract.

Stewart, I.D. (2011) *Redefining the urban heat island*, thesis (Doctor of Philosophy), The University of British Columbia, available: https://doi.org/10.14288/1.0072360.

Stewart, I.D. and Oke, T.R. (2012) 'Local Climate Zones for urban temperature studies', *Bulletin of the American Meteorological Society*, 93(12), 1879-1900, available: https://doi.org/10.1175/BAMS-D-11-00019.1.

Středová, H., Chuchma, F., Rožnovský, J. and Středa, T. (2021) 'Local Climate Zones, land surface temperature and air temperature interactions: case study of Hradec Králové, the Czech Republic', *ISPRS International Journal of Geo-Information*, 10(10), 704, available: https://doi.org/10.3390/ijgi10100704.

Sun, Y. and Augenbroe, G. (2014) 'Urban heat island effect on energy application studies of office buildings', *Energy and Buildings*, 77, 171-179, available: https://doi.org/10.1016/j.enbuild.2014.03.055.

Taha, H. (1997) 'Urban climates and heat islands: albedo, evapotranspiration, and anthropogenic heat', *Energy and Buildings*, 25(2), 99-103, available: https://doi.org/10.1016/S0378-7788(96)00999-1.

Terra (2022) *NASA - Terra: The EOS Flagship*, available: https://terra.nasa.gov/ [accessed 10 April 2022].

TIME_IS (2021) *Time.is Central European Time* available: https://time.is/CET [accessed 27 May 2021].

Tomlinson, C.J., Chapman, L., Thornes, J.E. and Baker, C. (2011) 'Remote sensing land surface temperature for meteorology and climatology: a review', *Meteorological Applications*, 18(3), 296-306, available: https://doi.org/10.1002/met.287.

Toth, C. and Jóźków, G. (2016) 'Remote sensing platforms and sensors: a survey', *ISPRS Journal of Photogrammetry and Remote Sensing*, 115, 22-36, available: https://doi.org/10.1016/j.isprsjprs.2015.10.004.

Tsagris, M. and Pandis, N. (2021) 'Multicollinearity', *American Journal of Orthodontics and Dentofacial Orthopedics*, 159(5), 695-696, available: https://doi.org/10.1016/j.ajodo.2021.02.005

Tsitoura, M., Tsoutsos, T. and Daras, T. (2014) 'Evaluation of comfort conditions in urban open spaces. Application in the island of Crete', *Energy Conversion and Management*, 86, 250-258, available: https://doi.org/10.1016/j.enconman.2014.04.059.

Tsoka, S. (2017) 'Investigating the relationship between urban spaces morphology and local microclimate: a study for Thessaloniki', *Procedia Environmental Sciences*, 38, 674-681, available: https://doi.org/10.1016/j.proenv.2017.03.148.

UN (2018) *United Nations - World Urbanization Prospects: The 2018 Revision [key facts]*, available: https://population.un.org/wup/Publications/Files/WUP2018-KeyFacts.pdf [accessed 31 March 2021].

UN (2022) *United Nations (UN) - Population*, available: https://www.un.org/en/global-issues/population#:~:text=The%20world%20population%20is%20projected,surrounding%20these%20latest%20population%20projections [accessed 10 April 2022].

Unger, J., Lelovics, E. and Gál, T. (2014) 'Local Climate Zone mapping using GIS methods in Szeged', *Hungarian Geographical Bulletin*, 63(1), 29-41, available: https://doi.org/10.15201/hungeobull.63.1.3.

USGS (2022a) *US. Geological Survey (USGS). What is a geographic information system (GIS)?*, available: https://www.usgs.gov/faqs/what-geographic-information-system-gis [accessed 10 April 2022].

USGS (2022b) *U.S. Geological Survey (USGS)*, available: https://www.usgs.gov/ [accessed 21 January 2022].

USGS_Landsat (2022) *USGS - What are the band designations for the Landsat satellites?*, available: https://www.usgs.gov/faqs/what-are-band-designations-landsat-satellites [accessed 25 March 2022].

Vahmani, P., Luo, X., Jones, A. and Hong, T. (2022) 'Anthropogenic heating of the urban environment: An investigation of feedback dynamics between urban micro-climate and decomposed anthropogenic heating from buildings', *Building and Environment*, 213, 108841, available: https://doi.org/10.1016/j.buildenv.2022.108841.

van Hove, L.W.A., Jacobs, C.M.J., Heusinkveld, B.G., Elbers, J.A., van Driel, B.L. and Holtslag, A.A.M. (2015) 'Temporal and spatial variability of urban heat island and thermal comfort within the Rotterdam agglomeration', *Building and Environment*, 83, 91-103, available: https://doi.org/10.1016/j.buildenv.2014.08.029.

Vermote, E. and Wolfe, R. (2015a) *MOD09GA MODIS/Terra Surface Reflectance Daily L2G Global 1kmand 500m SIN Grid V006* [dataset], NASA EOSDIS Land Processes DAAC, available: https://doi.org/10.5067/MODIS/MOD09GA.006 [accessed 28 December 2020].

Vermote, E. and Wolfe, R. (2015b) *MYD09GA MODIS/Aqua Surface Reflectance Daily L2G Global 1kmand 500m SIN Grid V006* [dataset], NASA EOSDIS Land Processes DAAC, available: https://doi.org/10.5067/MODIS/MYD09GA.006 [accessed 28 December 2020].

Vermote, E.F., Roger, J.C. and Ray, J.P. (2015) *MODIS Surface Reflectance User's Guide - Collection 6. MODIS Land Surface Reflectance Science Computing Facility*, available: https://lpdaac.usgs.gov/documents/306/MOD09_User_Guide_V6.pdf [accessed 30 May 2021].

Vienna_Baukörpermodell (2021) *Stadt Wien - Baukörpermodell (LOD1.4) (City of Vienna - Building Model (LOD1.4)) Datenquelle: Stadt Wien – data.wien.gv.at (Data source: City of Vienna – data.wien.gv.at)* [dataset], available: https://www.wien.gv.at/stadtentwicklung/stadtvermessung/geodaten/bkm/ [accessed 27 May 2021].

Vienna_FMZK (2021) *Stadt Wien - Flächen-Mehrzweckkarte (City of Vienna –Area multipurpose map) Datenquelle: Stadt Wien – data.wien.gv.at (Data source: City of Vienna – data.wien.gv.at)* [dataset], available: https://www.wien.gv.at/stadtentwicklung/stadtvermessung/geodaten/fmzk/ [accessed 27 May 2021].

Vienna Tourist Board (2021) *The Vienna Woods*, available: https://www.wien.info/en/sightseeing/excursions/vienna-woods-363998 [accessed 18 April 2021].

Voogt, J.A. (2002). 'Urban heat island' in Munn, T., editor-in-chief, *Encyclopedia of global environmental change*, Chichester (UK): John Wiley & Sons, 660 – 666.

Voogt, J. A. (2017). 'Urban climatology' in Richardson, D., Castree N., Goodchild, M.F., Kobayashi, A., Liu, W., and Marston, R.A., eds., *The international encyclopedia of geography: people, the earth, environment and technology*. John Wiley & Sons, Ltd, 1-14, available: https://doi.org/10.1002/9781118786352.wbieg0694.

Voogt, J.A. and Oke, T.R. (2003) 'Thermal remote sensing of urban climates', *Remote Sensing of Environment*, 86(3), 370-384, available: https://doi.org/10.1016/S0034-4257(03)00079-8.

Vu, D.H., Muttaqi, K.M. and Agalgaonkar, A.P. (2015) 'A variance inflation factor and backward elimination based robust regression model for forecasting monthly electricity demand using climatic variables', *Applied Energy*, 140, 385-394, available: https://doi.org/10.1016/j.apenergy.2014.12.011.

Vuckovic, M. (2015) *A framework for the representation of the urban environment and the assessment of its microclimatic variation*, thesis (Doktors der technischen Wissenschaften), Technische Universität Wien, reposiTUm, available: https://doi.org/10.34726/hss.2015.29763.

Vuckovic, M., Kiesel, K. and Mahdavi, A. (2016) 'Toward advanced representations of the urban microclimate in building performance simulation', *Sustainable Cities and Society*, 27, 356-366, available: https://doi.org/10.1016/j.scs.2016.05.002.

Vuckovic, M., Kiesel, K. and Mahdavi, A. (2017) 'The extent and implications of the microclimatic conditions in the urban environment: A Vienna case study', *Sustainability*, 9(2), 177, available: https://doi.org/10.3390/su9020177.

Wan, Z. (2008) 'New refinements and validation of the MODIS Land-Surface Temperature/Emissivity products', *Remote Sensing of Environment*, 112(1), 59-74, available: https://doi.org/10.1016/j.rse.2006.06.026.

Wan, Z. (2013) *Collection-6 MODIS Land Surface Temperature Products Users' Guide*, available: https://lpdaac.usgs.gov/documents/118/MOD11_User_Guide_V6.pdf [accessed 07 June 2021].

Wan, Z. (2014) 'New refinements and validation of the collection-6 MODIS land-surface temperature/emissivity product', *Remote Sensing of Environment*, 140, 36-45, available: https://doi.org/10.1016/j.rse.2013.08.027.

Wan, Z. and Dozier, J. (1996) 'A generalized split-window algorithm for retrieving land-surface temperature from space', *IEEE Transactions on Geoscience and Remote Sensing*, 34(4), 892-905, available: https://doi.org/10.1109/36.508406.

Wan, Z., Hook, S. and Hulley, G. (2015a) *MOD11A1 MODIS/Terra Land Surface Temperature/Emissivity Daily L3 Global 1km SIN Grid V006* [dataset], NASA EOSDIS Land Processes DAAC, available: https://doi.org/10.5067/MODIS/MOD11A1.006 [accessed 11 April 2020].

Wan, Z., Hook, S. and Hulley, G. (2015b) *MYD11A1 MODIS/Aqua Land Surface Temperature/Emissivity Daily L3 Global 1km SIN Grid V006* [dataset], NASA EOSDIS Land Processes DAAC, available: https://doi.org/10.5067/MODIS/MYD11A1.006 [accessed 12 April 2020].

Wan, Z. and Li, Z.-L. (1997) 'A physics-based algorithm for retrieving land-surface emissivity and temperature from EOS/MODIS data', *IEEE Transactions on Geoscience and Remote Sensing*, 35(4), 980-996, available: https://doi.org/10.1109/36.602541.

Wang, W., Liu, K., Tang, R. and Wang, S. (2019) 'Remote sensing image-based analysis of the urban heat island effect in Shenzhen, China', *Physics and Chemistry of the Earth, Parts A/B/C*, 110, 168-175, available: https://doi.org/10.1016/j.pce.2019.01.002.

Wang, Y., Berardi, U. and Akbari, H. (2016) 'Comparing the effects of urban heat island mitigation strategies for Toronto, Canada', *Energy and Buildings*, 114, 2-19, available: https://doi.org/10.1016/j.enbuild.2015.06.046.

Weng, Q. (2009) 'Thermal infrared remote sensing for urban climate and environmental studies: methods, applications, and trends', *ISPRS Journal of Photogrammetry and Remote Sensing*, 64(4), 335-344, available: https://doi.org/10.1016/j.isprsjprs.2009.03.007.

Wittich, K.P. (1997) 'Some simple relationships between land-surface emissivity, greenness and the plant cover fraction for use in satellite remote sensing', *International Journal of Biometeorology*, 41(2), 58-64, available: https://doi.org/10.1007/s004840050054.

WMO (2018) *World Meteorological Organization (WMO) - Guide to Instruments and Methods of Observation (WMO-No. 8), 2018 edition*, available: https://community.wmo.int/activity-areas/imop/wmo-no_8 [accessed 30 March 2022].

WMO (2022) *World Meteorological Organization (WMO)*, available: https://public.wmo.int/en [accessed 30 March 2022].

WMO_IMOP (2020) *WMO - Instruments and Methods of Observation Programme (IMOP)*, available: https://community.wmo.int/activity-areas/imop [accessed 30 March 2022].

WMO_OSCAR (2022a) *WMO - Observing Systems Capability Analysis and Review Tool (OSCAR) / Surface (OSCAR/Surface)*, available: https://oscar.wmo.int/surface/#/ [accessed 25 March 2022].

WMO_OSCAR (2022b) *WMO - Observing Systems Capability Analysis and Review Tool (OSCAR) Space-based Capabilities (OSCAR/Space)*, available: https://space.oscar.wmo.int/spacecapabilities [accessed 25 March 2022].

Wolfe, R.E., Roy, D.P. and Vermote, E. (1998) 'MODIS land data storage, gridding, and compositing methodology: Level 2 grid', *IEEE Transactions on Geoscience and Remote Sensing*, 36(4), 1324-1338, available: https://doi.org/10.1109/36.701082.

Wu, Y., Sharifi, A., Yang, P., Borjigin, H., Murakami, D. and Yamagata, Y. (2018) 'Mapping building carbon emissions within local climate zones in Shanghai', *Energy Procedia*, 152, 815-822, available: https://doi.org/10.1016/j.egypro.2018.09.195.

Yoo, C., Im, J., Park, S. and Quackenbush, L.J. (2018) 'Estimation of daily maximum and minimum air temperatures in urban landscapes using MODIS time series satellite data', *ISPRS Journal of Photogrammetry and Remote Sensing*, 137, 149-162, available: https://doi.org/10.1016/j.isprsjprs.2018.01.018.

Young, N.E., Anderson, R.S., Chignell, S.M., Vorster, A.G., Lawrence, R. and Evangelista, P.H. (2017) 'A survival guide to Landsat preprocessing', *Ecology*, 98(4), 920-932, available: https://doi.org/10.1002/ecy.1730.

Yow, D.M. (2007) 'Urban Heat Islands: Observations, impacts, and adaptation', *Geography Compass*, 1(6), 1227-1251, available: https://doi.org/10.1111/j.1749-8198.2007.00063.x.

Yuan, J., Farnham, C. and Emura, K. (2015) 'Development of a retro-reflective material as building coating and evaluation on albedo of urban canyons and building heat loads', *Energy and Buildings*, 103, 107-117, available: https://doi.org/10.1016/j.enbuild.2015.06.055.

Zakšek, K. and Schroedter-Homscheidt, M. (2009) 'Parameterization of air temperature in high temporal and spatial resolution from a combination of the SEVIRI and MODIS instruments', *ISPRS Journal of Photogrammetry and Remote Sensing*, 64(4), 414-421, available: https://doi.org/10.1016/j.isprsjprs.2009.02.006.

ZAMG (2022a) *Zentralanstalt für Meteorologie und Geodynamik (ZAMG) - Messnetze - Wetterstationen (Measuring Network - Weather Stations)*, available: https://www.zamg.ac.at/cms/de/klima/messnetze/wetterstationen [accessed 25 March 2022].

ZAMG (2022b) *Zentralanstalt für Meteorologie und Geodynamik (ZAMG)*, available: https://www.zamg.ac.at/cms/de/aktuell [accessed 25 March 2022].

Zheng, Y., Ren, C., Xu, Y., Wang, R., Ho, J., Lau, K. and Ng, E. (2018) 'GIS-based mapping of Local Climate Zone in the high-density city of Hong Kong', *Urban Climate*, 24, 419-448, available: https://doi.org/10.1016/j.uclim.2017.05.008.

7. APPENDIX

7.1. Calculating building-related attributes

Table 35. Results from surface fraction calculations

	Building Surface Area (m2)	Pervious Surface Area (m2)	Impervious Surface Area (m2)
IS	92391.86	15513.79	88443.89
HW	27376.55	127628.52	41344.45
DF	39520.85	102811.30	54017.38
MB	12184.57	132373.53	51791.44
GE	17747.43	158435.79	20166.27
SC	29.77	166244.01	30075.77
SD	18901.63	151814.01	25633.97

7.2. LST - T_{air} relationship

Table 36. Linear regression results of LST_{DAY} – T_{air} datasets

Overview	**R-Squared (R^2)**		**RMSE [K]**		**Number of observations (n)**	
	0.903		2.60		7255	
ANOVA Results		**DF**	**Sum of squares**	**Mean squares**	**F statistics**	**P-value**
	Regression	1	456431.90	456431.90	67542.40	0.00
	Residual	7253	49013.66	6.76		
	Total	7254	505445.56			
Variables		**Coefficients**	**Standard Error (SE) [K]**		**t Statistics**	**P-value**
	Intercept	-0.1768	0.08		-2.10	0.04
	LST_{DAY}	0.7755	2.98e-3		259.89	0.00

Table 37. Linear regression results of LST_{NIGHT} – T_{air} datasets

Overview	**R-Squared (R^2)**		**RMSE [K]**		**Number of observations (n)**	
	0.971		1.50		5192	
ANOVA Results		**DF**	**Sum of squares**	**Mean squares**	**F statistics**	**P-value**
	Regression	1	394049.36	394049.36	175845.58	0.00
	Residual	5190	11630.18	2.24		
	Total	5191	405679.54			
Variables		**Coefficients**	**Standard Error (SE) [K]**		**t Statistics**	**P-value**
	Intercept	1.8572	0.03		67.25	0.00
	LST_{NIGHT}	0.9829	2.34e-3		419.34	0.00

Table 38. Linear regression results of $LST_{TERRA\text{-}DAY}$ – T_{air} datasets

Overview	**R-Squared (R^2)**		**RMSE [K]**		**Number of observations (n)**	
	0.904		2.60		4104	
ANOVA Results		**DF**	**Sum of squares**	**Mean squares**	**F statistics**	**P-value**
	Regression	1	261309.67	261309.67	38636.58	0.00
	Residual	4102	27742.93	6.76		
	Total	4103	289052.60			
Variables		**Coefficients**	**Standard Error (SE) [K]**		**t Statistics**	**P-value**
	Intercept	-0.2487	0.11		-2.31	0.02
	$LST_{TERRA\text{-}DAY}$	0.7763	3.95e-3		196.56	0.00

Table 39. Linear regression results of $LST_{AQUA\text{-}DAY}$ – T_{air} datasets

Overview	**R-Squared (R^2)**		**RMSE [K]**		**Number of observations (n)**	
	0.899		2.60		3151	
ANOVA Results		**DF**	**Sum of squares**	**Mean squares**	**F statistics**	**P-value**
	Regression	1	188144.31	188144.31	27887.89	0.00
	Residual	3149	21244.58	6.75		
	Total	3150	209388.89			
Variables		**Coefficients**	**Standard Error (SE) [K]**		**t Statistics**	**P-value**
	Intercept	-0.0356	0.14		-0.26	0.79
	$LST_{AQUA\text{-}DAY}$	0.7727	4.63e-3		167.00	0.00

Table 40. Linear regression results of $LST_{TERRA\text{-}NIGHT}$ – T_{air} datasets

Overview	**R-Squared (R^2)**		**RMSE [K]**		**Number of observations (n)**
	0.975		1.42		2797
ANOVA Results		**DF**	**Sum of squares**	**Mean squares**	**F statistics**	**P-value**
	Regression	1	224005.41	224005.41	111104.76	0.00
	Residual	2795	5635.18	2.02		
	Total	2796	229640.59			
Variables		**Coefficients**	**Standard Error (SE) [K]**		**t Statistics**	**P-value**
	Intercept	2.2809	0.04		62.94	0.00
	$LST_{TERRA\text{-}NIGHT}$	0.9877	2.96e-3		333.32	0.00

Table 41. Linear regression results of $LST_{AQUA\text{-}NIGHT}$ – T_{air} datasets

Overview	**R-Squared (R^2)**		**RMSE [K]**		**Number of observations (n)**
	0.973		1.39		2395
ANOVA Results		**DF**	**Sum of squares**	**Mean squares**	**F statistics**	**P-value**
	Regression	1	166397.17	166397.17	85567.57	0.00
	Residual	2393	4653.50	1.94		
	Total	2394	171050.67			
Variables		**Coefficients**	**Standard Error (SE) [K]**		**t Statistics**	**P-value**
	Intercept	1.4131	0.04		37.94	0.00
	$LST_{AQUA\text{-}NIGHT}$	0.9694	3.31e-3		292.52	0.00

Table 42. Linear regression results of remaining LST_{DAY} – T_{air} observations after including BSA data

Overview	**R-Squared (R^2)**		**RMSE [K]**		**Number of observations (n)**	
	0.896		2.57		6714	
ANOVA Results		**DF**	**Sum of squares**	**Mean squares**	**F statistics**	**P-value**
	Regression	1	383542.68	383542.68	58012.55	0.00
	Residual	6712	44375.54	6.61		
	Total	6713	427918.23			
Variables		**Coefficients**	**Standard Error (SE) [K]**		**t Statistics**	**P-value**
	Intercept	-0.0699	0.09		-0.76	0.45
	LST_{DAY}	0.7739	3.21e-3		240.86	0.00

7.3. Deriving T_{air}: Multiple regression results

7.3.1. Day-time inquiries

Table 43. Results from multiple regression inquiries for day-time without ISF and EBH parameters

	Coefficients	VIF	SE (K)	t-Statistics	p-value
Intercept	1.563	X	0.53	2.9326	3.37e-3
LST_{DAY}	0.89916	4.08	0.01	157.56	0.00
BSF	-34.069	**53.19**	1.61	-21.179	2.01e-96
PSF	-10.082	**36.52**	0.78	-12.953	6.46e-38
MBH	0.24947	**15.12**	0.02	11.357	1.27e-29
SVF	-0.53424	**6.62**	0.40	-1.3424	**0.18**
SZA	0.087674	3.83	4.34e-3	20.191	4.63e-88
BSA	7.0365	1.46	1.08	6.5454	6.37e-11
Model's Performance					
Adjusted R^2	0.920				
RMSE (K)	2.26				
n	6714				

Table 44. Results from multiple regression inquiries for day-time without ISF, BSF, MBH and EBH parameters

	Coefficients	VIF	SE (K)	t-Statistics	p-value
Intercept	-7.2765	X	0.38	-19.068	5.56e-79
LST_{DAY}	0.87708	3.97	0.01	149.64	0.00
PSF	7.3573	2.66	0.22	33.627	3.09e-229
SVF	-5.7679	3.07	0.28	-20.451	3.18e-90
SZA	0.073448	3.76	4.48e-3	16.406	2.44e-59
BSA	6.4656	1.45	1.12	5.7867	7.50e-09
Model's Performance					
Adjusted R^2	0.913				
RMSE (K)	2.35				
n	6714				

Table 45. Results from multiple regression inquiries for day-time without ISF, PSF and EBH parameters

	Coefficients	VIF	SE (K)	t-Statistics	p-value
Intercept	-2.9997	X	0.40	-7.4083	1.44e-13
LST_{DAY}	0.89285	4.05	0.01	155.11	0.00
BSF	-14.737	**7.40**	0.61	-24.264	9.96e-125
MBH	0.073723	**9.35**	0.02	4.2159	2.52e-5
SVF	-4.3988	2.90	0.27	-16.498	5.72e-60
SZA	0.083145	3.81	4.38e-3	18.976	2.92e-78
BSA	7.0172	1.46	1.09	6.4478	1.21e-10
Model's Performance					
Adjusted R^2	0.918				
RMSE (K)	2.29				
n	6714				

Table 46. Results from multiple regression inquiries for day-time without ISF, BSF, MBH, SZA and EBH parameters

	Coefficients	VIF	SE (K)	t-Statistics	p-value
Intercept	-1.7752	X	0.19	-9.5553	1.69e-21
LST_{DAY}	0.79489	1.07	3.10e-3	256.23	0.00
PSF	6.6945	2.57	0.22	30.529	8.69e-192
SVF	-5.1205	3.01	0.28	-17.98	1.24e-70
BSA	4.1885	1.43	1.13	3.7047	2.13e-4
Model's Performance					
Adjusted R^2	0.910				
RMSE (K)	2.40				
n	6714				

Table 47. Results from multiple regression inquiries for day-time without ISF, PSF, SZA and EBH parameters

	Coefficients	VIF	SE (K)	t-Statistics	p-value
Intercept	2.6999	X	0.28	9.6869	4.77e-22
LST_{DAY}	0.79926	1.08	3.05e-3	262.34	0.00
BSF	-13.265	**7.28**	0.62	-21.454	8.20e-99
MBH	0.067668	**9.35**	0.02	3.7706	1.64e-4
SVF	-3.7905	2.86	0.27	-13.952	1.25e-43
BSA	4.4129	1.43	1.11	3.9822	6.90e-5
Model's Performance					
Adjusted R^2	0.913				
RMSE (K)	2.35				
n	6714				

Table 48. Results from multiple regression inquiries for day-time without PSF and EBH parameters

	Coefficients	VIF	SE (K)	t-Statistics	p-value
Intercept	-8.5187	X	0.58	-14.577	2.09e-47
LST_{DAY}	0.89916	4.08	0.01	157.56	0.00
BSF	-23.987	**17.88**	0.93	-25.717	3.49e-139
ISF	10.082	**7.86**	0.78	12.953	6.46e-38
MBH	0.24947	**15.12**	0.02	11.357	1.27e-29
SVF	-0.53424	**6.62**	0.40	-1.3424	**0.18**
SZA	0.087674	3.83	4.34e-3	20.191	4.63e-88
BSA	7.0365	1.46	1.08	6.5454	6.37e-11
Model's Performance					
Adjusted R^2	0.920				
RMSE (K)	2.26				
n	6714				

Table 49. Results from multiple regression inquiries for day-time without BSF and MBH parameters

	Coefficients	VIF	SE (K)	t-Statistics	p-value
Intercept	-16.11	X	0.84	-19.174	8.04e-80
LST_{DAY}	0.89446	4.06	0.01	155.91	0.00
ISF	17.155	**13.09**	1.01	16.938	4.76e-63
PSF	11.244	**39.66**	0.82	13.752	1.87e-42
SVF	-3.1071	4.09	0.32	-9.8588	8.97e-23
EBH	-0.17601	**13.74**	0.04	-4.4426	9.03e-06
SZA	0.084177	3.82	4.37e-3	19.267	1.48e-80
BSA	6.5058	1.45	1.08	6.0095	1.96e-09
Model's Performance					
Adjusted R^2	0.919				
RMSE (K)	2.28				
n	6714				

Table 50. Results from multiple regression inquiries for day-time without BSF, MBH and PSF parameters

	Coefficients	VIF	SE (K)	t-Statistics	p-value
Intercept	-6.4322	X	0.47	-13.823	7.15e-43
LST_{DAY}	0.88487	4.00	0.01	153.25	0.00
ISF	6.8172	**5.88**	0.69	9.9063	5.62e-23
SVF	-1.5585	3.56	0.30	-5.222	1.82e-7
EBH	-0.65061	3.31	0.02	-32.976	3.84e-221
SZA	0.077338	3.77	4.40e-3	17.573	1.28e-67
BSA	6.5304	1.45	1.10	5.9494	2.83e-9
Model's Performance					
Adjusted R^2	0.916				
RMSE (K)	2.31				
n	6714				

Table 51. Results from multiple regression inquiries for day-time without BSF, MBH and ISF parameters

	Coefficients	VIF	SE (K)	t-Statistics	p-value
Intercept	-4.0714	X	0.46	-8.8992	7.14e-19
LST_{DAY}	0.88181	3.99	0.01	151.82	0.00
PSF	0.96437	**17.81**	0.56	1.7236	**0.08**
SVF	-3.8595	4.00	0.32	-12.114	1.98e-33
EBH	-0.45564	**11.35**	0.04	-12.39	7.13e-35
SZA	0.075393	3.76	4.43e-3	17.021	1.24e-63
BSA	6.835	1.45	1.11	6.1842	6.61e-10
Model's Performance					
Adjusted R^2	0.915				
RMSE (K)	2.33				
n	6714				

Table 52. Results from multiple regression inquiries for day-time without BSF, MBH, PSF and SZA parameters

	Coefficients	VIF	SE (K)	t-Statistics	p-value
Intercept	-0.7371	X	0.34	-2.1585	0.03
LST_{DAY}	0.79812	1.08	3.06e-3	260.56	0.00
ISF	6.1959	**5.86**	0.70	8.8155	1.50e-18
SVF	-1.2982	3.56	0.30	-4.2584	2.09e-5
EBH	-0.59256	3.22	0.02	-29.788	3.14e-183
BSA	4.1578	1.43	1.11	3.7322	1.91e-4
Model's Performance					
Adjusted R^2	0.912				
RMSE (K)	2.36				
n	6714				

Table 53. Results from multiple regression inquiries for day-time without BSF, MBH, PSF and ISF parameters

	Coefficients	VIF	SE (K)	t-Statistics	p-value
Intercept	-3.6086	X	0.37	-9.7405	2.84e-22
LST_{DAY}	0.88143	3.99	0.01	151.84	0.00
SVF	-3.4772	2.06	0.23	-15.203	2.39e-51
EBH	-0.5141	1.70	0.01	-36.148	1.40e-261
SZA	0.075098	3.76	4.43e-3	16.964	3.11e-63
BSA	6.8018	1.45	1.11	6.1542	7.98e-10
Model's Performance					
Adjusted R^2	0.915				
RMSE (K)	2.33				
n	6714				

Table 54. Results from multiple regression inquiries for day-time without BSF, MBH, PSF and SVF parameters

	Coefficients	VIF	SE (K)	t-Statistics	p-value
Intercept	-7.653	X	0.40	-18.984	2.56e-78
LST_{DAY}	0.88272	3.98	0.01	152.97	0.00
ISF	9.1492	3.40	0.52	17.44	1.18e-66
EBH	-0.66524	3.25	0.02	-33.996	7.30e-234
SZA	0.076197	3.76	4.40e-3	17.301	1.21e-65
BSA	4.3156	1.24	1.01	4.2544	2.123-5
Model's Performance					
Adjusted R^2	0.916				
RMSE (K)	2.31				
n	6714				

Table 55. Results from multiple regression inquiries for day-time without BSF, MBH, PSF, SVF and SZA parameters

	Coefficients	VIF	SE (K)	t-Statistics	p-value
Intercept	-1.8266	X	0.23	-8.0653	8.59e-16
LST_{DAY}	0.7974	1.07	0.00	260.39	0.00
ISF	8.1508	3.36	0.53	15.296	6.10e-52
EBH	-0.60549	3.15	0.02	-30.759	1.76e-194
BSA	2.3376	1.22	1.03	2.2694	0.02
Model's Performance					
Adjusted R^2	0.912				
RMSE (K)	2.37				
n	6714				

7.3.2. Night-time inquiries

Table 56. Results from multiple regression inquiries for night-time without ISF and EBH parameters

	Coefficients	VIF	SE (K)	t-Statistics	p-value
Intercept	-4.2038	X	0.28	-14.911	2.90e-49
LST_{NIGHT}	0.98291	1.00	1.99e-3	493.6	0.00
BSF	10.324	**56.75**	1.04	9.9024	6.48e-23
PSF	1.5566	**39.21**	0.51	3.072	2.14e-3
MBH	-0.032671	**16.69**	0.01	-2.2705	0.02
SVF	5.2057	**6.98**	0.26	20.117	9.97e-87
Model's Performance					
Adjusted R^2	0.979				
RMSE (K)	1.27				
n	5192				

Table 57. Results from multiple regression inquiries for night-time without ISF, BSF, MBH and EBH parameters

	Coefficients	VIF	SE (K)	t-Statistics	p-value
Intercept	-0.21346	X	0.08	-2.6522	8.02e-3
LST_{NIGHT}	0.98351	1.00	2.03e-3	483.97	0.00
PSF	-4.5617	2.60	0.13	-34.222	1.27e-231
SVF	6.6976	2.60	0.16	41.513	0.00
Model's Performance					
Adjusted R^2	0.978				
RMSE (K)	1.30				
n	5192				

Table 58. Results from multiple regression inquiries for night-time without ISF, PSF and EBH parameters

	Coefficients	VIF	SE (K)	t-Statistics	p-value
Intercept	-3.4867	X	0.16	-22.041	5.45e-103
LST_{NIGHT}	0.98303	1.00	1.99e-3	493.34	0.00
BSF	7.3418	7.55	0.38	19.297	3.49e-80
MBH	-0.0043805	9.85	0.01	-0.39586	**0.69**
SVF	5.8411	2.52	0.16	37.529	6.43e-273
Model's Performance					
Adjusted R^2	0.979				
RMSE (K)	1.27				
n	5192				

Table 59. Results from multiple regression inquiries for night-time without PSF and EBH parameters

	Coefficients	VIF	SE (K)	t-Statistics	p-value
Intercept	-2.6472		0.32	-8.3861	6.41e-17
LST_{NIGHT}	0.98291	1.00	1.99e-3	493.6	0.00
BSF	8.7675	**18.79**	0.60	14.614	1.97e-47
ISF	-1.5566	**8.44**	0.51	-3.072	2.14e-3
MBH	-0.032671	**16.69**	0.01	-2.2705	0.02
SVF	5.2057	**6.98**	0.26	20.117	9.97e-87
Model's Performance					
Adjusted R^2	0.979				
RMSE (K)	1.27				
n	5192				

Table 60. Results from multiple regression inquiries for night-time without BSF and MBH parameters

	Coefficients	VIF	SE (K)	t-Statistics	p-value
Intercept	1.5378	X	0.46	3.3212	9.03e-4
LST_{NIGHT}	0.98284	1.00	1.98e-3	496.53	0.00
ISF	-6.2076	**12.88**	0.62	-9.972	3.27e-23
PSF	-3.6798	**43.02**	0.53	-6.9744	3.46e-12
SVF	4.9175	3.97	0.19	25.335	1.31e-133
EBH	0.21322	**15.63**	0.03	8.1604	4.15e-16
Model's Performance					
Adjusted R^2	0.980				
RMSE (K)	1.26				
n	5192				

Table 61. Results from multiple regression inquiries for night-time without BSF, MBH and PSF parameters

	Coefficients	VIF	SE (K)	t-Statistics	p-value
Intercept	-1.366	X	0.20	-6.7105	2.15e-11
LST_{NIGHT}	0.98289	1.00	1.99e-3	494.29	0.00
ISF	-3.086	6.22	0.43	-7.1003	1.41e-12
SVF	4.344	3.26	0.18	24.594	1.98e-126
EBH	0.37572	3.20	0.01	31.632	5.81e-201
Model's Performance					
Adjusted R^2	0.979				
RMSE (K)	1.27				
n	5192				

Table 62. Results from multiple regression inquiries for night-time without BSF, MBH and ISF parameters

	Coefficients	VIF	SE (K)	t-Statistics	p-value
Intercept	-2.6482	X	0.20	-13.425	2.03e-40
LST_{NIGHT}	0.98308	1.00	2.00e-3	492.04	0.00
PSF	0.10307	**20.78**	0.37	0.27845	**0.78**
SVF	5.1941	3.89	0.19	26.784	3.91e-148
EBH	0.32257	**12.87**	0.02	13.474	1.07e-40
Model's Performance					
Adjusted R^2	0.979				
RMSE (K)	1.27				
n	5192				

Table 63. Results from multiple regression inquiries for night-time without BSF, MBH, ISF and PSF parameters

	Coefficients	VIF	SE (K)	t-Statistics	p-value
Intercept	-2.6019	X	0.11	-24.542	6.26e-126
LST_{NIGHT}	0.98308	1.00	2.00e-3	492.1	0.00
SVF	5.2354	1.61	0.12	41.94	0.00
EBH	0.31633	1.61	0.01	37.331	2.16e-270
Model's Performance					
Adjusted R^2	0.979				
RMSE (K)	1.27				
n	5192				

Pelin Fırat Örs

EDUCATION

Doctoral Degree

2017 – Current	TU Wien, Doctoral Programme in Engineering Sciences, Dissertation field: Architecture
2016, Summer Term	Mobility, Incoming to Austria - Erasmus+ TU Wien, Institute of Architectural Sciences, Department of Building Physics and Building Ecology (Doctoral Programme in Engineering Sciences, Dissertation field: Architecture)
2013 – Discontinued	Izmir Institute of Technology, PhD Programme in Architecture

Master's Degree

2011 – 2013	Izmir Institute of Technology, The Graduate School of Engineering and Sciences, Master's Programme: Architecture

Bachelor's Degree

2003 – 2009	Dokuz Eylül University, Faculty of Architecture, Department of Architecture

ACADEMIC POSITIONS

01. 2012 – 09. 2017	Research Assistant Izmir Institute of Technology, Department of Architecture
07. 2011 – 01. 2012	Research Assistant Izmir University of Economics, Department of Architecture